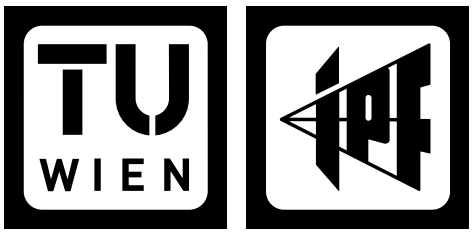

Masterarbeit

Validation and Improvement of the Freeze/Thaw detection Algorithm from ASCAT Data

ausgeführt am Institut für
Photogrammetrie und Fernerkundung
der Technischen Universität Wien

unter der Anleitung von

Prof. Dr. Wolfgang Wagner

und

Dr. Vahid Naeimi
Dr. Annett Bartsch
als mitwirkende Universitätsassistenten

durch
Christoph Paulik
Gumpendorferstrasse 72/9
1060 Wien

25 Oktober 2011

A

Abstract

The Freeze/Thaw state of the surface has wide reaching consequences for numerous processes in nature. It is coupled to the surface energy budget, hydrological activity which starts when melting begins, vegetation growing season dynamics,the terrestrial carbon budget and also the remote sensing retrieval of soil moisture, which is not valid if the soil is frozen. Mainly because of the last reason, the Institute for Photogrammetry and Remote Sensing at the Technical University of Vienna has recently developed an empirical threshold-analysis algorithm for the detection of frozen surface states using only the ASCAT data. Previously the ASCAT Scatterometer on-board the MetOp-A satellite provided soil moisture measurements but depended on external probabilistic data for flagging measurements taken over frozen ground.

The algorithm uses the distribution of normalized backscatter measurements (σ^{40}) over temperature to find parameters that characterize the behaviour of backscatter when freezing occurs. Based on these parameters a decision tree based approach is used for freeze/thaw detection. This work presents a first validation of the resulting freeze/thaw product using different global and regional temperature datasets ranging from model data (ERA-INTERIM, GLDAS-NOAH) and in-situ measurements (WMO-METEO stations, GTN-P borehole data) to satellite derived land surface temperature (MODIS-LST,AATSR-LST). The validation shows good agreement between the extracted frozen/unfrozen flag and the temperature data but also the need for improvement in certain situations. The shortcomings of the algorithm are found to be ambiguities in the backscatter/temperature relationship as well as systematic problems in some areas. As a last step it was tried to simplify, and make the algorithm more robust through the use of ancillary data that eliminates the need to account for numerous possible cases of backscatter in summer and winter and focuses on the critical times in spring and autumn when most freeze/thaw events take place. The results of these slight modifications were then validated using the same datasets and the results were improved in most cases.

Z

Zusammenfassung

Der Frostzustand der Erdoberfläche hat weitreichende Konsequenzen für eine vielzahl von Vorgängen in der Natur. Der Bodenenergiehaushalt, der Wasserzyklus, die Wachstumszeiten der Pflanzen, der Kohlenstoffhaushalt der Erde, und auch die Messung der Bodenfeuchte mit Fernerkundungstechnologien, welche bei gefrorenem Boden nicht möglich ist, sind stark vom Frostzustand abhängig. Am Institut für Photogrammetrie und Fernerkundung and der TU Wien wurde ein empirischer, auf Schwellenwerten basierender Algorithmus entwickelt, welcher es ermöglicht den Frostzustand nur mithilfe von ASCAT Daten festzustellen. Vor dieser Entwicklung war die vom ASCAT Scatterometer gemessene Bodenfeuchte von externen Wahrscheinichkeiten für gefrorenen Boden abhänging, um Messwerte zu erkennen die über selbigem gemacht wurden.

Der Algorithmus verwendet die Verteilung von normalisierter Rückstreuung (σ^{40}) über Temperaturmesswerten um daraus Parameter abzuleiten welche das Verhalten der Rückstreuung beim gefrieren des Bodens beschreiben. Basierend auf diesen Parametern führen mehrere Entscheidungsbäume zu einer Aussage über den Frostzustand. Im Zuge dieser Arbeit wurde eine erste Valdierung des resultierenden Produktes mit unterschiedlichen globalen und regionalen Temperaturdatensätzen vorgenommen. Dabei wurden sowohl Klimamodelle (ERA-INTERIM, GLDAS-NOAH) als auch in situ Messwerte (WMO-METEO Stationen, GTN-P Bohrlochdaten) und von Satelliten gemessene Bodentemperaturdaten (MODIS-LST,AATSR-LST) verwendet. Die Validierung zeigt gute Übereinstimmungen zwischen dem abgeleiteten Frostzustand und den verschiedenen Datensätzen, aber auch die Notwendigkeit von Verbesserungen in bestimmten Situationen. Die Probleme des Algorithmus treten hauptsächlich dann auf wenn der Zusammenhang zwischen Rückstreuung und Temperatur nicht eindeutig gegeben ist, es kommen aber in machen Gebieten noch systematische Fehler hinzu. Als letzter Schritt wurde versucht die Entscheidungsbäume zu vereinfachen und die Robustheit des Algorithmus zu verbessern indem durch externe Datensätze die zu berücksichtigenden Kombinationen von Rückstreuung und Temperatur, minimiert werden. Dadurch kann sich der Algorithmus auf die für den Frostzustand wichtige Zeit in Frühling und Herbst konzentrieren. Die Ergebnisse dieser Änderungen wurden ebenfalls validiert und bedeuten in den meisten Fällen eine Verbesserung.

A

Acknowledgments

The research in this thesis was done at the Institute of Photogrammetry and Remote Sensing at the Vienna University of Technology. I would like to thank all my colleagues but especially Annett Bartsch, for providing invaluable insights into the actual ground processes going on during freezing and thawing, Vahid Naeimi for developing the algorithm this thesis is based upon and for letting me test it thoroughly and Wolfgang Wagner for his support in every aspect of creating this document and for providing a great research environment.

I also want to thank all my friends who made live so much more fun in the last few years, especially the "Sparverein", but the biggest thank you has to go to my parents who always supported me in whatever I wanted to do.

This work was supported by the geoland-II project in frame of the Global Monitoring for Environment and Security (GMES), a joint initiative of the European Commission (EC) and the European Space Agency (ESA), the PERMAFROST project funded by the European Space Agency (ESA) Data User Element (DUE) and the project ALANIS funded by the European Space Agency (ESA) and the Integrated Land Ecosystem-Atmosphere Processes Study (iLEAPS).

C

Contents

F

List of Figures

T

List of Tables

1

Introduction

1.1 Remote Sensing

The term "Remote Sensing" has several definitions, with one of the broadest being "the collection of information about an object without making physical contact with it" [12]. For the purpose of this thesis we can focus on the collection of information about the earth's surface using electromagnetic radiation. Whereas observation platforms can be mounted on any machine capable of flying, the focus here is on satellite remote sensing since it is able to observe the earth on a global scale, including regions that are hard to reach using other methods. Active remote sensing sends electromagnetic waves to the earth and measures the reflected signal while passive systems observe the radiation that is naturally occurring.

The atmosphere absorbs most radiation therefore observation from satellites is only possible using frequencies in the so called atmospheric windows (see also Fig. 2.1). The atmosphere is more or less transparent for visible light, thermal infrared and microwave frequencies. Microwaves are especially useful for continuous global observations because cloud cover is not an issue. Scatterometers, as for example ASCAT on-board METOP-A are great tools for monitoring global phenomenon like soil moisture or the freeze/thaw state of the soil because they can provide near daily global coverage, although the spatial resolution is not great.

1.2 Freeze/Thaw State

The Freeze/Thaw state of the surface has wide reaching consequences for numerous processes in nature [13]. It is coupled to the surface energy budget, hydrological activity which starts when melting begins, vegetation growing season dynamics and the terrestrial carbon budget. The changing extent and timing of soil freezing can influence the existence of permafrost. Thawing ice rich permafrost can lead to the subsidence of the ground and the formation of thermokarst which impacts human and animal populations [14].

1.3 Objective and Structure of Work

There are two objectives of this Master Thesis. Firstly the validation of the Freeze/Thaw flagging of the ASCAT Soil Moisture Product. Until recently this was based on historic probabilistic quality flags (frozen surface,snow and ice probabilities) and is now done with the Surface State Flag which is derived from the ASCAT measurements directly [15]. Secondly, assessing the Surface State Flag algorithm and finding improvements to it.

After this introduction the second chapter will give an overview of the theoretical foundations of microwave remote sensing. This will include a description of electromagnetic waves and their interaction with the surface of the earth.

Chapter 3 will give an overview of the used datasets, both for producing the Surface State Flag as well as validation. The ASCAT Sensor, it's observation geometry and the normalization of backscatter to 40° will be covered. Global Atmospheric Models (ERA-Interim, GLDAS-NOAH), in situ datasets (WMO ds512,GTN-P) and Satellite observations (MODIS LST) used for validation will also be explained.

Chapter 4 will focus on the Freeze/Thaw flagging algorithm from ASCAT data. It will cover the Surface State Flag algorithm and the 9 Freeze/Thaw parameters needed for SSF generation. Also the 3 decision trees that lead to the SSF will be explained.

Chapter 5 presents the validation methods and looks into the error classification used. Then the results of the validation using the different temperature datasets will be discussed starting with the model datasets. The differences between the validation results will be shown with examples were they are comparable. The chapter will also look into the reasons for algorithm failure.

Chapter 6 proposes 2 ways to use ancillary data to improve the accuracy and robustness of the algorithm. It also includes a comparison of the validation results achieved with the original SSF with the ones using the suggested improvements. Additionally it will contain an assessment of how the use of ancillary data influences the failure cases found in chapter 5.

The Last Chapter provides a summary and looks into possible future developments.

2

Microwave Remote Sensing

This chapter focuses on active remote sensing in the microwave domain (roughly 0.3 GHz - 300 GHz) and how the backscattered signal is influenced by the structure and dielectric properties of the earth's surface with a special focus on how freezing changes the backscatter coefficient. For a broader look at the topic see [2, 4, 7, 12].

2.1 Electromagnetic Waves

2.1.1 Maxwell's equations

Maxwell's equations are the basic theory explaining the propagation of electromagnetic radiaton as waves, the following summary follows mainly [12]

The equations for free space can be written like

$$\nabla \cdot \mathbf{E} = 0 \tag{2.1}$$

$$\nabla \cdot \mathbf{B} = 0 \tag{2.2}$$

$$\nabla \times \mathbf{E} = -\frac{\partial \mathbf{B}}{\partial t} \tag{2.3}$$

$$\nabla \times \mathbf{B} = \epsilon_0 \mu_0 \frac{\partial \mathbf{E}}{\partial t} \tag{2.4}$$

where **E** and **B** are the electric and magnetic field vectors and ϵ_0 and μ_0 denote the electric permittivity and the magnetic permeability of free space.

The plane wave

$$E_x = E_0 \cos(\omega t - kz), E_y = E_z = 0 \tag{2.5}$$

$$B_y = \frac{E_0}{c} \cos(\omega t - kz), B_x = B_z = 0 \tag{2.6}$$

satisfies Maxwell's equation for free space under the condition that the wave speed is

$$c = \frac{\omega}{k} = \frac{1}{\sqrt{\epsilon_0 \mu_0}} \tag{2.7}$$

using

$$\omega = 2\pi f \text{ and } k = \frac{2\pi}{\lambda} \tag{2.8}$$

as the angular frequency ω and the wave number k. The constant c is, of course, the speed of light in a vacuum. **E** and **B** are perpendicular to one another and travel along the z-axis which is sometimes defined through the wave vector **k**.

Active Remote Sensing Systems do not send electromagnetic waves exclusively through vacuum, so we have to modify the equations in order to describe their behaviour when travelling through a homogeneous medium of some sort.

Every medium has two properties that define how electromagnetic waves interact with it, these are the electric permittivity ϵ and the magnetic permeability μ. They are related to the electric permittivity and the magnetic permeability of free space through

$$\mu = \mu_r \mu_0 \tag{2.9}$$

and

$$\epsilon = \epsilon_r \epsilon_0 \tag{2.10}$$

Most of the time the relative values ϵ_r and μ_r are used in formulas and tables, these are dimensionless numbers. The relative electric permeability ϵ_r is also known as the dielectric constant.

If we now modify equations 2.5 and 2.6 to

$$E_x = E_0 \cos(\omega t - kz), E_y = E_z = 0 \tag{2.11}$$

$$B_y = \frac{E_0 \sqrt{\epsilon_r \mu_r}}{c} \cos(\omega t - kz), B_x = B_z = 0 \tag{2.12}$$

the ratio of amplitudes of the electric and magnetic fields goes from

$$B_0 = \frac{E_0}{c} \text{ to } B_0 = \frac{E_0 \sqrt{\epsilon_r \mu_r}}{c} \tag{2.13}$$

meaning that the wave velocity changes to

$$v = \frac{\omega}{k} = \frac{c}{\sqrt{\epsilon_r \mu_r}} \tag{2.14}$$

and is now called the phase velocity of the wave which in turn defines the refractive index of the medium as

$$n = \frac{c}{v} = \sqrt{\epsilon_r \mu_r} \tag{2.15}$$

As we can see the behaviour of electromagnetic waves in a medium is dependent on the refractive index. For most natural media, except ferro or ferrimagnetic materials, the relative magnetic permeability μ_r can be assumed to be 1. The relative electric permittivity of natural media on the other hand varies from approximately 1 for air to 88 for water at 0°C [16].

If the material absorbs energy the dielectric constant is a complex number, this can either be put as $\epsilon_r = \epsilon' - i\epsilon''$ or as a complex refractive index $n = n' - in''$. If we now consider an electric field using complex exponential notation

$$E_x = E_0 e^{i(\omega t - kz)} \tag{2.16}$$

which is equivalent to the x component in 2.5. Using equations 2.14 and 2.15 we can now substitute

$$k = \frac{\omega}{c}(n' - in'') \tag{2.17}$$

into 2.16 and we get a simple harmonic wave whose amplitute decreases exponentially with z

$$E_x = E_0 e^{-\frac{\omega n'' z}{c}} e^{i(\omega t - \frac{\omega n' z}{c})} \tag{2.18}$$

The distance this wave has to travel so that the power $|E|^2$ is reduced by a factor of e is called the absorption length l_a and is given by

$$l_a = \frac{c}{2\omega n''} \tag{2.19}$$

If we ignore scattering and other reasons for energy loss this distance gives a good estimate of how far electromagnetic radiation will propagate through a material before its intensity is significantly reduced.

2.1.2 Reflection and Transmission

When electromagnetic radiation encounters a plane boundary between two uniform homogeneous media a part of it is reflected and the other transmitted. The law of reflection states that the angle of incidence is equal to the angle of reflection (Fig.2.1) while the angle of the refracted (transmitted) wave depends on the ration of the 2 refractive indexes (Snell's law of refraction).

$$n_1 \sin\theta_1 = n_2 \sin\theta_2 \tag{2.20}$$

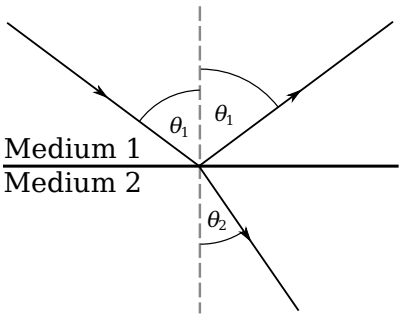

Figure 2.1 – Reflection and Transmission of a plane wave on a plane boundary

Fresnel equations

We also want to know how much of the energy of the wave is transmitted or reflected, this is where the reflection and transmission coefficients come into play. These are defined as a fraction of the electric field amplitude of the incident radiation. Since these coefficients depend on the polarisation of the incident radiation we must split them into parallel ($\parallel$) and perpendicular ($\perp$), or as is also common in remote sensing, vertical and horizontal, polarisations (Fig.2.2). Any combination of these polarisation states can be calculated by splitting it into these components.

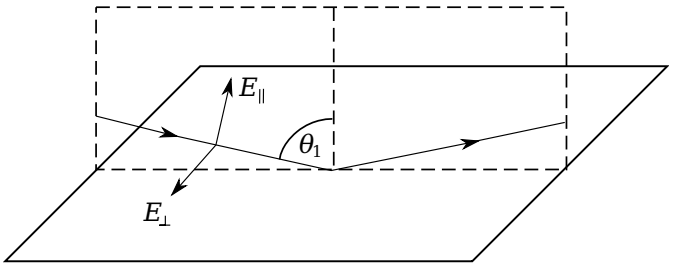

Figure 2.2 – Illustration of parrallel (vertical) and perpendicular (horizontal) polarized electromagnetic radiation, reflected from a plane boundary

The Fresnel equations are solutions of Maxwell's equations solved at the boundary. For non magnetic materials ($\mu_r = 0$) and if medium 1 has a refractive index of 1, which is a good approximation for air and the case in most remote sensing scenarios, then the reflection and transmission coefficients are given by

$$r_\perp = \frac{\cos\theta_1 - \sqrt{\epsilon_{r2} - \sin^2\theta_1}}{\cos\theta_1 + \sqrt{\epsilon_{r2} - \sin^2\theta_1}} \tag{2.21}$$

$$t_\perp = \frac{2\cos\theta_1}{\cos\theta_1 + \sqrt{\epsilon_{r2} - \sin^2\theta_1}} \tag{2.22}$$

$$r_\parallel = \frac{\sqrt{\epsilon_{r2} - \sin^2\theta_1} - \epsilon_{r2}\cos\theta_1}{\sqrt{\epsilon_{r2} - \sin^2\theta_1} + \epsilon_{r2}\cos\theta_1} \tag{2.23}$$

$$t_\parallel = \frac{2\sqrt{\epsilon_{r2}}\cos\theta_1}{\sqrt{\epsilon_{r2} - \sin^2\theta_1} + \epsilon_{r2}\cos\theta_1} \tag{2.24}$$

Transmission through the Atmosphere

Different molecules absorb different wavelengths of electromagnetic radiation. Because of that some frequencies are nearly completely absorbed by the atmosphere while others pass nearly unimpeded through it. Figure 2.3 shows the transmission coefficient of electromagnetic waves trough the atmosphere. For the microwave spectrum it can be seen that atmospheric absorption becomes a problem when wavelengths get smaller than 2cm. The C-Band, which is defined from 4-8 GHz (3.8 - 7.5 cm), is therefore suitable for all weather situations (Figure 2.4) since neither cloud coverage nor rainfall have big influence on the transmission coefficient [2].

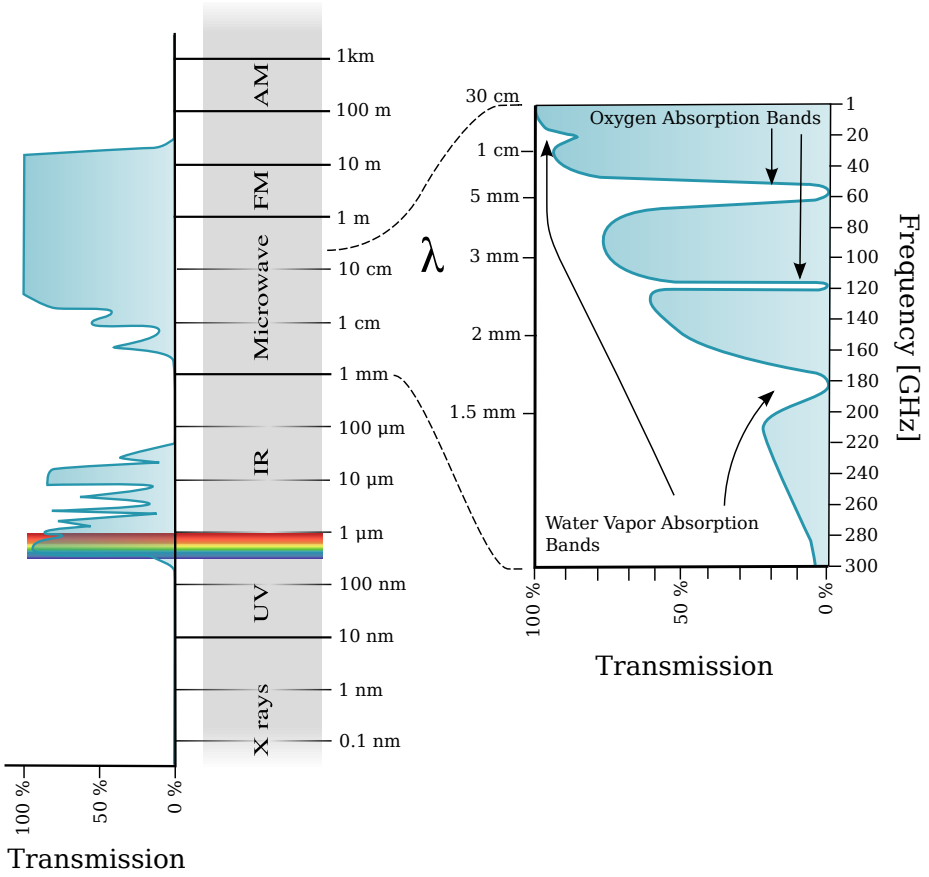

Figure 2.3 – Transmission of electromagnetic waves through the atmosphere, combination of graphics from [1] and [2]

2.2 Dielectric properties of Water, Soil and Snow

This section gives a short overview of the dielectric properties of natural media most important to freeze/thaw processes, such as water, soil and snow.

2.2.1 Water

The distribution of electric charges in a water molecule is asymmetric (Fig 2.5), the 2 hydrogen atoms and the oxygen atom form two covalent bonds with an interior angle of 104.45°. Because of that, liquid water shows orientational polarization and an unusually high dielectric constant of about 80 (at 20°C) which is the fundamental reason why water is so important in microwave remote sensing.

Water molecules align, on average, in the direction of the applied electric field. The relaxation time measures the average orientation time of a water dipole subjected to viscous drag. This classical view is challenged by other explanations involving quantum processes [17]. As liquid water cools down and freezes the polarization effects are lost and ice behaves distinctly different than liquid water, this is also shown by the fact that the relaxation frequency of water is approximately 9 GHz (Fig.2.6), whereas that of ice is in the kilohertz range [18].

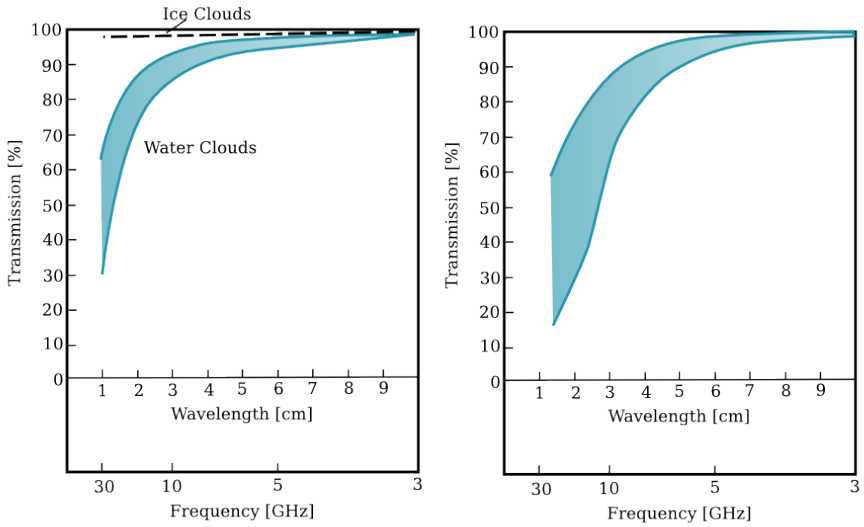

Figure 2.4 – Influence of clouds (left) and rain(right) on transmission of microwaves [2]

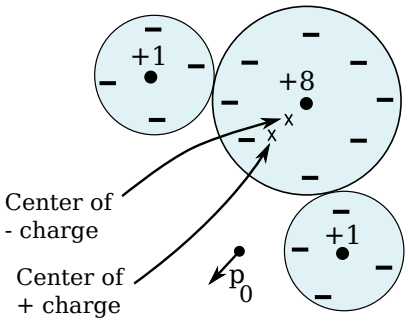

Figure 2.5 – Water molecule with it's permanent dipole moment p_o (after [3])

2.2.2 Soil

Soil is usually a mixture of soil particles (also called the matrix of the soil), air voids and liquid water [2]. The water content is the most dominant factor in determining the dielectric properties of soil [19], it is divided into two fractions, bound and free water. Bound Water refers to the water molecules in the first molecular layers of the soil particles bound to them through matric forces [20]:

- direct adhesion of water molecules to soil particles through London-van der Waals forces
- capillary binding
- osmotic binding of water in double layers

The relative amount of water bound through these forces varies with soil type. Since bound water cannot move freely its dielectric properties are dissimilar to that of free water.

Figure 2.7 shows that the dielectric constant changes rapidly when freezing occurs and that this effect is very dependent on the moisture content of the soil.

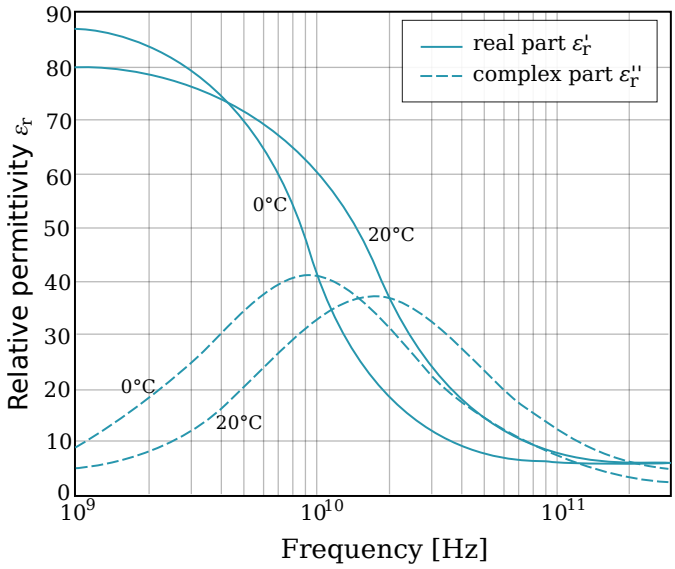

Figure 2.6 – Relaxation spectrum of water at 0 and 20°C (simplified after [4])

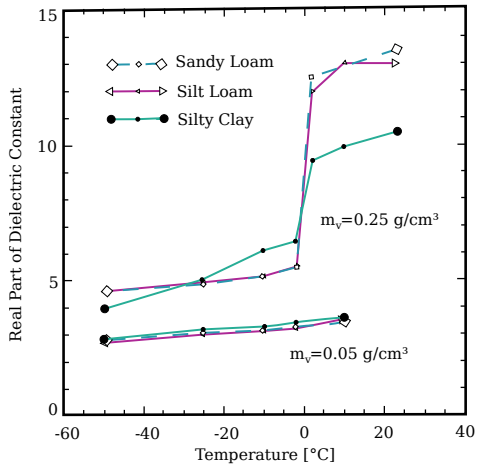

Figure 2.7 – Effect of freezing on dielectric constant of soil for two different moisture contents m_v (after [5])

2.2.3 Snow

The dielectric characteristics of snow are not easily described because they are, again, very dependent on the water content of snow. Dry snow is a mixture of ice particles and air voids whereas wet snow also contains liquid water. Wet snow has two distinct regimes of liquid saturation [21, 22]. In the pendular regime, which is equivalent to low wetness, water occurs as isolated inclusions while air is continuous throughout the snow. In the funicular regime (high wetness), the water is continuous throughout the pore space and the air occurs in distinct bubbles. The change from on regime to the other happens at about 10 to 20 % of saturation [23].

Additional complexity is added because melting and refreezing of snow change the microstructure and the grains become rounded or disappear completely. The dielectric constant of snow depends, in general, on temperature, volumetric water content, snow density, ice particle shape and shape of the water inclusions [18].

The dielectric constant of dry snow increases almost linearly with increasing snow density whereas the real and imaginary part of the dielectric constant of wet snow increase with water content as long as the snow is in the pendular regime.

2.3 Scattering

Not only the dielectric properties of a medium influence the interaction of electromagnetic radiation with it, also the size, geometry and roughness of an object or a surface in relation to the wavelength of the EM wave are important factors. If we imagine a sphere with a circumference $2\pi a$ that is much larger than the wavelength λ, ($2\pi a \gg \lambda$), then the EM wave will act as if it were a surface and we can use the Fresnel equations (see 2.1.2). This is also referred to as the optical region or non-selective scattering. In the other extreme case where the sphere is much smaller than the wavelength ($2\pi a \ll \lambda$), this is referred to as Rayleigh scattering and is for instance important when microwaves are scattered by spherical water droplets in the atmosphere. The region between these extreme cases is called Mie scattering where resonant effects occur (see Fig. 2.8) [7].

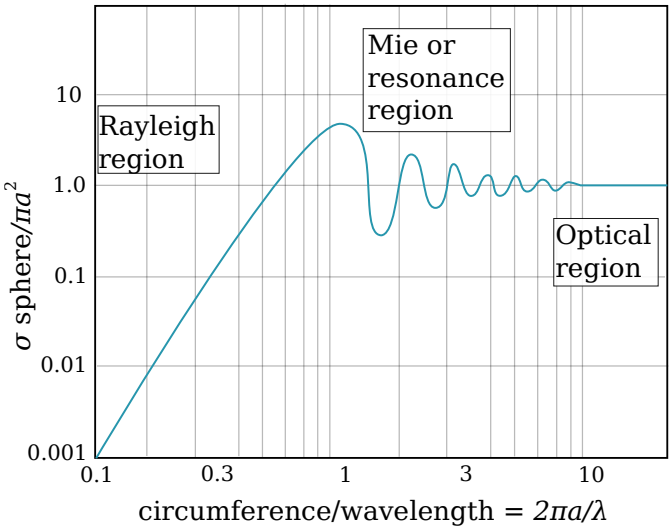

Figure 2.8 – The transition from Rayleigh to optical scattering (after [7])

If the surface, that a EM wave encounters, is rough in relation to is wavelength the scattering characteristics change from specular to diffuse reflection (Fig. 2.9). The roughness of a surface is defined using the standard

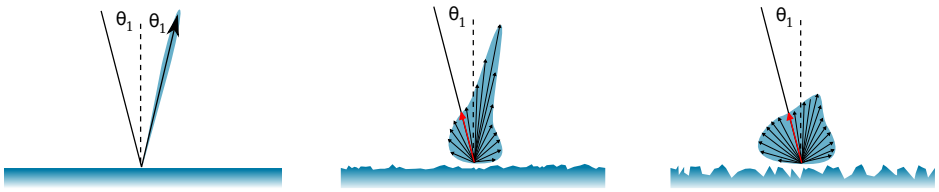

Figure 2.9 – From left to right: specular to diffuse scattering depending on the surface roughness (after [6])

deviation of the height deviation h from the mean height $\bar{h}$. The question is how big can h be before a surface should be considered "rough". The rayleigh criterion states that if

$$h < \frac{\lambda}{8 \cos \theta_i} \tag{2.25}$$

the surface should be considered rough, with θ_i as the incidence angle. This means that the average phase difference due to h is less than $\pi/2$. If the phase difference becomes larger the scattered waves are no longer coherent and diffuse reflection will gain the upper hand. The rayleigh criterion is only useful for a first-order classification of the smoothness of a surface. The stricter Fraunhofer criterion is more useful for microwave wavelengths, it states that

$$h < \frac{\lambda}{32 \cos \theta_i} \tag{2.26}$$

This means that the phase difference is less than $\pi/8$.

All of the above is only valid for randomly rough surfaces, if the height variations exhibit a periodic pattern Bragg scattering can occur, this means that the ordered structure of the surface leads to scattered waves which will combine constructively in some directions and destructively in others.

2.4 Radar Equation

Radar scatterometers send out an electromagnetic wave and measure the energy of the returning wave that was scattered backwards from the earth's surface.

$$P_r = \frac{P_t A_{eff}^2}{4\pi\lambda^2 R^4}\sigma \tag{2.27}$$

The (monostatic) radar equation [2] (2.27) describes how the received power P_r depends on the technical characteristics of the radar system,

P_t transmitted power

A_{eff} effective area of the Antenna

λ wavelength

the distance between radar and object R, and the cross section of the object σ. The radar equation is not formulated for area extensive targets [16, 24]. The illuminated surface is considered to be composed by an infinite collection of targets with a differential sized cross section $d\sigma$. $d\sigma$ can then be rewritten as the product of the *backscattering coefficient* σ° and the differential area da of the target. The backscattering coefficient is defined as the radar cross section per unit area with the unit $m^2 m^{-2}$ but it is commonly expressed in decibels (dB):

$$\sigma^\circ(dB) = 10 \cdot log\sigma^\circ(m^2 m^{-2}) \tag{2.28}$$

Equation 2.27 changes to

$$P_r = \iint_A \frac{P_t A_{eff}^2}{4\pi\lambda^2 R^4}\sigma^\circ da \tag{2.29}$$

when applied to an area extensive target with an area of A. The received power P_r is converted to the backscattering coefficient σ° in order to obtain information about the target.

3

Datasets

In the following chapter the datasets used for deriving the freeze/thaw state as well as those used for validation are summarized. It also includes a basic description of the ASCAT Sensor and the data processing done to the observations before using them for freeze/thaw detection.

3.1 ASCAT onboard Metop

The Advanced Scatterometer (ASCAT) is a C-Band(5.255 GHz in VV-polarisation) Scatterometer on-board the Metop A satellite. It is part of the EPS (EUMETSAT Polar System) programme which itself is part of a joint European-American system of polar-orbiting satellites, the Initial Joint Polar System (IJPS) [6]. It provides near global coverage in five days with a spatial resolution of 50 (regular product) and 25 km (experimental product, used at IPF), using three antennas for each of it's two 550 km wide swaths (see Figure 3.1).

Each of the 2 swaths consists of 3 antennas with azimuth angles of 45°, 90°and 135°(fore, mid and after beams). The incidence angles are approximately 34 - 64°for fore and after beams and 25 - 53°for the mid beam.

3.1.1 Discrete Global Grid

For further processing the measurements of the ASCAT sensor are resampled to a Discrete Global Grid (DGG) at IPF. This DGG is based on the GEM6 (Goddard Earth Model) ellipsoid, which is divided in equally (12.5km) spaced latitude small circles. On each of these small circles a 12.5km longitudinal spacing defines the grid points. For a more detailed explanation as well as a comparison to other possible grids see [6].

The grid contains a grand total of 3264391 grid points but only 839826 of them are routinely processed because oceans, inland water bodies and areas covered with permanent ice are excluded from the analysis.

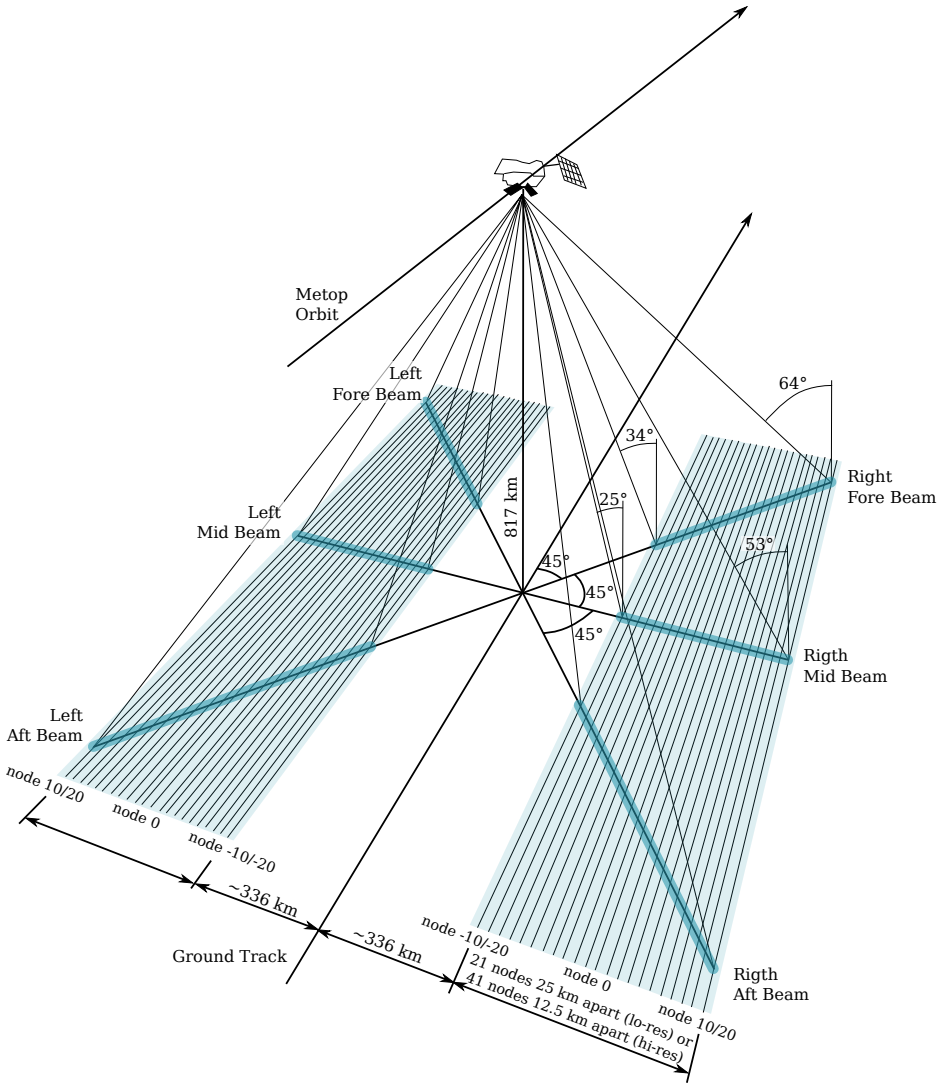

Figure 3.1 – Observation geometry of ASCAT on-board Metop (after [6])

3.1.2 Normalized backscatter

The ASCAT sensor takes the σ_o measurements at different incidence and azimuth angles. Because the intensity of the backscattered signal depends strongly on the incidence angle it is impossible to compare σ_o observations directly. Consequently the backscatter coefficients are normalized to a reference incidence angle of 40°according to

$$\sigma_i^\circ(40,t) = \sigma_i^\circ(\theta,t) - \sigma'(40,t)(\theta-40) - \frac{1}{2}\sigma''(40,t)(\theta-40)^2 \tag{3.1}$$

Where i marks one of the three beams while slope (σ') and curvature (σ'') are the first and second derivatives of σ°. The measurements of the 3 beams are then averaged to reduce the influence of instrument noise, speckle and azimuthal effects [25].

The reference angle is chosen based on the incidence angle range of the ERS Scatterometer (18-59°) and minimizes the extrapolation error [16].

3.2 WMO METEO stations

The WMO METEO station network dataset provides among other variables 24 hour minimum and maximum temperature. There are about 8900 actively reporting stations worldwide with widely varying periods of record. About 3150 stations provided data for the years 2007 and 2008 and are located in latitudes where freezing occurs (see Figure 3.2). The data was obtained from [26].

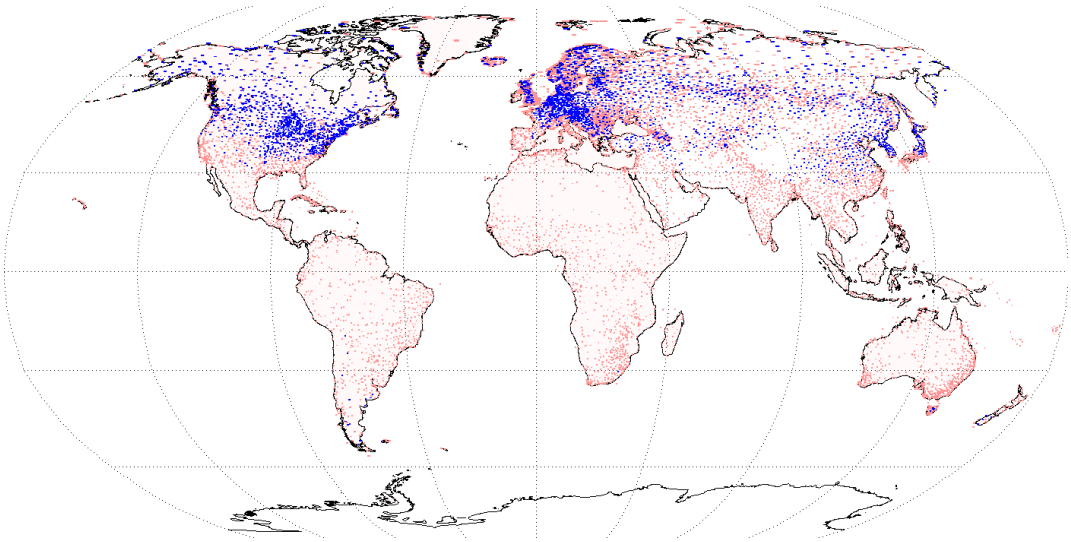

Figure 3.2 – WMO stations - red: all stations blue: stations with usable data

3.2.1 Interpolated data

Neither maximum nor minimum 24 hour temperature are a realistic representation of the real temperature at the time of the satellite overpass. A simple averaging doesn't provide realistic results. Because of that a more sophisticated approach was taken to get a good estimate of temperature. The diurnal temperature cycle is driven by the sun with the coldest temperature occurring around sunrise and maximum temperature a few hours after solar noon (see Figure 3.3). Because of that sunrise times and solar noon were calculated for every day and all stations, then minimum temperature was assumed at sunrise and maximum temperature 2h after solar noon.

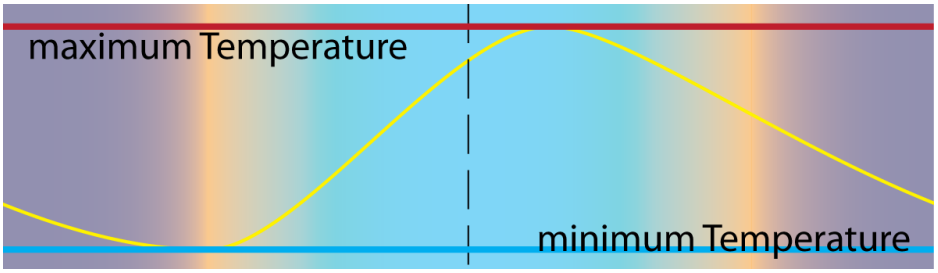

Figure 3.3 – Diurnal Temperature Cycle (approx.)

Station	Lat.	Lon.	Start	End
Nadym R1	65° 20’	72° 50’	2007-08-05	2008-08-08
R3 Marre Sale	69° 42’	66° 30’	2007-09-01	2008-09-01
R33 Borehole 3	65° 57’	75° 52’	2007-01-01	2007-07-09
Barrow	71° 19’	-156° 38’	2007-01-01	2008-05-31
Council Forest	64° 54’	-163° 40’	2007-01-01	2008-12-31

Table 3.1 – Overview of GTN-P stations

3.3 GTN-P borehole data

The Global Terrestrial Network for Permafrost (GTN-P) which combines the Circumpolar Active Layer Monitoring (CALM) network and the thermal state of permafrost (TSP) project [27]. The CALM in-situ station network has been established with more than 100 sites in 15 countries in both hemispheres, designed to observe the response of the active layer and near-surface permafrost to climate change. 5 Stations were used, 3 located in Siberia and 2 in Alaska (see Fig. 3.4). Table 3.1 lists the station details.

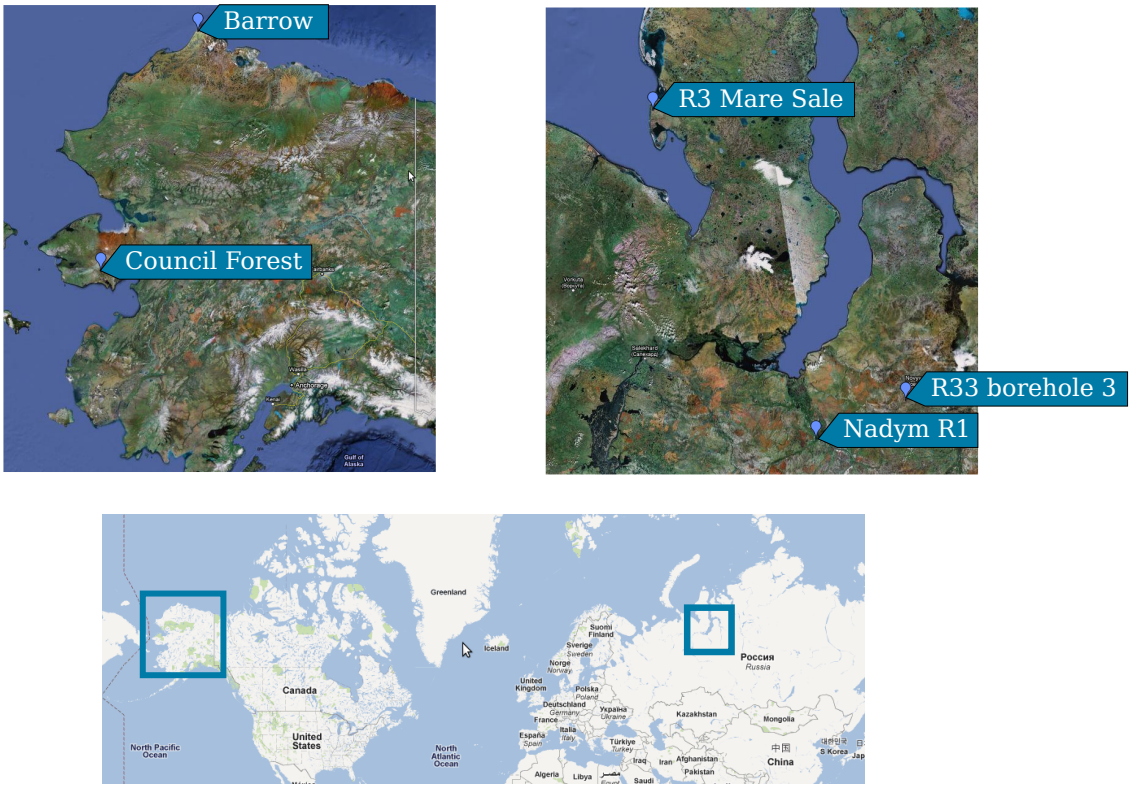

Figure 3.4 – Locations of the 5 GTN-P stations

3.4 Model data

Global Climate models provide continuous (1h-6h intervals are provided) coverage of various meteorological variables. For the validation only temperature variables were used but also the snow water equivalent was of interest for detailed analysis of single grid points.

3.4.1 ERA Interim

ERA Interim is a global atmospheric reanalysis dataset produced by the European Centre for Medium-Range Weather Forecasts (ECMWF). It provides data from 1989 to 31 October 2010 (as of writing of this thesis) but is constantly updated. The variables of interest where

- soil temperature of layer 1 (0-7 cm) in [K]
- 2 meter air temperature [K]

This data is available in 6h temporal resolution (0,6,12,18 UTC) on a reduced gaussian grid (ECMWF T255) [28] with 0.7°spatial resolution at the equator.

3.4.2 GLDAS-Noah

The GLDAS-Noah dataset is the output of the Global Land Data Assimilation System (GLDAS), a software package that can simulate several land surface models, simulating the Noah land surface model [29]. The variable of interest was

- Average layer 1 (0-10 cm) Soil temp. [K]

Data was available from February 2000 onwards in 3h temporal resolution (0,3,6... UTC) on a 0,25°regular grid.

3.5 Satellite data

3.5.1 Land Surface Temperature

Land Surface Temperature was available from 2 different sensors, MODIS and AATSR. Both datasets were provided by the permafrost project and are slightly modified from the original MODIS and AATSR products. The purpose of the permafrost project was to merge the datasets from MODIS and AATSR to derive a product with improved temporal coverage [30]. The provided data for this validation were the 8 day averages before merging the 2 products.

MODIS

MODIS or Moderate Resolution Imaging Spectroradiometer is a instrument which is carried onboard NASA's Terra and Aqua Satellites. In combination these 2 satellites observe the whole surface of the earth in 1-2 days. MODIS records data using 36 spectral bands providing different datasets to the scientific community of which only one is Land Surface Temperature [31].

The dataset provided by the permafrost project was a average of the observations made by Aqua and Terra. The accuracy of the 1km MODIS LST product is 1°K for cloud free observations [32].

Data was available in 2 test regions.

- Ob Estuary for the year 2008 as 8 day composite with 28 km resolution.
- North Siberia for the years 2007/2008 as 8 day composite with 28 km resolution.

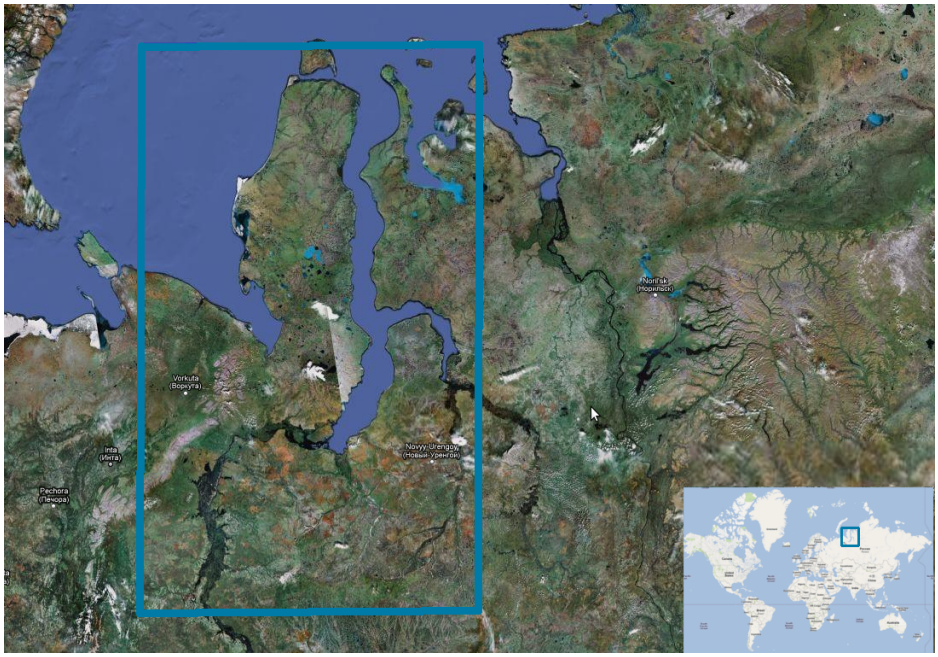

Figure 3.5 – Extent of Ob estuary region in northern siberia.

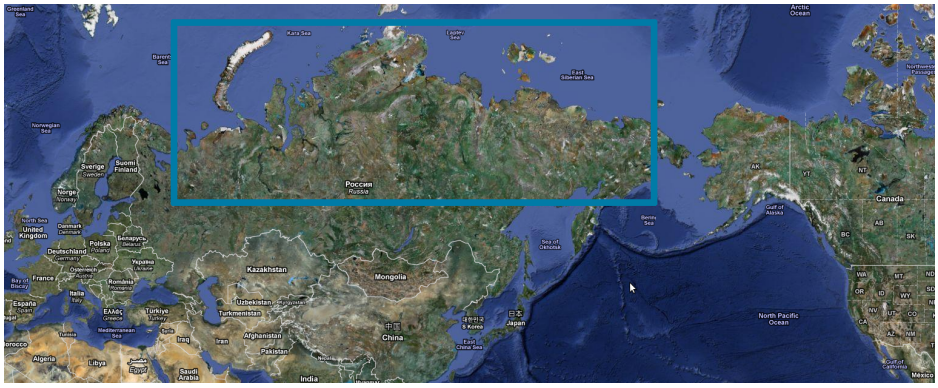

Figure 3.6 – Extent of North Siberia dataset.

AATSR

AATSR or Advanced Along-Track Scanning Radiometer is a sensor carried on-board ENVISAT, its main purpose is the measurement of Sea Surface Temperature (SST) but also LST can be derived. The accuracy is better than 0.5°K averaged over areas of 50km² for SST [33] and between 1 and 3°K for LST [34].

Envisat has a orbital period of 100.6 min, with a repeat cycle of 35 days, but in Arctic regions the revisit time is reduced to 3 days [30].

Data was available in the following test region.

- Kuparuk River (North Slope, Alaska) for the year 2008 as 8 day composite with 1km resolution.

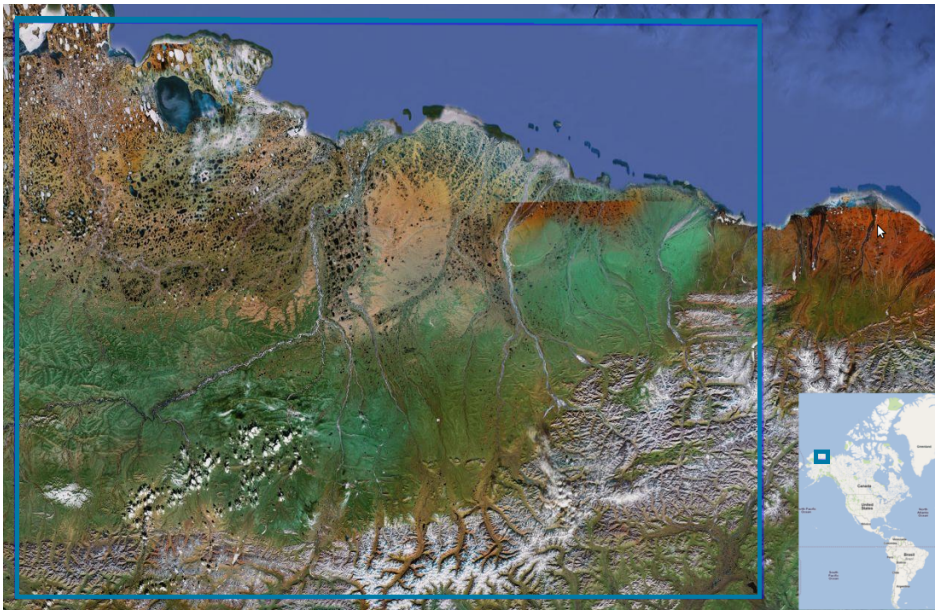

Figure 3.7 – Extent of Kuparuk river region in north slope Alaska

3.6 Probability Flags

These flags contain the probability of frozen ground, snow or ice cover for every day of the year in percent. This dataset was originally developed for flagging the freeze/thaw state of σ_{40} measurements and is distributed together with the ASCAT soil moisture dataset [35].

3.6.1 Frozen Probabilities

The frozen probabilities are based on the ERA40 reanalysis dataset and describe the probability of the temperature being below 0°C for a given day of the year.

3.6.2 Snow cover probabilities

Based on a historic 7 year analysis of SSM/I snow cover data this flag gives the probability of the occurrence of snow for a given day of the year.

3.7 Frozen probabilities from ERA-Interim data

Since the frozen probabilities distributed with the ASCAT soil moisture dataset are derived using the ERA40 model, a new dataset was produced using 20 years of ERA Interim temperature data. This was done so that the the same dataset is used for deriving the freeze/thaw thresholds (see chapter 4) and the ambiguity correction (see chapter 6).

The probability of frozen soil was computed for each day of the year using 20 years of ERA-Interim 2m air temperature between 1.Jan 1990 and 31.Dec 2009.The probabilities are given in percent based on how many of the data points had temperature values below 0° C.

This dataset can also be used to estimate the area of frozen ground. Fig.3.8 shows the maximum number of frozen days, meaning that if at least once in the 20 year period the temperature was below the freezing point of water this day is counted.

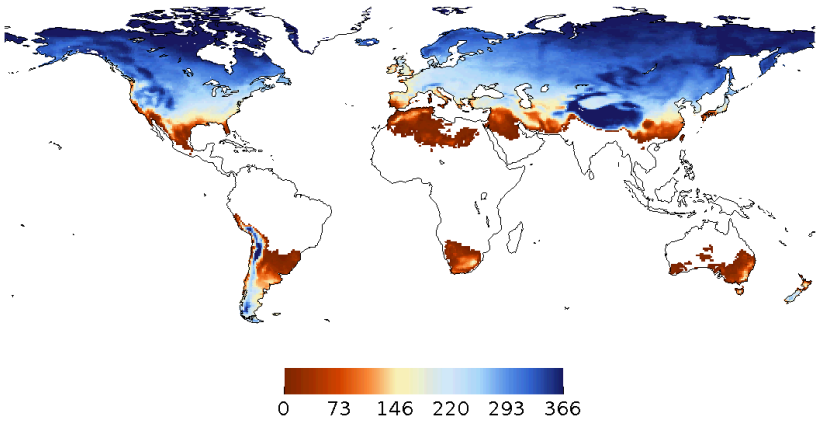

Figure 3.8 – Number of days in a year at which a temperature below 0°C was observed in 20 years of ERA-Interim data

Of the 839826 DGG grid points over land 489673 or 58.31 % had a day with temperatures below the freezing point of water. For the northern hemisphere this means that 69.93 % of the land area experienced freezing temperatures. This figure is higher than the estimate by [11], which states that approximately 57.1 % of the northern hemisphere are seasonally or intermittently frozen ground. This is to be expected since any day with a temperature below 0°C is included, regardless of how short this potential freezing was.

4

Freeze/Thaw detection using ASCAT Data

This chapter gives a summary of the freeze/thaw detection algorithm developed by [15].

Freeze/Thaw detection from ASCAT data is based on the variation of backscatter due to temperature changes, specifically due to the freezing of water in the ground. Fig. 4.1 shows the behaviour of normalized backscatter when freezing occurs. In the beginning of the year backscatter is at a more or less constant level while the temperature is well below 0°C and the snow cover is not changing. The 2 thawing periods in the end of April and May are characterised through very low backscatter, probably due to specular reflection [36] from water on the surface. In summer backscatter increases and is mainly dependent on soil moisture. In November temperature is dropping below the freezing point of water and backscatter decreases to winter levels that are equal to those observed in the beginning of the year.

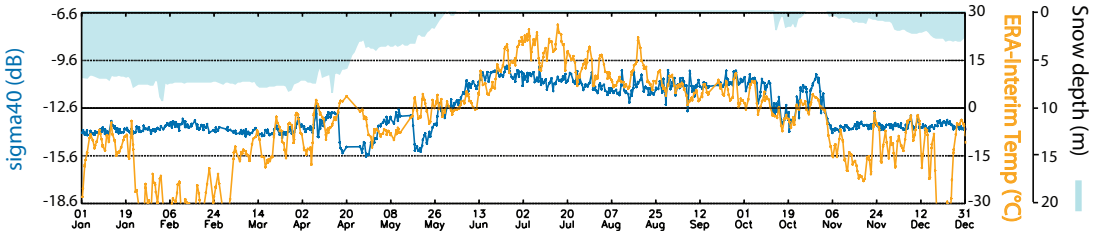

Figure 4.1 – Comparison of ASCAT σ^{40} backscatter measurements ERA-Interim 2m Air Temperature and WMO Meteo snow depth data over a grid point at 66.5037°E, 66.6924°N for the year 2007

The Freeze/Thaw product from ASCAT data is calculated in 2 steps. First the algorithm uses the distribution of backscatter measurements over temperature (see Fig.4.2) to find σ^{40} thresholds that define the freezing characteristics of one DGG point. In the second step these saved thresholds are used to find the freeze/thaw state for every ASCAT σ^{40} measurement. The result is the Surface State Flag (SSF), it's possible values are summarized in Table 4.1.

Flag Value	Surface State
255	Not Valid
0	Unknown
1	Unfrozen
2	Frozen
3	Temporary water surface / Melting conditions
4	Permanent ice / Frozen water body

Table 4.1 – Values of the Surface State Flag

4.1 Freeze/thaw parameters

The freezing characteristics of every DGG Point have to be defined in order to use σ^{40} for freeze/thaw detection. These characteristics can be described using the 9 freeze/thaw parameters.

Freeze level

The freeze level is defined as the inflection point of the logistic function (Figure 4.2) that is fitted to all σ^{40} measurements that lie between +10 and -10 °C. It's the most important characteristic because it is the basis of the separation of measurements into frozen and unfrozen.

If no logistic function can be fitted then the algorithm will not work. Fig.4.3 shows where the algorithm can find a freeze level. The Gobi and Taklamakan deserts immediately stand out as problem areas. The algorithm can not work there since little difference in backscatter is observed, because the soil is very dry and does not change its backscatter characteristics significantly when freezing. Another easily spotted problem area is the Sichuan basin in south western China, it can be seen in Fig.4.3 as a white nearly circular area east of the Himalaya Mountains.

Fig.4.4 shows the correlation coefficient between backscatter and ERA Interim air temperature. Comparing Fig 4.4 and Fig 4.3 shows that the algorithm is more likely to not produce a freeze level if the correlation coefficient is low. This is not too surprising since a dependence of backscatter on temperature is the basis of the algorithm. In chapter 5 we will see that the quality of the flagging also depends on the strength of this relationship.

Compared to the map of freezing extent derived from ERA-Interim data (Fig. 3.8), it can be easily seen that the algorithm also fails when there are only very few measurements taken during frozen conditions, this is not surprising since the algorithm only starts fitting a logistic function if more than 10 measurements were taken when temperatures were below 0°C. The freeze level can be determined for 327600 grid points or 66.9 % of the 489673 that experienced freezing temperatures (see Chapter 3.7). This figure seems a little low but it has to be considered that the estimate from ERA-Interim data takes into account every temperature below 0°C in a 20 year period which leads to an overestimation of frozen area.

For the northern hemisphere [11] provides an estimate of seasonally ($48.12 \cdot 10^6 km^2$), and intermittently ($6.27 \cdot 10^6 km^2$) frozen ground, which together are approximately $54.39 \cdot 10^6 km^2$. There are 294367 grid points with a valid freeze level north of the equator which, multiplied by the area of a DGG point, represent about $46 \cdot 10^6 km^2$. So the algorithm works for 84.6% of the area indicated by [11].

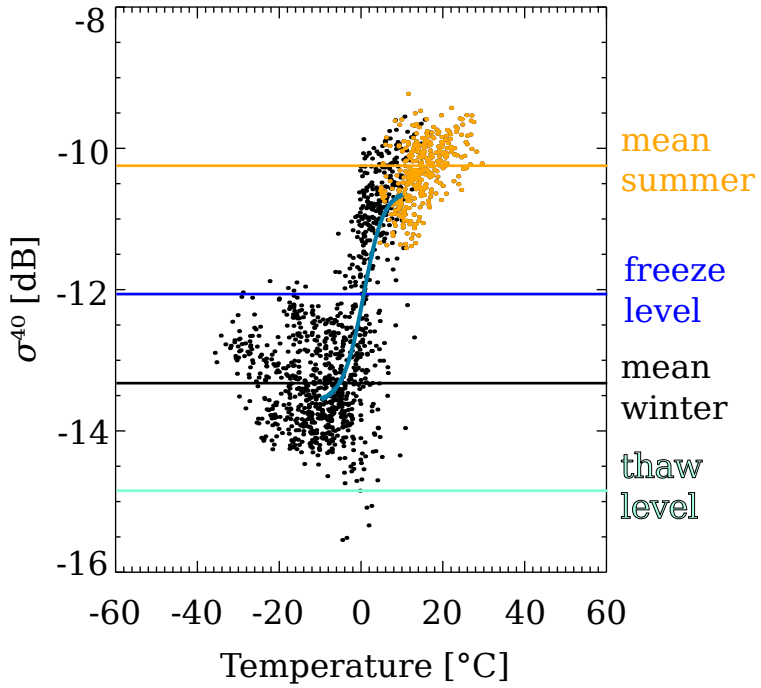

Figure 4.2 – Scatterplot of ERA Interim Temperature and σ^{40}

Permanent ice flag

If the logistic function shows declining behaviour this flag is set. It means that there is higher backscatter in Winter than in Summer. As the name of the flag indicates this should only happen in ice covered areas. Backscatter in these areas drops when the ice is melting in summer and is generally higher in winter when the ice is frozen.

Thaw level

In order to calculate the thaw level the backscatter measurements are limited to those that lie between -20 and +5 °C. From this subset, the interquartile range (iqr) and the quartiles(q1-3) are calculated. All measurements whose backscatter is less than $q1 - iqr$ are flagged as outliers and the maximum of these outliers is the thaw level. If no outliers are detected then the thaw level is set to the minimum σ^{40} measurement.

This procedure ensures that if there are significantly low backscatter values(which means water on the surface/specular reflection) the SSF is not set to simply unfrozen or frozen but also thawing conditions are recognized.

Sig_slop_minust

This parameter is the slope of a regression line fitted to all backscatter measurements occurring when temperatures are between -5 and -35 °C. It is used to determine if σ^{40} increases with decreasing temperature, this is an indicator for volume scattering when the ground is covered with a layer of snow.

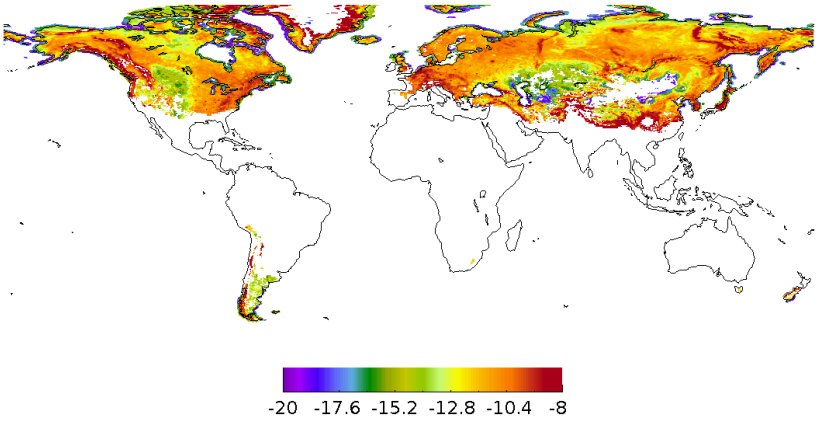

Figure 4.3 – Backscatter value of the freeze level in dB

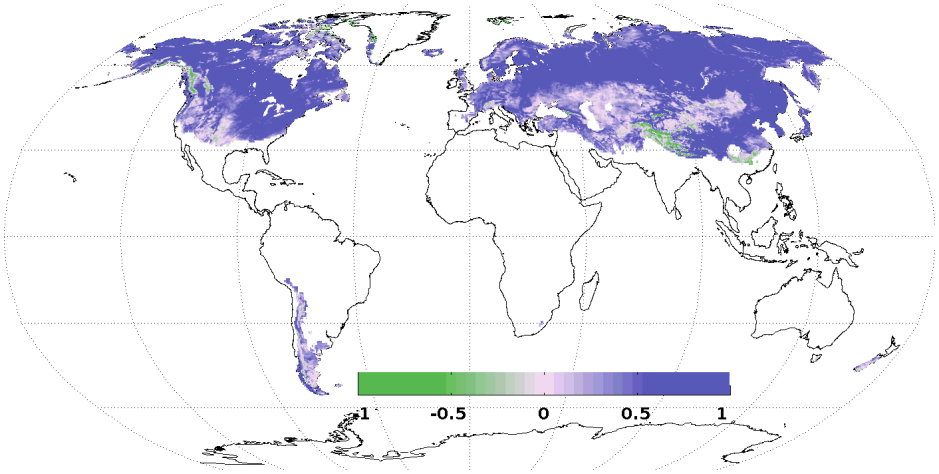

Figure 4.4 – correlation coefficient between backscatter and ERA Interim air temperature

Mean values of backscatter

Mean values of backscatter (msig_summer & msig_winter) in summer (June, July, August) and winter (December, January, February) are mainly used to determine if there is enough difference in σ^{40} between summer and winter in order to calculate the SSF. The months which are considered winter/summer are switched for grid points in the southern hemisphere.

Transition days

The 2 Transition days (pt1_doy & pt2_doy) are calculated using a step function (Figure 4.5). The first transition day is assumed to occur during the first 213 days of the year and the second transition day should occur in the last 213 days. For finding the transition from winter to summer the step function has a the value of msig_winter before, and msig_summer after the step. Quadratic residuals are calculated 213 times while shifting the position of the step by 1 day each time. The minimum of the residuals is the most likely day of transition. The inverse step function is used for finding the transition between winter and summer while calculating the quadratic residuals for the last 213 days of the year.

These 2 days also define winter, summer and the transition periods (Figure 4.6).

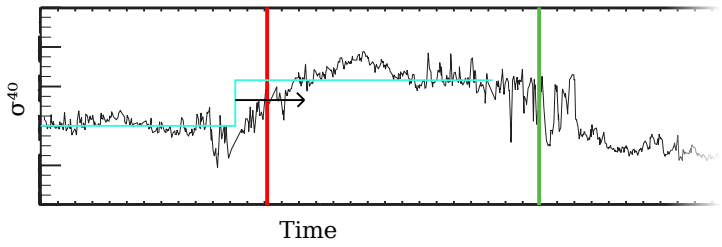

Figure 4.5 – σ^{40} Timeseries with stepfunction(lightblue), pt1(red) and pt2(green)

Standard deviation of backsatter during freezing

Standard deviation of σ^{40} measurements in Winter (as defined by pt1/2) that where taken when temperatures were below 0 °C and that are between freeze and thaw level (sig_stdev_frozen). This parameter is used to check if any change in backscatter in winter is statistically significant, especially for calculation of the deepsnow flag.

4.2 Other parameters

The 9 Freeze/Thaw parameters are stored for every DGG point and used in the decision trees. The following parameters are calculated for each backscatter measurement.

Deepsnow flag

The deepsnow flag is set to true if $-30 * sig\_slop\_minust > 2 * sig\_stdev\_frozen$. This indicates a significant increase in backscatter with decreasing temperature.

Time period

Every σ^{40} measurement is assigned a time period according to Figure 4.6. The observation time plays a critical role in the interpretation of the measurements.

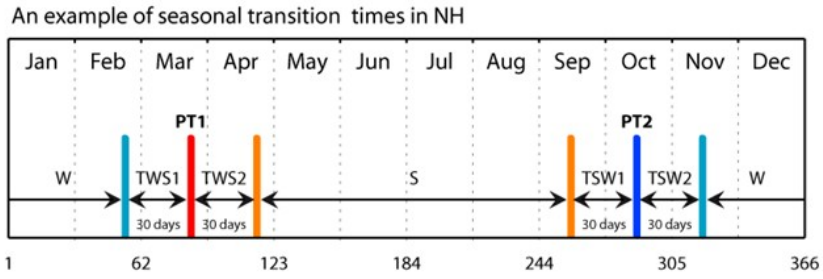

Figure 4.6 – Definition of winter, summer and transition periods

4.3 Decision Trees

There are 3 decision trees, each is applied in one of the following cases.

Decision Tree 1: mean of backscatter in summer greater than mean of backscatter in winter or deepsnow flag is set, permanent ice flag is not set

Decision Tree 2: mean of backscatter in summer less than mean of backscatter in winter, permanent ice flag is not set

Decision Tree 3: permanent ice flag is set

Decision Tree 1 is the most prominent (Figure 4.7) since a positive relationship between σ^{40} and temperature measurements is expected to be most common.

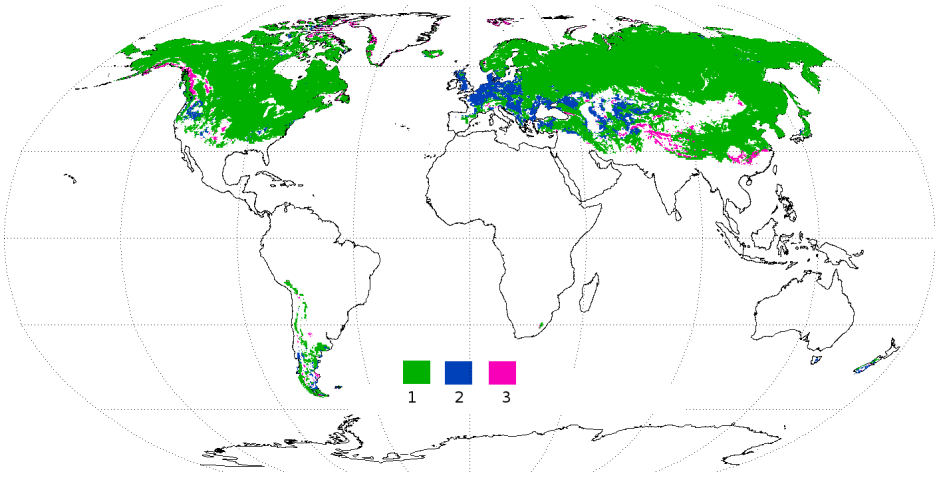

Figure 4.7 – Global distribution of decision trees (1-green,2-blue,3-pink)

Decision Tree 1

Figure 4.8 shows the decision making process for Decision tree 1. The upper part shows the classification in regard to the different thresholds explained previously. Every measurement that falls into the red area will be classified using the previous SSF via the red table.

This is the basic classification but there are some special rules for a rapid increase or decrease of the σ^{40} timeseries shown in yellow. An rapid increase of backscatter results in a SSF that shows unfrozen conditions. A rapid decrease results in a SSF that shows frozen ground unless it happens in transition time 1, the previous SSF also showed frozen conditions and the backscatter measurement is below the $freezelevel - 2 * \sigma\_noise$. These rules are overruled if the σ^{40} measurement is in the temporary melting class (shown in green).

Decision Tree 2

Decision Tree 2 differentiates only between 2 time windows. Figure 4.7 shows that this decision tree is mainly used in temperate climate like Europe. In this regions there are a lot of dry conditions in summer which should not be flagged as frozen. This is the reason why the red table is very conservative with flagging a measurement as frozen. A rapid increase indicates unfrozen and a rapid decrease indicates frozen conditions, but not in summer because of the aforementioned reasons.

Decision Tree 3

Decision Tree 3 is only used in areas that are probably covered with ice (Figure 4.7) and show higher backscatter in winter than in summer (Figure 4.10). The SSF can only have the 'unfrozen' value in a narrow window between the freeze and the thaw level or if there's a rapid decrease in σ^{40} during winter. This means that most of the measurements in these areas will not be suitable for SWI calculation.

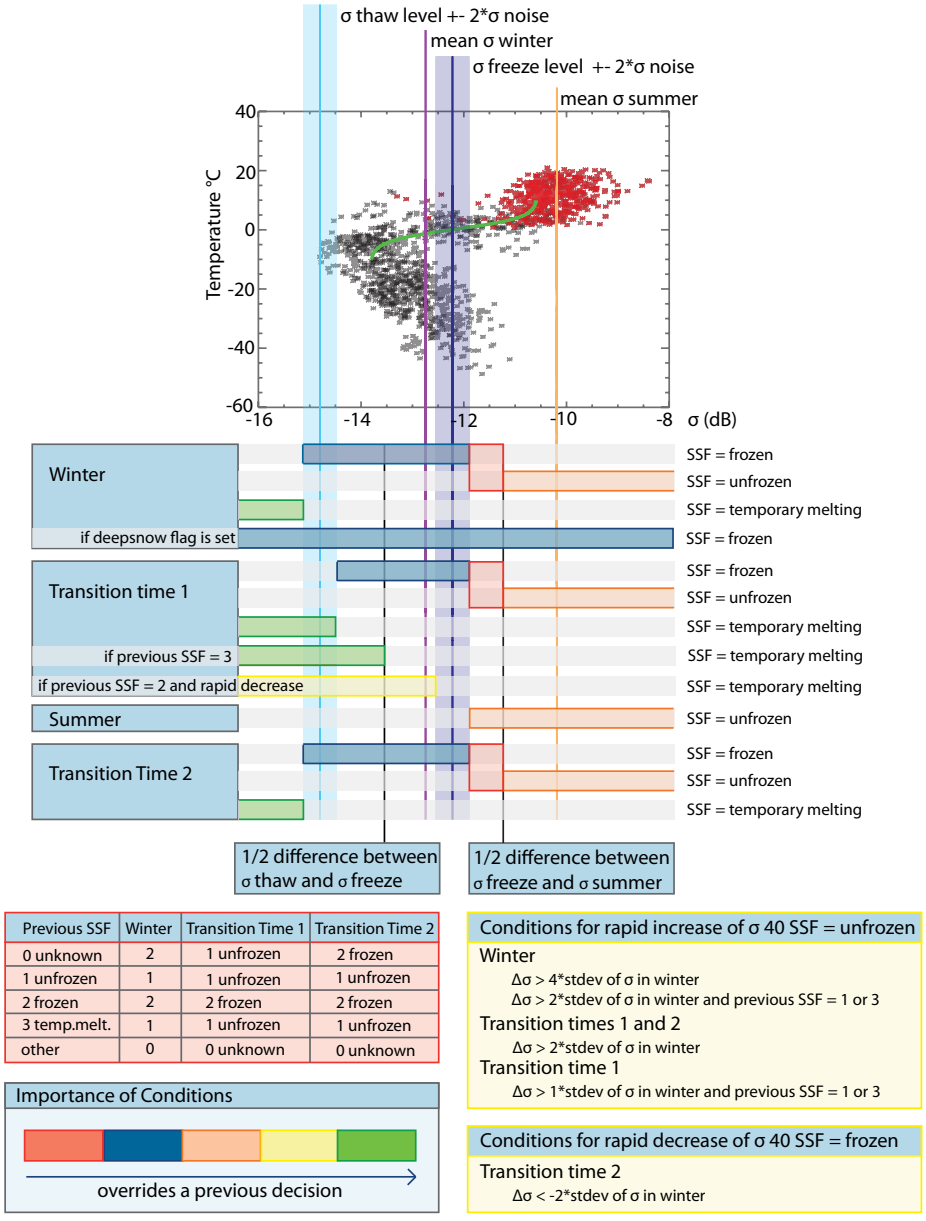

Previous SSF	Winter	Transition Time 1	Transition Time 2
0 unknown	2	1 unfrozen	2 frozen
1 unfrozen	1	1 unfrozen	1 unfrozen
2 frozen	2	2 frozen	2 frozen
3 temp.melt.	1	1 unfrozen	1 unfrozen
other	0	0 unknown	0 unknown

Importance of Conditions

overrides a previous decision

Conditions for rapid increase of σ 40 SSF = unfrozen

Winter

Δσ > 4*stdev of σ in winter

Δσ > 2*stdev of σ in winter and previous SSF = 1 or 3

Transition times 1 and 2

Δσ > 2*stdev of σ in winter

Transition time 1

Δσ > 1*stdev of σ in winter and previous SSF = 1 or 3

Conditions for rapid decrease of σ 40 SSF = frozen

Transition time 2

Δσ < -2*stdev of σ in winter

Figure 4.8 – Decision Tree 1

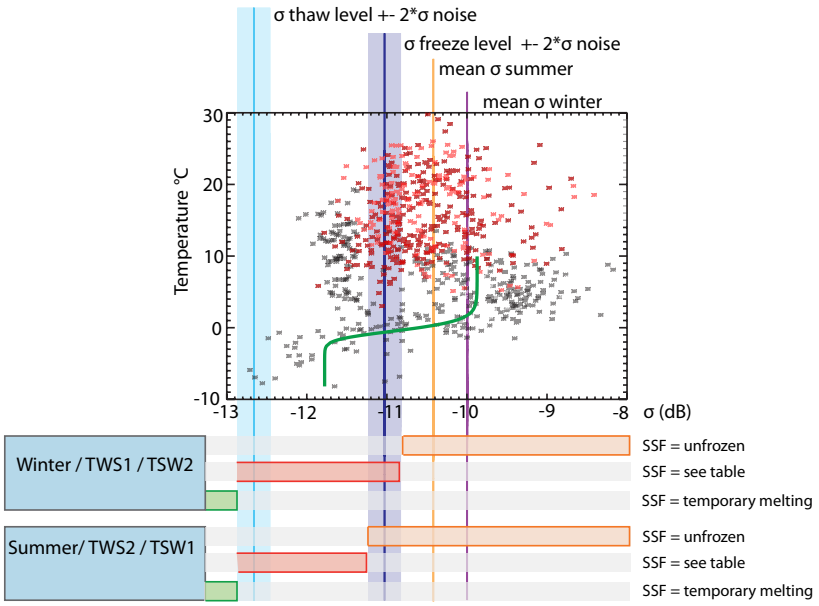

Previous SSF	Winter / TWS1 / TSW2	Summer/ TWS2 / TSW1
0 unknown	0 unknown	0 unknown
1 unfrozen	0 unknown	1 unfrozen
2 frozen	2 frozen	0 unkown
3 temp.melt.	1 unfrozen	1 unfrozen
other	0 unknown	0 unknown

Conditions for rapid increase of σ 40

Winter / TWS1 /TSW2

Δσ > 2*stdev of σ in winter -> SSF 1 unfrozen

Summer/ TWS2 / TSW1

Δσ > 2*stdev of σ in winter -> SSF 1 unfrozen

Conditions for rapid decrease of σ 40

Winter / TWS1 /TSW2

Δσ < -2*stdev of σ in winter -> SSF 2 frozen

Summer/ TWS2 / TSW1

Δσ < -2*stdev of σ in winter -> SSF 0 unknown

Importance of Conditions

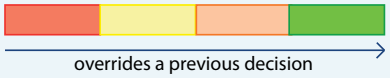

Figure 4.9 – Decision Tree 2

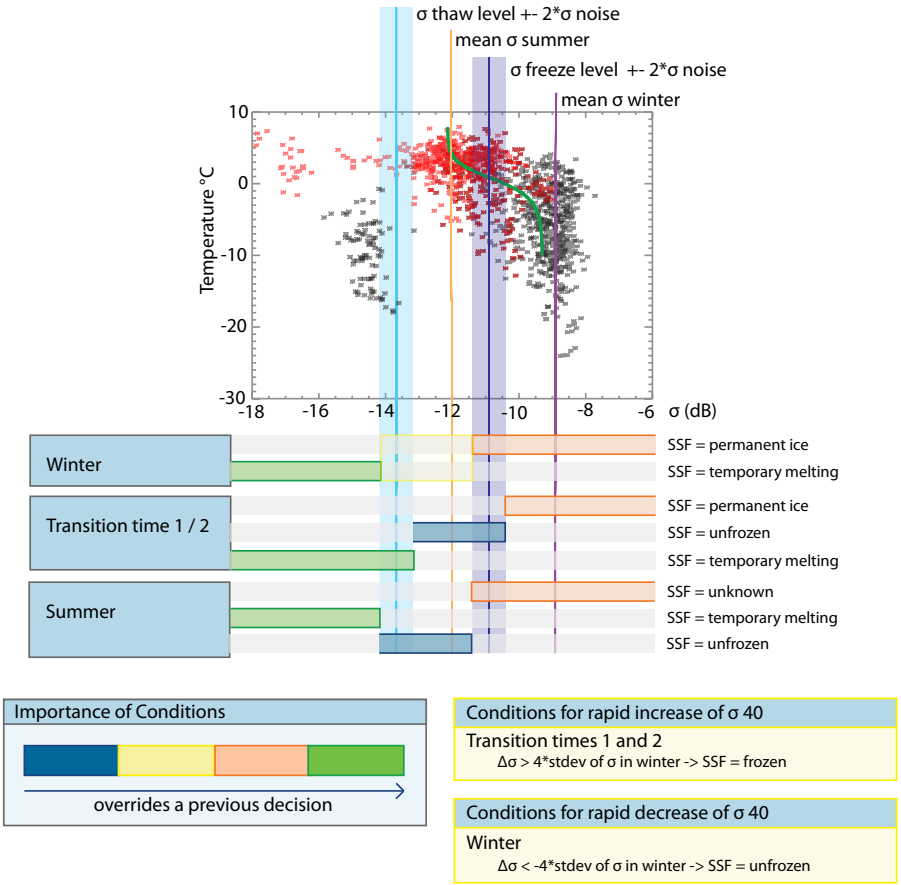

Figure 4.10 – Decision Tree 3

5

Validation

In the following sections the validation results are discussed. First the methods used for validation and the classification of the errors will be explained, secondly the validation with the global temperature datasets will be discussed, followed by the comparisons with GTN-P stations and other satellite products.

5.1 Method

The validation of freeze/thaw states is not easy since there are no global in-situ measurements of the freeze/thaw state of the soil available. Temperature datasets have to be used which introduce accuracy errors of their own and don't necessarily represent the actual freeze/thaw state of the ground. Data from 1.January 2007 until 31.December 2008 was used for validation since the SSF is based on observations from this period. ERA-Interim and GLDAS-Noah were available globally for the whole timespan. WMO Meteo stations provided useful data in a lot of cases (see Fig. 3.2). The accuracy of the algorithm varies greatly with the seasons, because of this behaviour the datasets where split into 4 time intervals according to chapter 4.1.

Before any validation of the SSF with temperature data could be made, the datapoints that are most suitable for comparison had to be found. For ERA Interim and GLDAS the nearest datapoint on the respective grid was searched for every DGG point. In the case of WMO meteo data and the GTN-P stations, the nearest DGG point for every station was searched. The distances were calculated on a spherical earth with a radius of 6371 km. After a suitable timeseries was found the temperature data was interpolated to the ASCAT σ_{40} observation time and then compared to the corresponding SSF.

For AASTR and MODIS land surface temperatures a different approach was needed since these datasets are 8 day composite images. The ASCAT observations and with it the Surface State Flag time series do not have a fixed temporal resolution. In order to compare the 8 day composite data with the SSF, the temporal resolution of the latter had to be changed to an 8 day, exponentially weighted, average. This was done by counting the occurrence of each SSF value and then weighing them exponentially by the time difference between the observation time and the point in time of the 8 day average. After that the value with the biggest weight is chosen as the value of the 8 day composite, if 2 values have the same weight then the SSF value of the previous 8 day composite is favored.

SSF	Frozen	Unfrozen
Temp. < 0°C	correct(true positive)	incorrect(false negative)
> 0°C	incorrect(false positive)	correct(true negative)
Invalid	% of unknown or not valid flags	
Correct	sum of correct measurements	

Table 5.1 – Classification of Errors

For actual comparison the DGG was used as the default grid, meaning that for each LST dataset all points belonging to a DGG point were searched and then the LSTs for all these points were averaged and compared to the SSF. This is mainly relevant for the 1km product from AATSR.

5.1.1 Basic error classification

The Surface State Flag is capable of differentiating between 4 states as seen in Chapter 4. For the validation efforts the temporary melting flag was treated as unfrozen and the permanent ice value as frozen because these states should occur in the same temperature range most of the time. The freeze/thaw states were compared to the different temperature datasets using a simple threshold at 0° according to Table 5.1.

The terms positive and negative, used in the error classification, have historical context and were originally used in medicine where a positive classification meant that a patient had a certain disease.

Error Analysis

There are two different kind of errors:

Type I error (false positive): Temperature data has a value above 0 °C but SSF shows frozen. Valid soil moisture measurements are disregarded

Type II error (false negative): Temperature data has a value below 0 °C but SSF shows unfrozen. Invalid soil moisture measurements are not identified

The overall accuracy is of course important but few Type II errors are a priority if the SSF is used for flagging soil moisture measurements.

ROC curves

The errors can also be described using the true positive rate (TPR) and the false positive rate(FPR). These are defined as

$$TPR = \frac{\text{True positives}}{\text{True positives} + \text{False negatives}} \tag{5.1}$$

$$FPR = \frac{\text{False positives}}{\text{False positives} + \text{True negatives}} \tag{5.2}$$

These parameters can then be inserted into a receiver operating characteristic (ROC) curve which shows the effectiveness of a detector [37]. A ROC curve provides a richer measure of classification performance than other scalar measures [8].

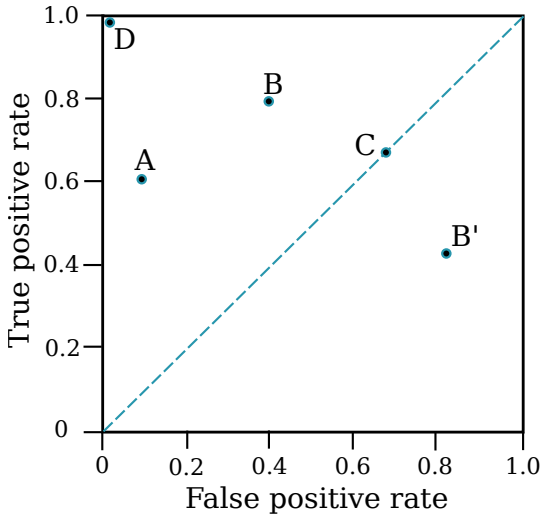

Figure 5.1 – ROC space with discrete clasifiers (after [8])

Fig.5.1 shows the ROC space where TPR is plotted on the Y axis and FPR on the X axis. The diagonal line is called the line of no discrimination, a point (C) falling on this line is essentially a random guess. All points above this line do better than a random guess and all below do worse. The better a point the more it will be in the upper left corner. The more left a point (classifier A) is the more conservative its classification algorithm, because it only makes a decision with strong evidence and therefore very few false positive errors. A point on the right side of the ROC space may classify the same number of observations correctly than one on the left side but it will do so with weak evidence and therefore make more Type I errors. The area below the diagonal line is usually empty since the decision process of any classifier that would fall in there can easily be inverted in order to make it switch sides (see B and B' in Fig.5.1). Classifier D makes no mistakes, representing the perfect case.

5.2 Global Temperature Datasets

Assessment of the validation quality of global datasets is rather complex since the climate on earth is extremely diverse and it is not expected that a single algorithm performs consistently on a global scale. The temperature models may not have the same accuracy everywhere on earth, which adds another layer of complexity.

First an overview of the validation results will be given, followed by a more in depth look into the behaviour in different times of the year. An intercomparison of the results will lead to areas where there are big differences between the temperature datasets, these cases will be investigated in the last part of the validation.

5.2.1 Overview

Figure 5.2 and Table 5.2 show that the overall classification results compared to the used global temperature datasets are rather good and very similar. They all show similar spatial patterns, with high agreement with the SSF in Siberia, central Europe, the northern United States and Canada. Lower agreement is generally found in southern areas where freezing does not occur regularly but also in Scandinavia and in regions where backscatter does not change with temperature. There are also other reasons that lead to a failure of the algorithm which will be discussed in chapter 5.2.6.

The agreement with the WMO meteo dataset is lower than that with the global climate models, this is due to the uneven distribution of the in situ stations, with few stations in areas where freezing is common and the algorithm seems to work well. The different distribution of measurements can also be seen in Table 5.2 where only 24,47% of WMO meteo datapoints show temperatures below 0°C compared to an average of 43,05% for the 3 other datasets. Between 63 and 76 % of measurements that where not in agreement with the SSF are false positives, meaning a measurement was flagged as frozen but the respective temperature dataset indicated otherwise, which is important for SWI generation as catching all freezing events has priority over flagging too many measurements as frozen. The algorithm fails to identify a freeze/thaw state for 3,38 or 4,68% of measurements, the reason for these invalid SSF and their distribution will be examined closely in chapter 5.2.5. A more in depth look into the validation results of each dataset will be given in the following chapters.

	ERA air temp.		ERA soil temp.		GLDAS soil temp.		WMO meteo	
	Frozen	Unfrozen	Frozen	Unfrozen	Frozen	Unfrozen	Frozen	Unfrozen
< 0°C	38,50	3,35	38,56	4,91	39,92	5,09	21,36	3,11
> 0°C	8,68	46,10	8,62	44,54	7,25	44,35	10,29	60,56
Invalid	3,38		3,38		3,38		4,68	
Correct	**84,60**		**83,09**		**84,27**		**81,93**	

Table 5.2 – Agreement of various datasets with the SSF for the years 2007 and 2008

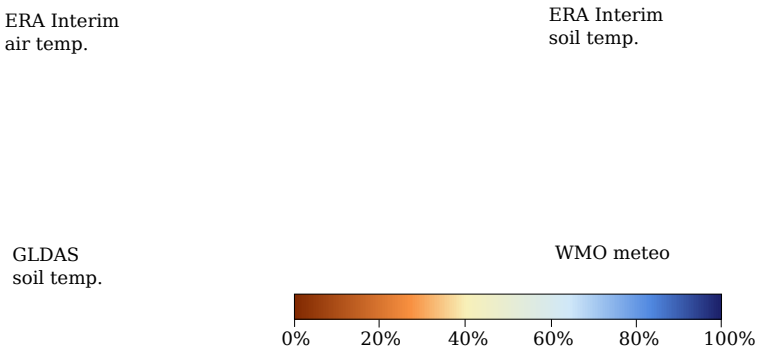

Figure 5.2 – Agreement of various datasets with SSF in percent for the years 2007 and 2008.

5.2.2 ERA Interim

Both comparisons with soil and 2m air temperature show least agreement with the SSF in the transitional times of the year when temperatures are around 0°C. In these times of the year the temperature dataset is most likely to not represent the actual freeze/thaw state of the soil. The comparison with air temperature yields better results than the validation with soil temperature. An obvious reason for this behaviour could be that the algorithm was trained with ERA Interim air temperature, but making this argument is not straightforward since agreement with GLDAS soil temperature (see chapter 5.2.3) is similar to that with ERA Interim air temperature. Comparing the transition periods (TZ1 and TZ2) in Fig.5.3 and 5.4 it can be seen that Siberia, Canada and parts of southern China have better agreement with air temperature.

Examining the different error types can give a hint of where the dissimilarities come from. In transition zone 1 or spring more temperature measurements are below 0°C for soil temperature then there are for air temperature. This can be expected since soil does not thaw immediately when air temperature rises above the thawing point of ice. In TZ2 or autumn the opposite relationship can be seen as soil temperature drops below 0°C later than air temperature, the shift is not as big as in spring where more than 10% of soil temperature measurements are on a different side of zero degrees celsius than air temperature observations.

Winter and Summer compare similarly with the SSF for both air and soil temperature. In Summer very few measurements show values below 0°C, the only problem are the 6,27% of measurements for which no SSF can be calculated, this will be investigated in chapter 5.2.5. In Winter the validation results in parts of southern China show big differences between air and soil temperature.

	Winter		TZ1		Summer		TZ2	
	Frozen	Unfrozen	Frozen	Unfrozen	Frozen	Unfrozen	Frozen	Unfrozen
< 0°C	81,96	2,22	17,01	9,69	0,16	1,09	29,68	3,93
> 0°C	8,02	6,34	15,97	54,04	0,50	91,97	17,83	45,92
Invalid	1,46		3,28		6,27		2,63	
Correct	**88,30**		**71,05**		**92,14**		**75,61**	

Table 5.3 – Agreement between ERA Interim 2m air temperature and SSF in percent

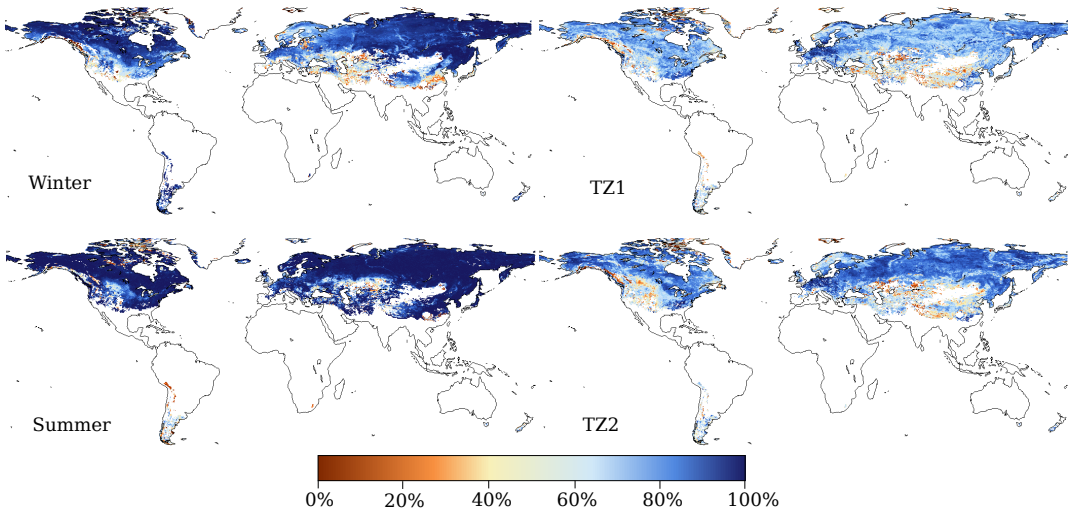

Figure 5.3 – Global maps of agreement of ERA Interim 2m air temperature with SSF in percent for the years 2007 and 2008.

	Winter		TZ1		Summer		TZ2	
	Frozen	Unfrozen	Frozen	Unfrozen	Frozen	Unfrozen	Frozen	Unfrozen
< 0°C	82,32	2,52	20,62	16,57	0,10	1,71	25,95	5,00
> 0°C	7,66	6,04	12,36	47,17	0,56	91,35	21,57	44,86
Invalid	1,46		3,28		6,27		2,63	
Correct	**88,36**		**67,79**		**91,45**		**70,81**	

Table 5.4 – Agreement between ERA Interim soil temperature and SSF in percent

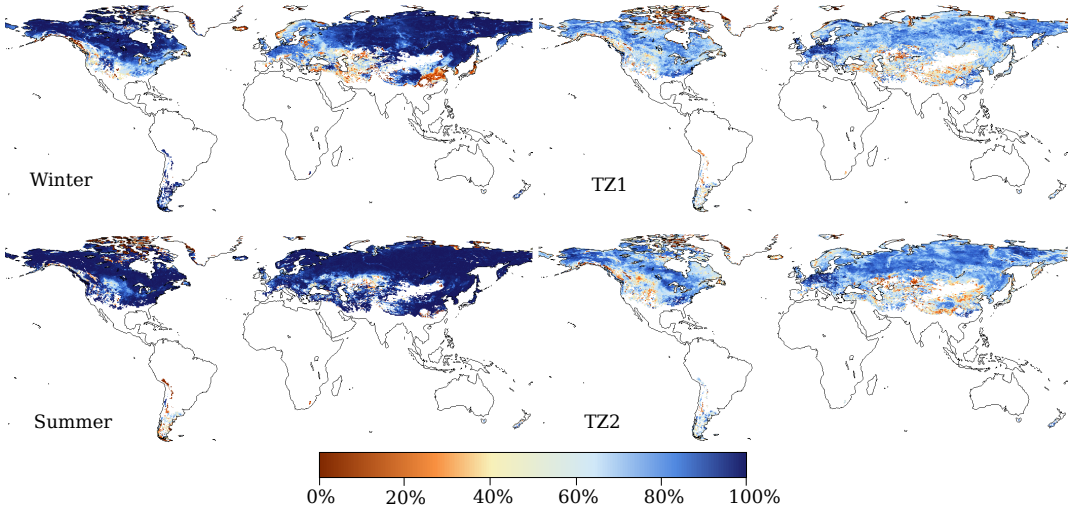

Figure 5.4 – Global maps of agreement of ERA Interim soil temperature with SSF in percent for the years 2007 and 2008.

5.2.3 GLDAS

Interestingly the agreement of the SSF with GLDAS soil temperature is about as good as that with ERA Interim air temperature in TZ2, better than with both ERA datasets in Winter and between them in TZ1 and Summer. The distribution of measurements between negative and positive temperature is similar to ERA Interim soil temperature except for TZ2 where GLDAS has more data points below 0°C than both ERA Interim datasets. The aggregated percentages do not show a lot of detail, so it is better to look a the difference plots in Fig. 5.6.

	Winter		TZ1		Summer		TZ2	
	Frozen	Unfrozen	Frozen	Unfrozen	Frozen	Unfrozen	Frozen	Unfrozen
< 0°C	83,85	2,88	20,99	16,01	0,15	1,66	30,21	5,91
> 0°C	6,13	5,68	11,99	47,73	0,51	91,41	17,31	43,94
Invalid	1,46		3,28		6,27		2,62	
Correct	**89,52**		**68,72**		**91,56**		**74,16**	

Table 5.5 – Agreement between GLDAS soil temperature and SSF in percent

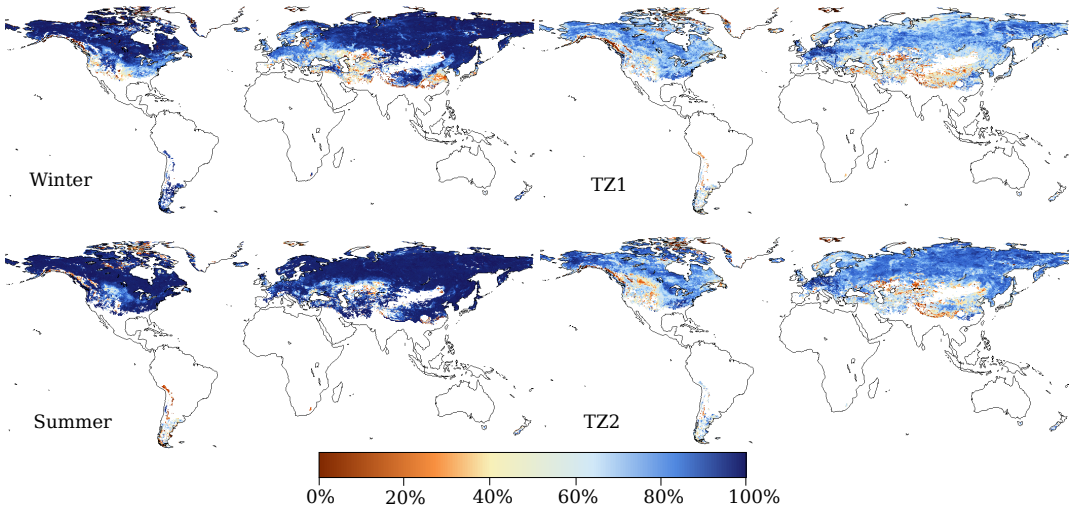

Figure 5.5 – Global maps of agreement of GLDAS soil temperature with SSF in percent for the years 2007 and 2008.

Difference to ERA Interim

The validation results achieved when comparing the SSF to GLDAS soil temperature are compared to those calculated with ERA Interim soil temperature.

In Winter most of Siberia and Canada only show small differences in the agreement to the SSF, but Scandinavia, south eastern China, Iran, Turkey and parts of southern Canada show significantly better results for GLDAS soil temperature. GLDAS performs worse in the Himalayas and a few small areas in eastern Europe.

In spring or transition zone 1 there is no obvious pattern or regions that perform better or worse in either dataset. In central Canada there is better agreement between GLDAS soil temperature and SSF than with ERA Interim soil temperature. What's interesting is that the regions which performed much better in Winter now perform worse or equal to ERA Interim soil temperature, so this is not a consistent effect which is observable the whole year.

Summer is not pictured because there are no remarkable differences between the two validation results.

In autumn or transition zone 2 large parts of Siberia, China and especially Quebec and Newfoundland and Labrador GLDAS soil temperature matchs better with the SSF than ERA Interim soil temperature whereas central Canada and most of Europe match worse.

For 2 years of data north western Scandinavia and eastern China show large improvements over the validation with ERA Interim soil temperature as well as Iceland, Japan and the southern part of Kamchatka Krai in eastern Siberia. There are no regions where GLDAS soil temperature performs significantly worse than the equivalent dataset from ERA Interim. Regions, where the difference in agreement is apparent and more than 5% for a full year, will be further examined.

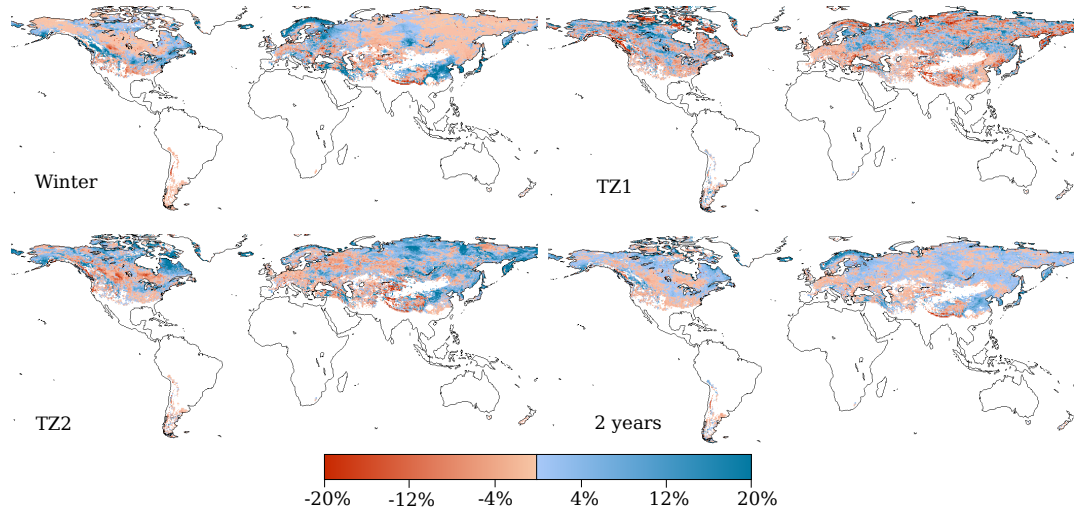

Figure 5.6 – Difference between classification accuracy of GLDAS and ERA Interim soil temperature (GLDAS-ERA Interim) for Winter the 2 transition periods and the complete 2 year dataset

Scandinavia In Scandinavia differences in agreement between SSF and the temperature datasets are especially pronounced in the winter period. In Fig.5.7 we can see that the GLDAS soil temperature stays below 0 degrees Celsius the whole winter while both ERA Interim datasets reach above 0°C multiple times during winter. In spring the thawing indicated by the SSF fits very good with the Snow Water Equivalent from GLDAS while ERA Interim shows complete snowmelt sooner than both GLDAS and SSF. The ERA Interim temperatures rise about 6 weeks before GLDAS soil temperature begins to rise. The models obviously model soil temperature differently, with ERA Interim showing more temperature differences when the soil is frozen. When melting of snow occurs GLDAS still shows a soil temperature of below 0°C while ERA Interim temperatures are way above this threshold. This explains why the validation results in spring are worse for GLDAS soil temperature in this region.

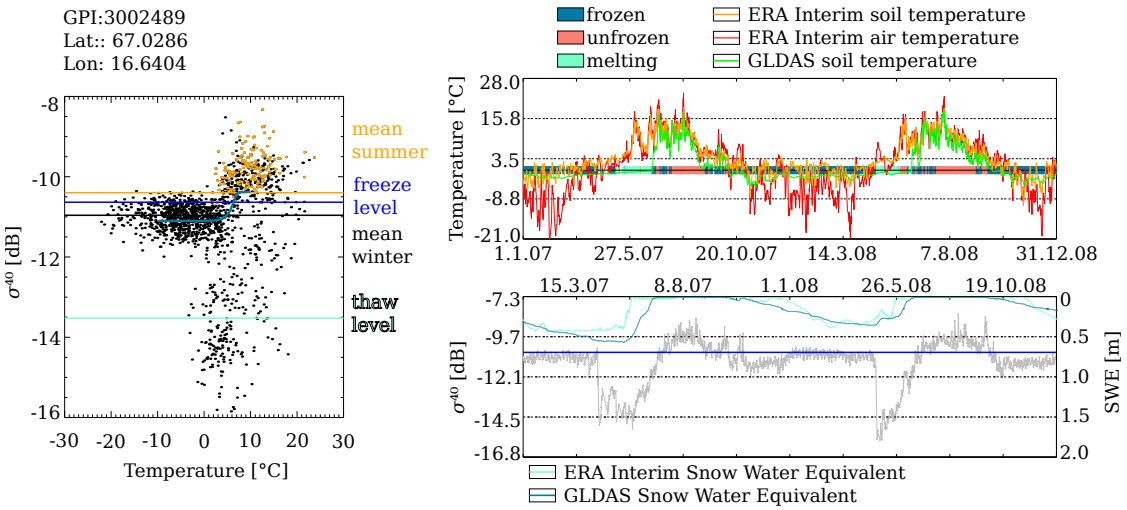

Figure 5.7 – On the left: σ_{40}/temperature plot,fitted logistic function in dark blue with backscatter measurements taken in summer shown in orange. On the right: Temperature plot with SSFs indicated around the 0°C line and σ_{40} plot with freeze level(horizontal blue line) for a grid point in Scandinavia

What we can also observe is that the SSF shows frozen conditions after the melting period in both years, these flags are probably wrong since all temperature datasets have values well above the thawing point of ice and also σ^{40} is around or slightly above the freeze threshold. Other than that the SSF algorithm works very well considering that the σ^{40}/temperature distribution in Fig.5.7 is not without ambiguities, especially around zero degrees Celsius.

South Korea The reason for the bad agreement of the SSF with ERA Interim soil temperature in parts of South Korea is that the temperature dataset shows too high values in winter. It never reaches less than about 9°C at the gridpoint in Fig.5.8. It's not certain that the ground freezes when air temperature is below 0°C but the drop in σ^{40} backscatter indicates it and the GLDAS soil temperature dataset agrees.

The σ^{40}/temperature plot in Fig.5.8 shows that a logistic function is a very good fit for the temperature dependance of backscatter with only a few measurements taken in positive temperatures below the freeze level. But we can also see that these observations lead to the SSF indicating short freezing periods at the end of October 2007 and 2008 that are not consistent with the temperature measurements. Especially in 2008 the temperature remains well above 10°C. Nonetheless it is safe to conclude that in this case the algorithm works well and the ERA Interim soil temperature dataset is to blame for bad validation results.

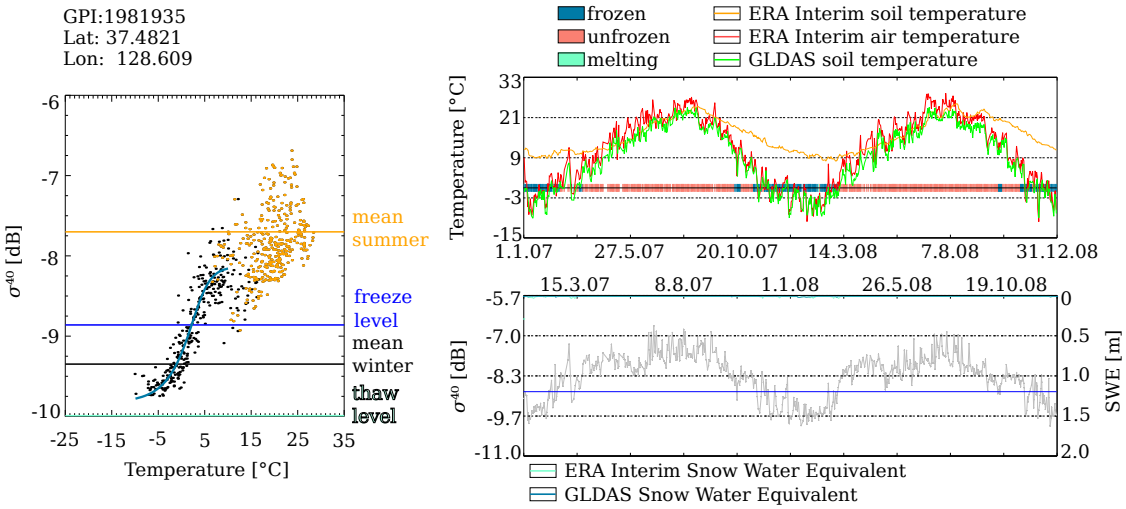

Figure 5.8 – On the left: σ_{40}/temperature plot,fitted logistic function in dark blue with backscatter measurements taken in summer shown in orange. On the right: Temperature plot with SSFs indicated around the 0°C line and σ_{40} plot with freeze level(horizontal blue line) for a grid point in South Korea

Iceland In this area ERA Interim soil temperature behaves strangely in winter as it first goes below, but then rises and hovers slightly above, 0°C (see Fig.5.9). The backscatter timeseries looks a little erratic in its changes, but we can see on the σ^{40}/temperature plot that the backscatter dependency on temperature is obvious but not as clear cut than for example in Fig.5.8, because of that the SSF may indicate frozen soil a little too long in spring when backscatter is near the freeze level. It is interesting that the SSF shows several short thawing periods in winter that are accompanied by quick rising temperatures that are not above the thawing point of ice, and dropping backscatter, which could mean that there is water on the surface while the ground remains frozen.

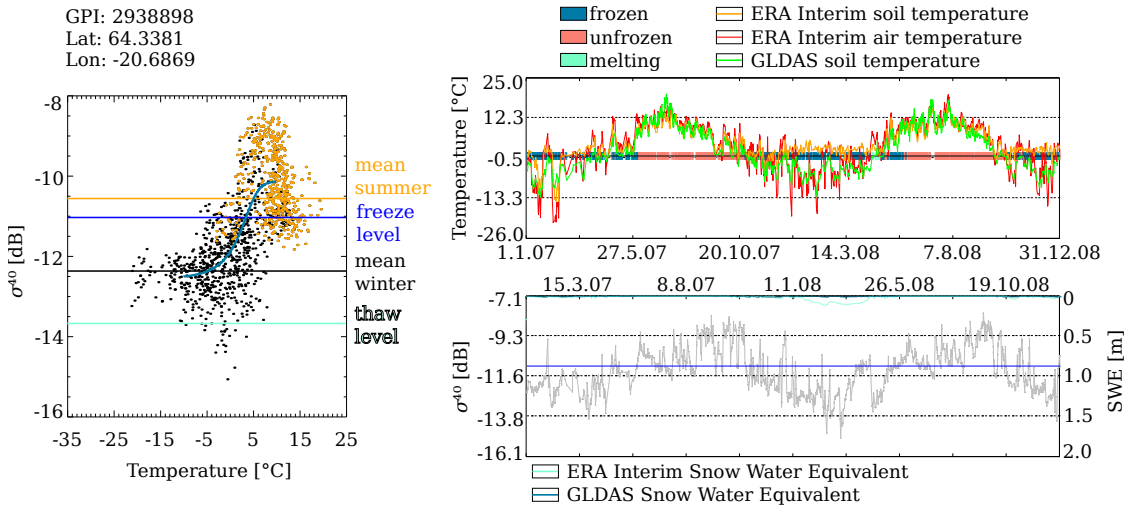

Figure 5.9 – On the left: σ_{40}/temperature plot,fitted logistic function in dark blue with backscatter measurements taken in summer shown in orange. On the right: Temperature plot with SSFs indicated around the o°C line and σ_{40} plot with freeze level(horizontal blue line) for a grid point in Iceland

China The chosen grid point in eastern China (Fig.5.10) shows the already familiar problem of ERA Interim soil temperature in certain areas as it only goes below the freezing point of water for a very short period in winter while the other temperature datasets and the drop in backscatter indicate frozen soil. But this gridpoint also shows a problem of the SSF algorithm when the change in backscatter, due to freezing is well represented by the fitted logistic function, but has no easily described behaviour during hotter time periods of the year (see σ^{40}/temperature plot in Fig.5.10). In this case this problem leads to frozen SSFs when temperatures are way above the thawing point of ice and the backscatter has risen about 1dB from its lowest levels, which occur around the beginning of January in both 2007 and 2008. This is due to very low soil moisture.

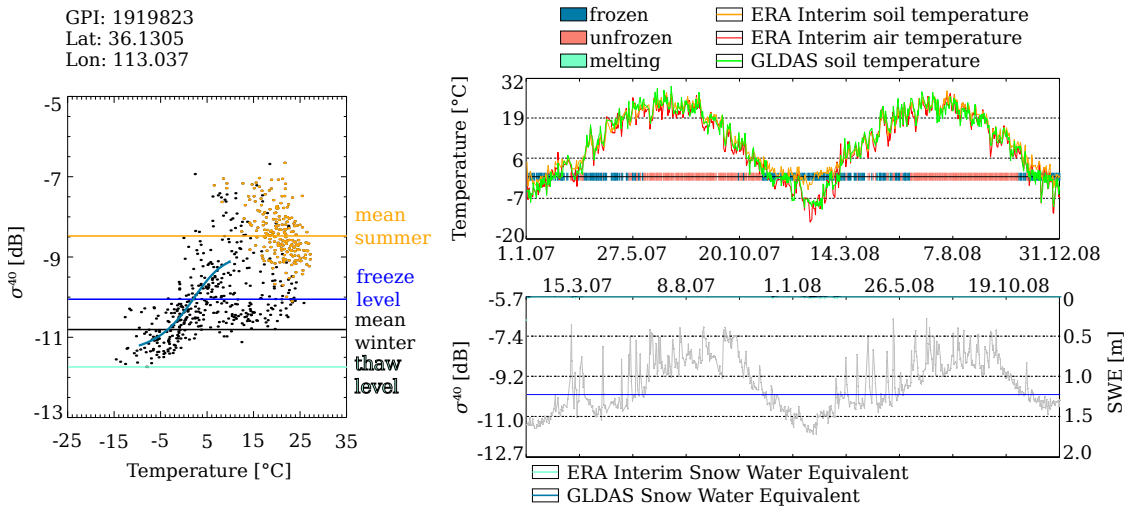

Figure 5.10 – On the left: σ_{40}/temperature plot,fitted logistic function in dark blue with backscatter measurements taken in summer shown in orange. On the right: Temperature plot with SSFs indicated around the o°C line and σ_{40} plot with freeze level(horizontal blue line) for a grid point in eastern China

Kamchatka Krai (Siberia) In this area of the world ERA Interim compares worse to the SSF than GLDAS soil temperature, especially in spring. It seems this has a similar reason than in Scandinavia as the ERA Interim dataset shows thawing earlier than GLDAS and the SSF(see Fig.5.11). In autumn the ERA Interim soil temperature also stays above the freezing point of water about a month longer than all other indicators for frozen soil. The σ^{40} timeseries shows that backscatter drops at the end of winter and GLDAS snow water equivalent begins to drop at the same time, but the SSF algorithm does not flag these observations as thawing most of the time because backscatter does not drop enough for the algorithm to recognize it. These measurements can also be seen in the lower right part of the σ^{40}/temperature plot in Fig.5.11. There they are separate but well above the recognized thaw level.

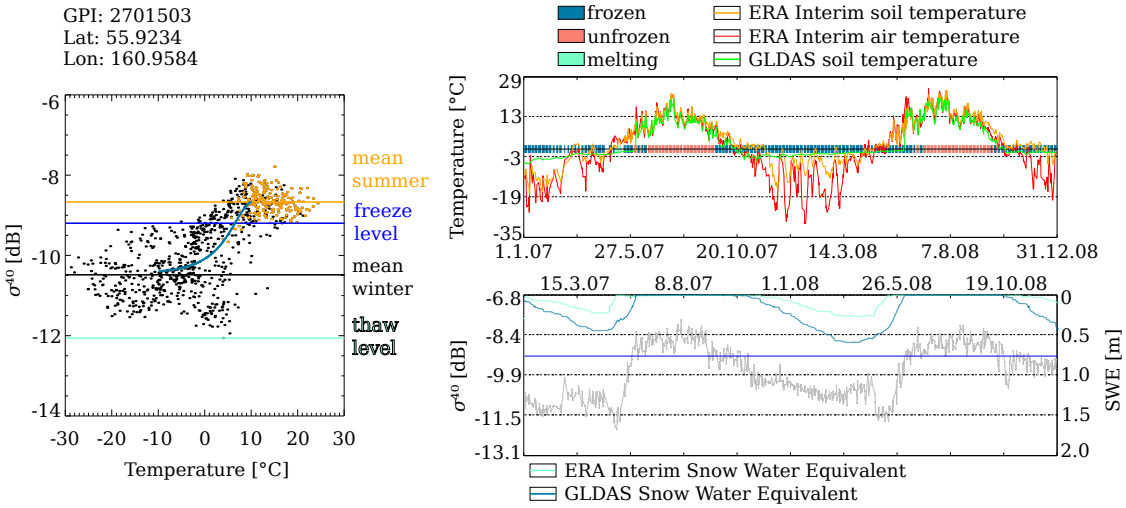

Figure 5.11 – On the left: σ_{40}/temperature plot,fitted logistic function in dark blue with backscatter measurements taken in summer shown in orange. On the right: Temperature plot with SSFs indicated around the 0°C line and σ_{40} plot with freeze level(horizontal blue line) for a grid point in Kamchatka Krai, East Siberia

Japan At this gridpoint in Japan ERA Interim temperature data does not indicate freezing but GLDAS soil temperature and snow water equivalent as well as backscatter do. The σ^{40}/temperature plot in Fig.5.12 shows the drop in backscatter very clearly and its also obivous in the σ^{40} timeseries but the values of the temperature datasets are only seldom below zero degrees, if ever. Only GLDAS soil temperature stays below the freezing point of water for an extended period of time in the beginning of 2008, but this seems to be because the GLDAS-NOAH model keeps soil temperatures below 0°C when snow is present. It is difficult to say if the frozen SSFs in the middle of March 08 are correct since temperatures are all above zero degrees celsius and backscatter is around the freeze level.

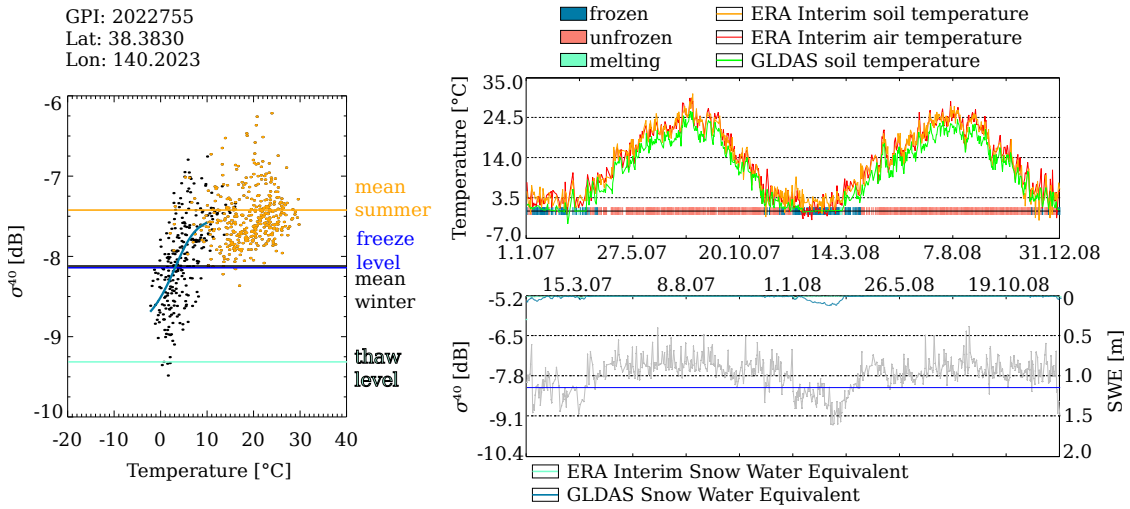

Figure 5.12 – On the left: σ_{40}/temperature plot,fitted logistic function in dark blue with backscatter measurements taken in summer shown in orange. On the right: Temperature plot with SSFs indicated around the o°C line and σ_{40} plot with freeze level(horizontal blue line) for a grid point in Japan

5.2.4 WMO Meteo

The validation results achieved with the WMO Meteo dataset do not reveal new information. They show similar spatial and temporal patterns as the validation with climate models, but this is to be expected since climate modellers incorporate this dataset into their models. Since the difference to the climate models is not big, this dataset can be used to quickly test changes in the algorithm, because the processing time for validation is significantly less then for either climate model. This fact will also be used in chapter 6 to test different improvements to the algorithm. As already mentioned in the overview, the smaller overall percentages in table 5.6 are due to the distribution of the measurement stations and not because of lesser agreement with the SSF of the individual observations.

	Winter		TZ1		Summer		TZ2	
	Frozen	Unfrozen	Frozen	Unfrozen	Frozen	Unfrozen	Frozen	Unfrozen
< o°C	54,46	3,11	16,10	9,06	0,03	0,74	21,26	3,34
> o°C	16,13	23,41	15,65	55,57	0,19	92,30	19,53	52,11
Invalid	2,89		4,00		6,75		4,00	
Correct	**77,87**		**71,67**		**92,32**		**73,41**	

Table 5.6 – Agreement between WMO interpolated temperature and SSF in percent

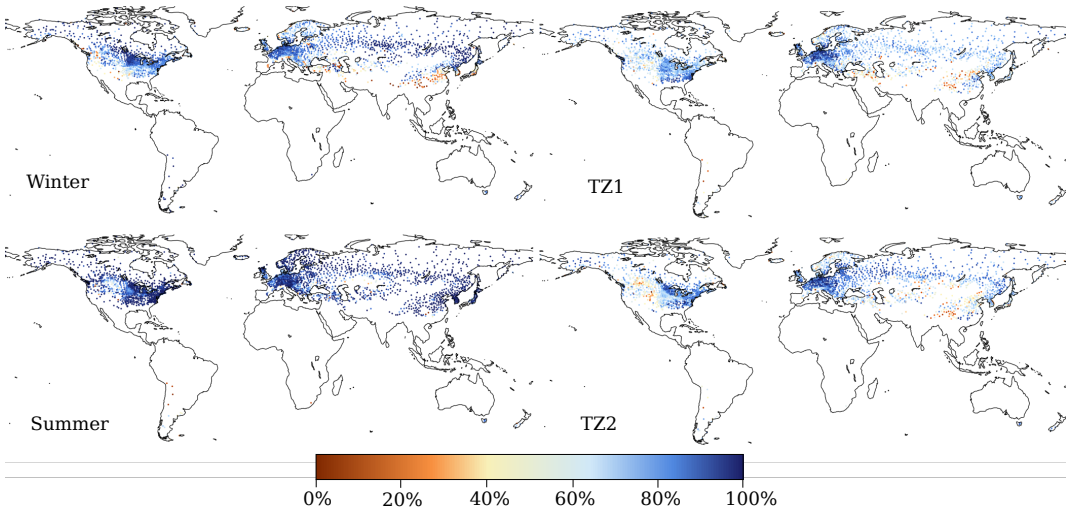

Figure 5.13 – Global maps of agreement of WMO interpolated temperature with SSF in percent for the years 2007 and 2008.

5.2.5 Unknown Surface State Flags

As we can see in Fig. most backscatter measurements to which no SSF can be attributed occur in the transition zones and in Summer. It is also clear when looking at the decision trees (Fig.4.8,4.9,4.10), that unknown SSFs mainly occur in Summer. They are also more likely to occur when decision tree 2 is used (Fig.4.7), which is logical since this decision tree was introduced in areas where backscatter is low in summer due to dry soil.

There is some similarity between the areas where no SSF can be found in Summer and the Köppen Climate classification of cold semi-arid climates (Fig.5.15). These areas commonly feature hot and dry summers and cold winters with some snowfall.

In Northern America the similarity of the problem areas in Summer (Fig.5.14) with what's called Palliser's Triangle (Fig.5.16),named after John Palliser, a british explorer who first remarked on this area for being unusable due to a lack of rainfall and timber [38], is very clear. This area, also known by the name Canadian Prairies, is very prone to frequent and severe droughts. These very dry conditions in summer leads to very low backscatter which in turn leads to unknown SSFs (see Fig.5.17)

In general unknown SSFs tend to be in areas where the overall classification accuracy is not very high, those are also the areas where there is little correlation or dependence between σ^{40} backscatter and temperature (see Fig.4.4).

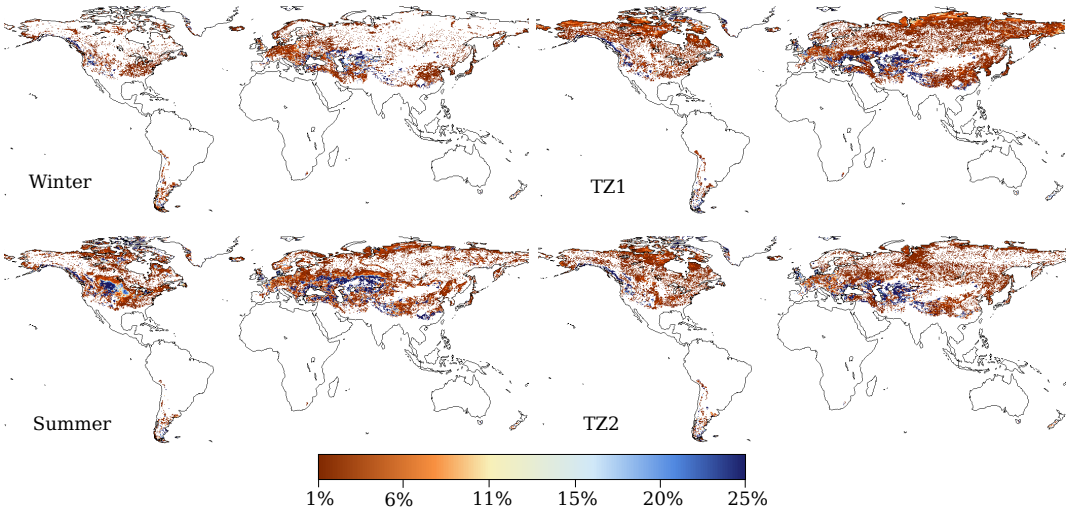

Figure 5.14 – Distribution of invalid SSF for 4 time periods, in percent.

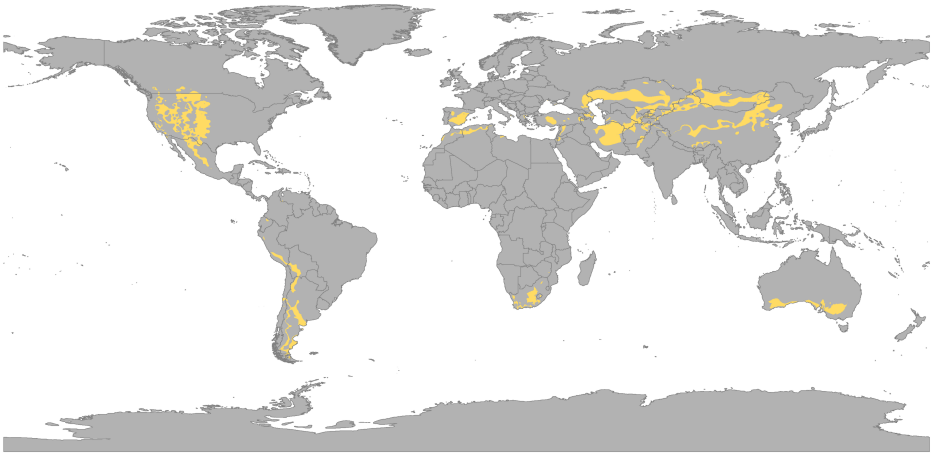

Figure 5.15 – Köppen climate classification of cold semi-arid areas (BSk). (taken from [9])

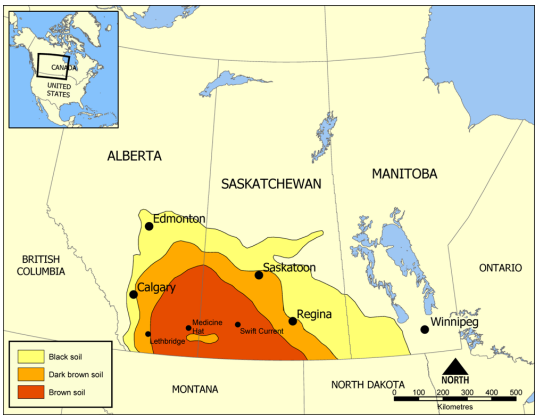

Figure 5.16 – Map of Palliser's Triangle in the Canadian Prairies(taken from [10])

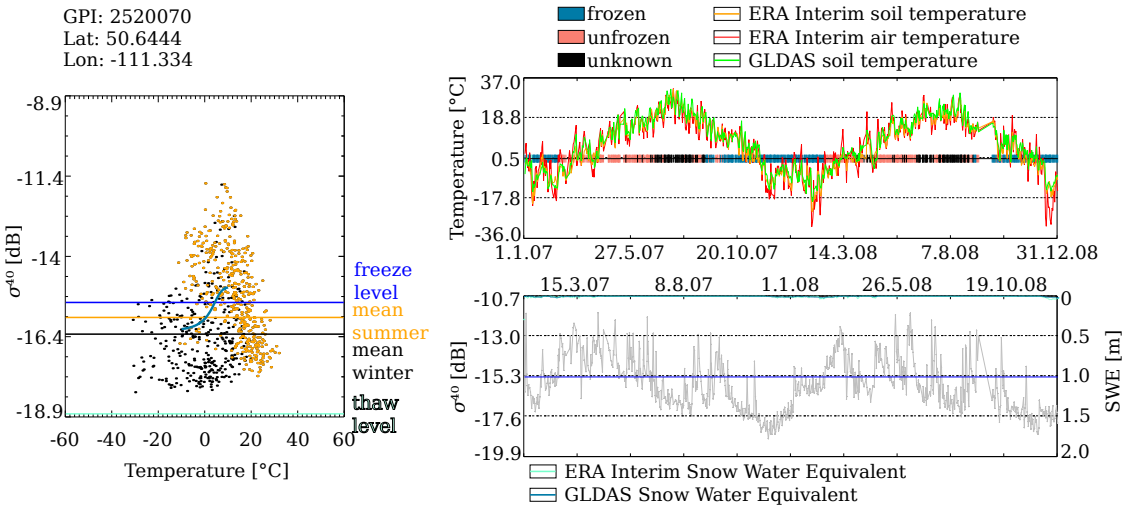

Figure 5.17 – On the left: σ_{40}/temperature plot,fitted logistic function in dark blue with backscatter measurements taken in summer shown in orange. On the right: Temperature plot with SSFs indicated around the o°C line and σ_{40} plot with freeze level(horizontal blue line) for a grid point in the Canadian prairies

5.2.6 Failure cases

There are two different definitions of a failure in this case. If no freeze/thaw parameters can be derived then the algorithm has failed. These cases are not described in detail here as this happens in areas where backscatter is not dependent on temperature and was already discussed in chapter 4. The other case of a failure is given if the algorithm works but produces wrong results. This can happen for various reasons which will be discussed with examples in this section.

High backscatter in winter The algorithm has a built in mechanism, to catch rising backscatter with dropping temperatures, in the deepsnow flag (4.2). There are unfortunately cases when the conditions for the deepsnow flag are not satisfied but backscatter is still relatively high in winter.

Fig. 5.18 and 5.19 illustrate different incarnations of this behaviour. The first figure shows a gridpoint in northern Siberia, here we can observe the rising backscatter with dropping temperatures in the σ^{40}/temperature plot, but it is not pronounced enough to trigger the deepsnow flag. Because of that the timeseries plots in Fig.5.18 show unfrozen SSFs in Winter.

The second figure shows two backscatter levels during cold temperatures, this behaviour would not be recognized by the algorithm under any circumstance. We can see that the SSFs are wrong or unknown for large parts of the 2 year validation period. The σ^{40}/temperature plot in Fig.5.19 and 5.18 also illustrate the problems that occur when the dependence of backscatter on temperature is not without ambiguities. This not only leads to obvious problems in differentiating between frozen and unfrozen conditions but it is worsened by the fact that the detection of the transition periods is increasingly difficult when backscatter in summer and winter are too similar.

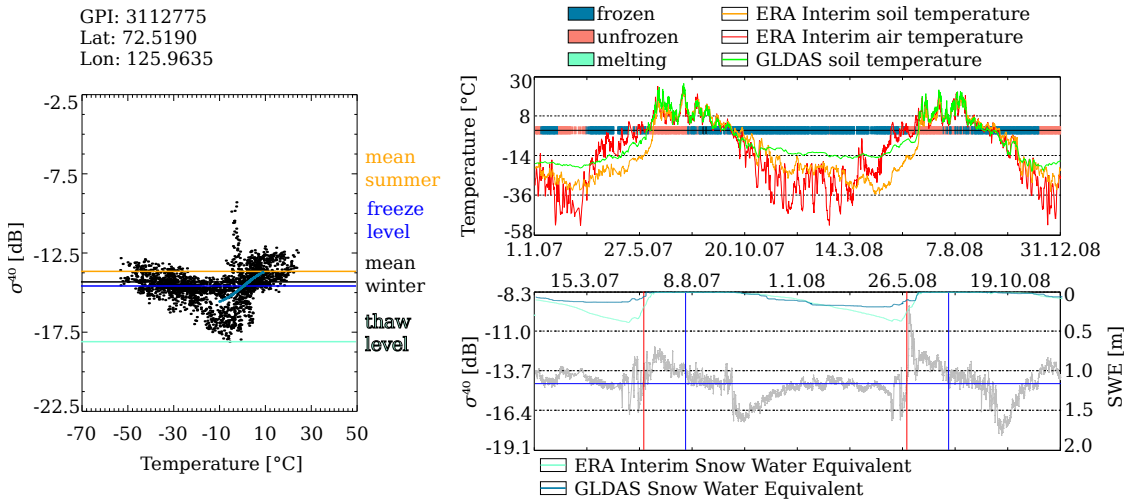

Figure 5.18 – On the left: σ_{40}/temperature plot, with the fitted logistic function in dark blue. On the right: Temperature plot with SSFs indicated around the 0°C line and σ_{40} plot with freeze level(horizontal blue line) and the transition times pt1 and pt2 (vertical red and blue lines respectively) for a grid point in north Siberia

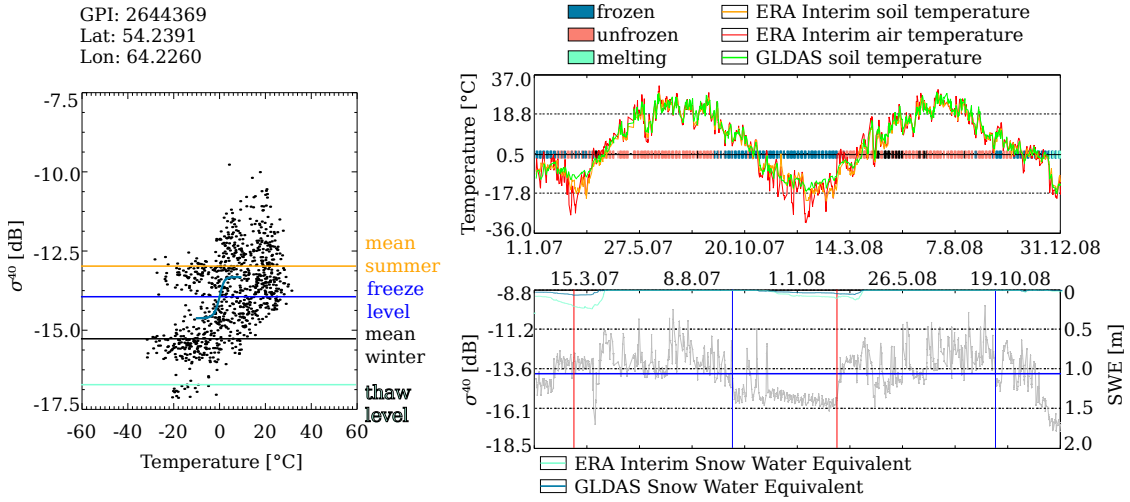

Figure 5.19 – On the left: σ_{40}/temperature plot, with the fitted logistic function in dark blue. On the right: Temperature plot with SSFs indicated around the 0°C line and σ_{40} plot with freeze level(horizontal blue line) and the transition times pt1 and pt2 (vertical red and blue lines respectively) for a grid point in Kazakhstan

False definition of the transition times There are two possibilities why the transition times are not correctly detected. The first is when backscatter in summer and winter are too similar then the step function approach does not yield realistic results. In Fig.5.19 the timeseries plots show that the second transition time pt2 (vertical blue line in the σ^{40} plot) is about 60 days too soon which increases the possibility of frozen flags since the algorithm thinks it is already autumn while in reality it is still summer.

Fig.5.18 also shows this problem as the second transition time pt2(vertical blue line in the σ^{40} plot) is indicated too early because the backscatter levels are so similar in winter and in summer. It is rather obvious that the transition period should start when backscatter drops sharply at the beginning of October. This leads to frozen SSFs when the backscatter is slightly above the freeze level in August.

The second possibility is a short freezing period as it is common in temperate regions. The step function approach assumes that winter and summer are both 3 months long (see chapter 4.1), if this is not the case wrong backscatter values will be assumed for the mean of winter and summer leading to wrong assignment of the transition times. In Fig.5.20 we can see that the summer period is very long compared to the winter period. This leads to a wrong assignment of the first transition time pt1 (the red vertical line in the σ^{40} plot). It is assigned approximately 2 months to late which increases the probability of frozen flags in this period. Freezing occurs seldom as can be seen in the σ^{40}/temperature plot.

This error also influences the algorithm in another way as it changes the thresholds used in decision tree 1 (see Fig.4.8).

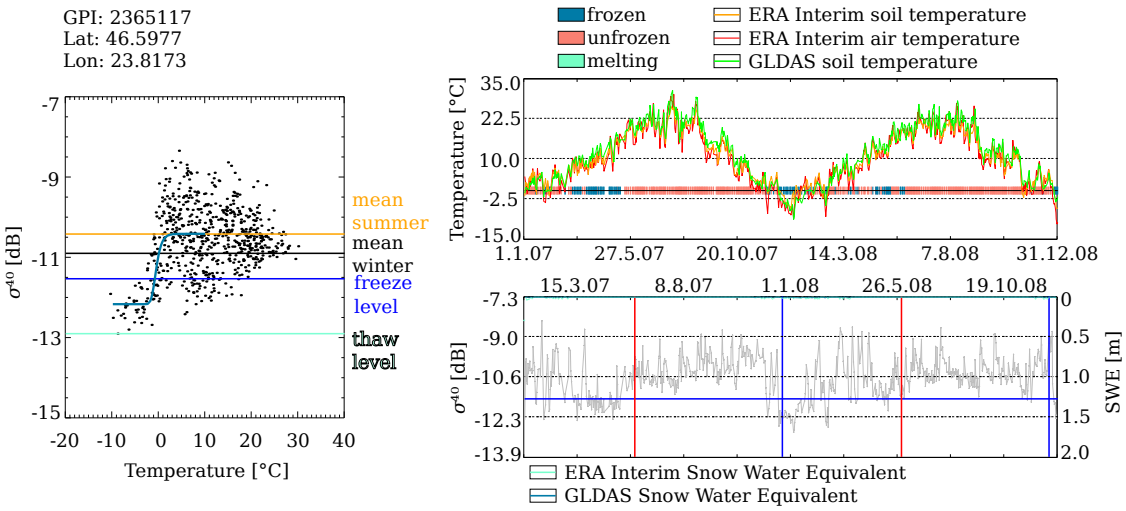

Figure 5.20 – On the left: σ_{40}/temperature plot, with the fitted logistic function in dark blue. On the right: Temperature plot with SSFs indicated around the 0°C line and σ_{40} plot with freeze level(horizontal blue line) and the transition times pt1 and pt2 (vertical red and blue lines respectively) for a grid point in Romania

Wrong fitting of the logistic function If there are not a lot of backscatter measurements, taken when temperatures are below zero degrees celsius then the logistic function can be fitted wrongly leading the algorithm to decide that permanent ice type behaviour of σ_{40} is observed at a grid point. In Fig.5.21 it is shown how one extraordinary event can cause this type of error.

China suffered under severe snow storms from the 25th of January until the 6th of February 2008 [39], interestingly a big anomaly in backscatter occurs at the same time. σ_{40} rises and falls about 3dB in the beginning of 2008, this short aberration is enough to change the fit of the logistic function in the σ^{40}/temperature plot, because there are very few other measurements below 0 °C. This type of error may be eradicated through better outlier detection or simply through taking longer time periods of ASCAT data into consideration when calculating the freeze/thaw parameters.

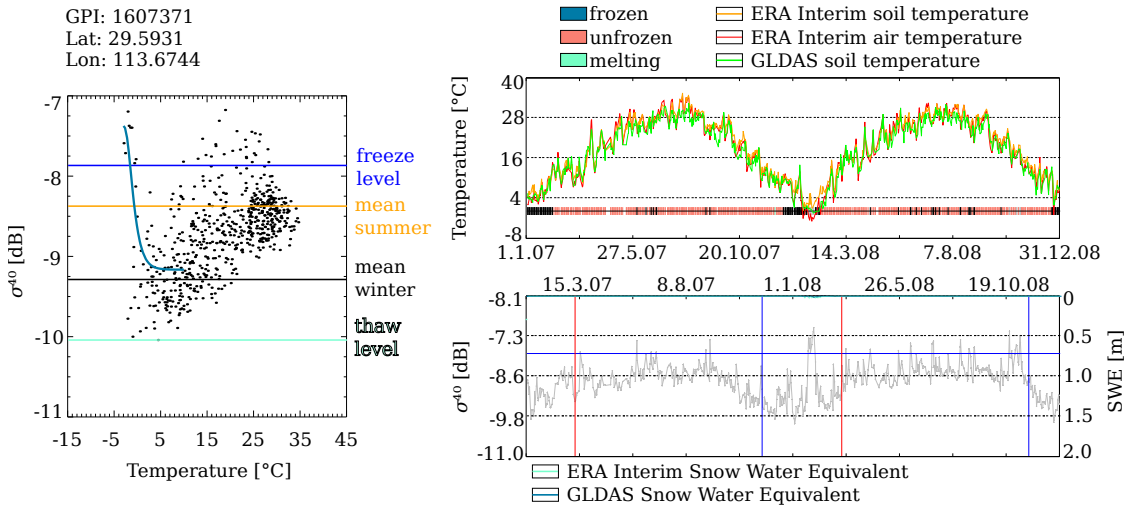

Figure 5.21 – On the left: σ_{40}/temperature plot, with the fitted logistic function in dark blue. On the right: Temperature plot with SSFs indicated around the 0°C line and σ_{40} plot with freeze level(horizontal blue line) and the transition times pt1 and pt2 (vertical red and blue lines respectively) for a grid point in China

5.3 GTN-P

The SSF and the GTN-P stations agree very well. Table 5.7 shows that the agreement is well above 80% for most stations. For most stations the agreement gets slightly worse the deeper a temperature was measured, this is somewhat expected since the microwaves emitted by ASCAT only penetrate the first few centimeters of the surface. In the following sections the stations will be analyzed in detail.

Station	Temperature	Agreement with SSF [%]
Nadym R1	surface	91.79
Nadym R1	air	90.36
R3 Marre Sale	0.02m below ground	82.75
R3 Marre Sale	0.5m below ground	80.13
R33 Borehole 3	0m surface	80.36
R33 Borehole 3	0.5m below ground	71.90
Barrow	0.04m below ground	84.16
Barrow	0.1m below ground	83.14
Council Forest	air	94.41
Council Forest	0.01m surface	79.87

Table 5.7 – Agreement of GTN-P stations with SSF

5.3.1 Nadym R1

In Fig.5.22 the air temperature data is in good agreement with the surface state flag, starting in September 07 the temperature hovers around the freezing point of water and the SSF generally shows frozen during negative temperatures and unfrozen when there they are positive, backscatter shows a similar behaviour to temperature during that time. Around November 5^{th} a sharp drop in temperature and σ_{40} signals freezup which is reflected in the SSF. The algorithm recognizes two thawing events in the beginning of May but does not indicate thawing at the end of March when temperatures are also rising above 0°C for a few days. Backscatter rises during this period which may indicate that the snowcover got wetter when the temperatures were positive but no open water appeared on the surface. Overall agreement between the in situ data and the nearest grid point, at a distance of 4.24 km, is 90.36%. Agreement with the surface temperature is slightly better but the dataset stays constant for some time which may indicates erroneous data.

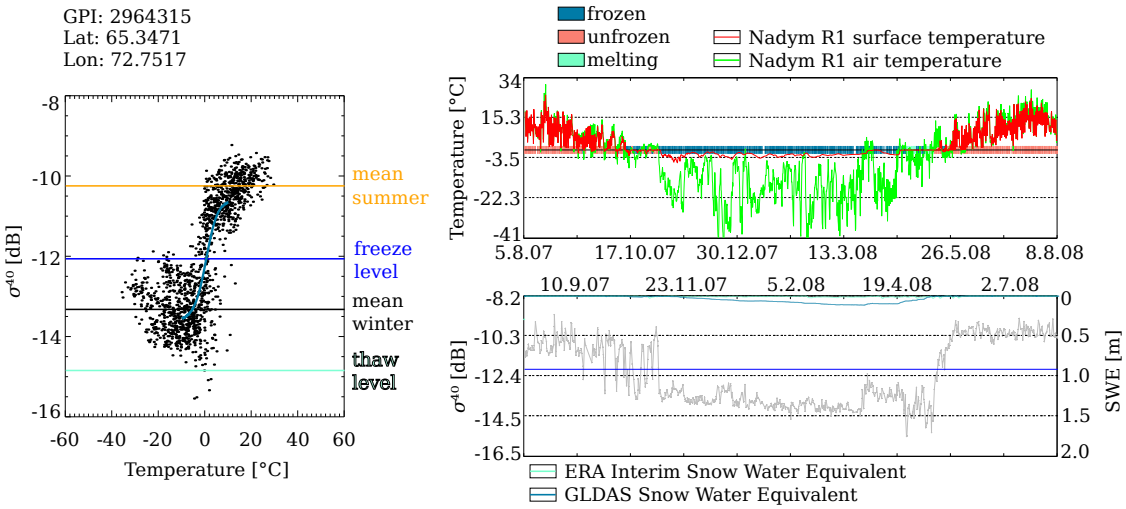

Figure 5.22 – On the left: σ_{40}/temperature plot, with the fitted logistic function in dark blue. On the right: Temperature plot with SSFs indicated around the 0°C line and σ_{40} plot with freeze level(horizontal blue line) for the station Nadym R1

5.3.2 Mare Sale R3

At the station R3-Marre Sale (Fig.5.23) the surface state is flagged as unknown(data gaps) for 7.53% of the measurements.The temperature was measured at a depth of 2 and 50cm. The algorithm recognizes freezup at the end of October quite well but shows unfrozen in November, December and even January and thawing in March and April when the borehole temperature data shows negative temperatures.

Air temperature data from the nearest WMO Meteo station shows that thawing can occur in March and April and is most likely caused by so called rain on snow events which do occur in this region [40] and are not as clearly visible in the surface temperature data from the borehole. Backscatter shows sharp drops in April and March, which also points toward rain on snow events. Fig.5.23 shows that the σ_{40}/temperature relationship is not very clear, this leads to a wrong calculation of the transition times especially pt2 (vertical red line in Fig.5.23) is assumed too soon. Because of that, the sharp drops in backscatter observed in the end of May and in June are not classified as thawing events, what they most likely are, but are flagged as unknown since, according to the algorithm, they occur in summer.

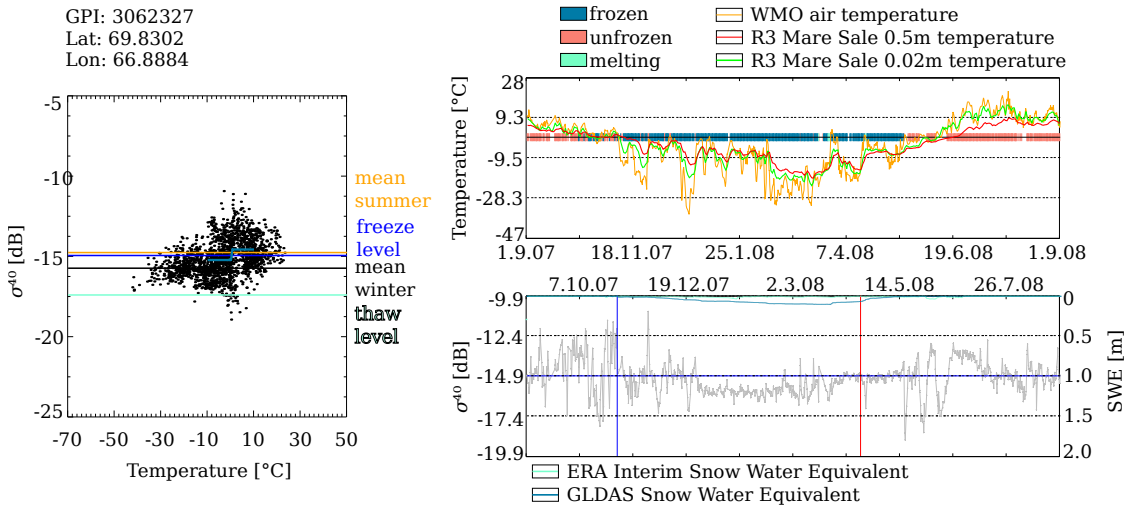

Figure 5.23 – On the left: σ_{40}/temperature plot, with the fitted logistic function in dark blue. On the right: Temperature plot with SSFs indicated around the 0°C line and σ_{40} plot with freeze level(horizontal blue line) for the station Mare Sale R3

5.3.3 R33 borehole 3

For station R33 borehole 3 only 6 months of data were available covering only one thawing period (Fig.5.24). The temperature was measured at the surface (0cm) and in 0.5m depth. For this grid point, the algorithm is likely flagging unfrozen conditions too soon (middle of April, beginning of May) and has problems in deciding between unfrozen and frozen surface states between the thawing events. The backscatter/temperature relationship is very good described by the logistic function but the rise in backscatter in spring is flagged as unfrozen, which is a little strange since it is below the freeze level for this grid point.

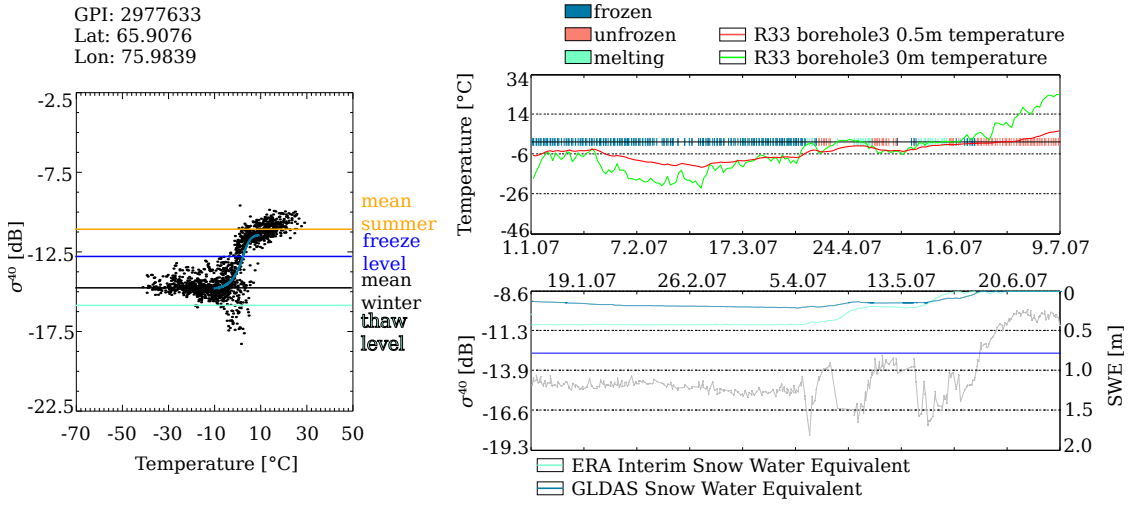

Figure 5.24 – On the left: σ_{40}/temperature plot, with the fitted logistic function in dark blue. On the right: Temperature plot with SSFs indicated around the 0°C line and σ_{40} plot with freeze level(horizontal blue line) for the station R33

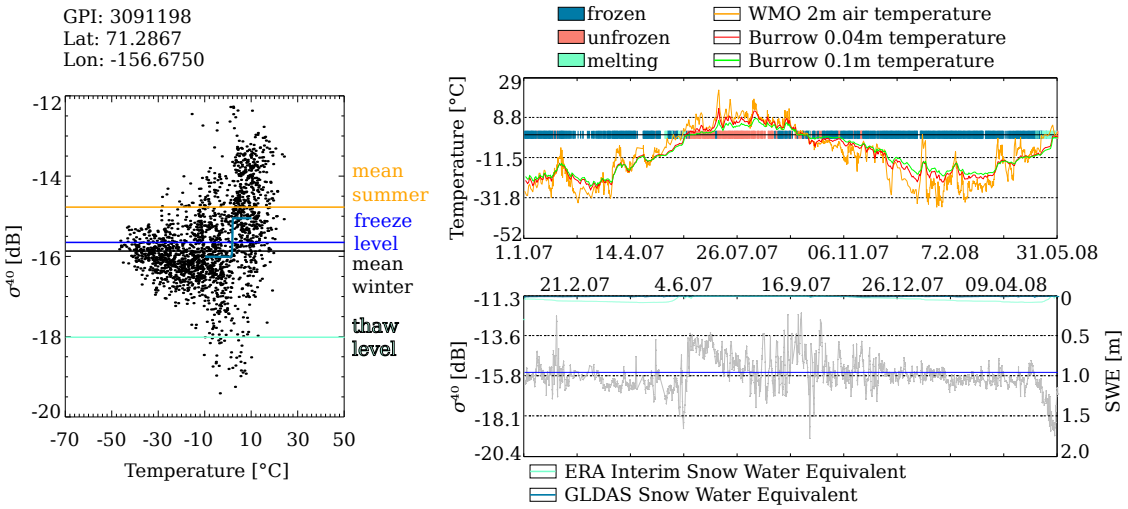

Figure 5.25 – On the left: σ_{40}/temperature plot, with the fitted logistic function in dark blue. On the right: Temperature plot with SSFs indicated around the 0°C line and σ_{40} plot with freeze level(horizontal blue line) for the station Barrow

5.3.4 Barrow

This station lies at the north coast of Alaska, the overall agreement is around 84% for both, the temperature measured at 0.04m and the one observed at 0.1m below the surface. The thawing events in May 2007 are detected but are interrupted by frozen periods. The backscatter does not show a very differentiated behaviour between summer and winter (see Fig.5.25), because of that the SSF shows frozen conditions at the beginning of September 2007 while the temperature datasets are still above 0°C. In October and November some measurements are flagged as unfrozen. The σ_{40} measurements vary by about ± 1.5dB in this period, in contrast to the winter periods when backscatter is more constant, which indicates some dependency on temperature. In May 2008 backscatter drops very fast and WMO air temperature rises abruptly. This may indicate a sudden and strong thawing event which is also detected by the SSF algorithm.

5.3.5 Council Forest

Fig.5.26 shows that the air temperature measured at the in situ station Council Forest in southern Alaska and the SSF agree very well. The 0.01m temperature doesn't fit so good, mainly because of temperatures above 0°C in Winter. The freeze/thaw timing is very well captured by the SSF, but there are a few small errors. In September 07 the SSF shows frozen conditions for a 2 short periods when temperatures are well above the freezing point of water and backscatter does not drop below the freeze level. After the freezeup in the beginning of August the temperature data as well as the backscatter show 2 spikes that could indicate short thawing of the surface. In January and February 2008 backscatter rises above the freeze level while temperatures also rise to slightly below 0°C but the SSF shows unfrozen only for a few measurements (barely visible in Fig.5.26). The thawing in April 2008 is well captured. Unfortunately there is a data gap during the freezing period in September 2008 which may influence the derivation of the freeze/thaw parameters, but agreement is still very good for the air temperature with 94.41%.

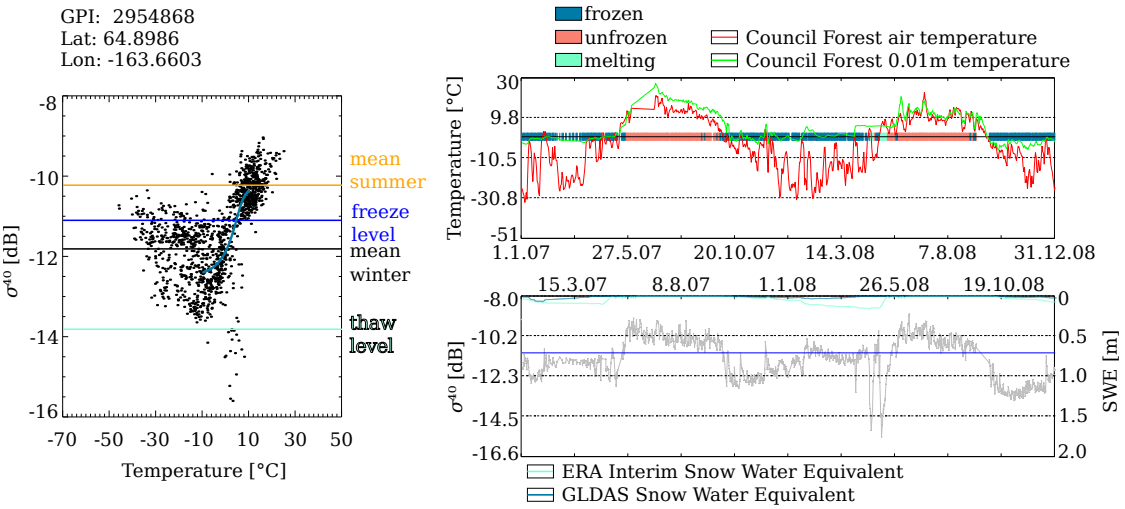

Figure 5.26 – On the left: σ_{40}/temperature plot, with the fitted logistic function in dark blue. On the right: Temperature plot with SSFs indicated around the 0°C line and σ_{40} plot with freeze level(horizontal blue line) for the station Council Forest

5.4 Satellite derived LST

Since the accuracy of Satellite derived LST products is between 1 and 3°K [32, 34] a "buffer" zone of ± 2°C was introduced where the comparison results between SSF and LST were not flagged as right or wrong, but as "around zero".

5.4.1 MODIS

Ob estuary

In winter and summer the SSF is nearly 100% in agreement with the LST data, the problematic times are in spring and autumn(Fig.5.27). In spring the SSF flag indicates unfrozen soil too soon. Most of the incorrect values are because the SSF indicates temporary water surface/melting conditions (see Fig.5.28). If the 8 day composite LST has a value below -2°C and the SSF flag shows temporary water surface/melting conditions then this is not necessarily contradictory, if it happens in a thawing period.

In autumn only very few measurements are classified as incorrect until 8 day period 38 where the SSF shows unfrozen in 40% of the test area without any rise in LST (see Fig.5.29).

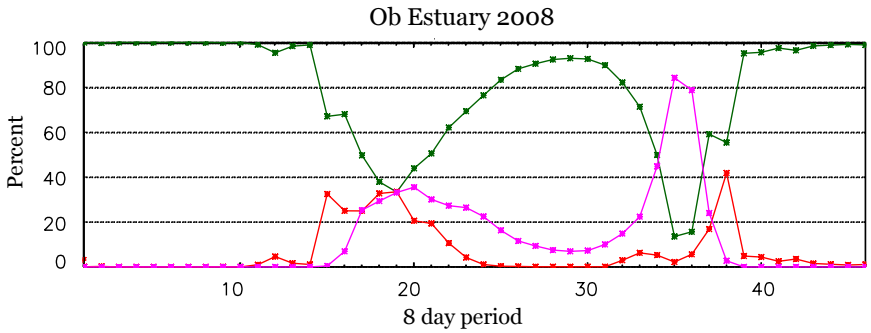

Figure 5.27 – Percent of correct (green), incorrect (red) and around zero (magenta) data points for every 8 day period.

North Siberia

In this test area we can see a similar behavior to the Ob Estuary region. The SSF flag indicated unfrozen and especially temporary melting conditions too soon but there is none the less a good agreement between the SSF and the LST (see Fig. 5.32 and Fig.5.33). There are no significant changes between 2007 and 2008.

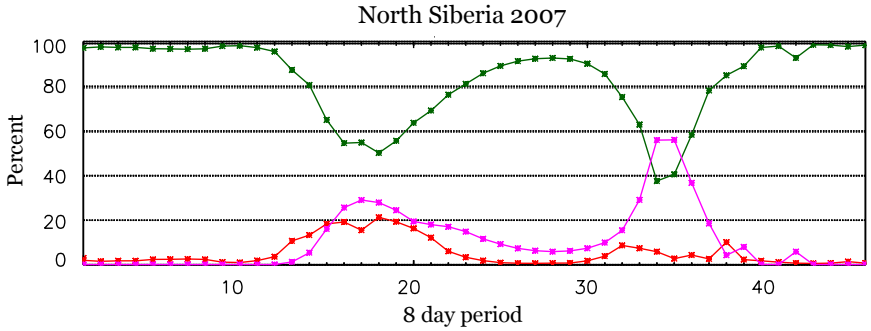

Figure 5.30 – Percent of correct (green), incorrect (red) and around zero (magenta) data points for every 8 day period.

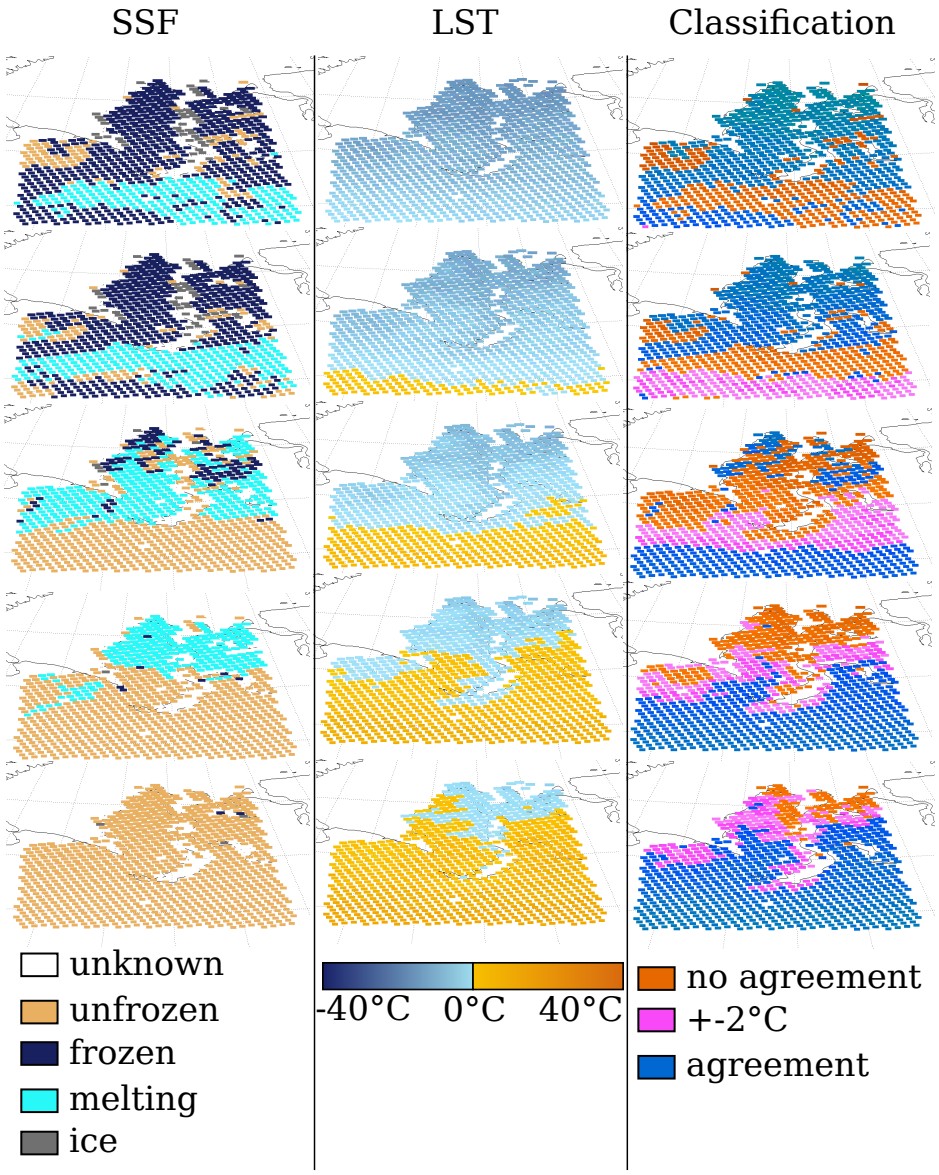

Figure 5.28 – Ob estuary spring thawing period - 8 day periods 15, 17, 19, 21 and 23 (top to bottom).

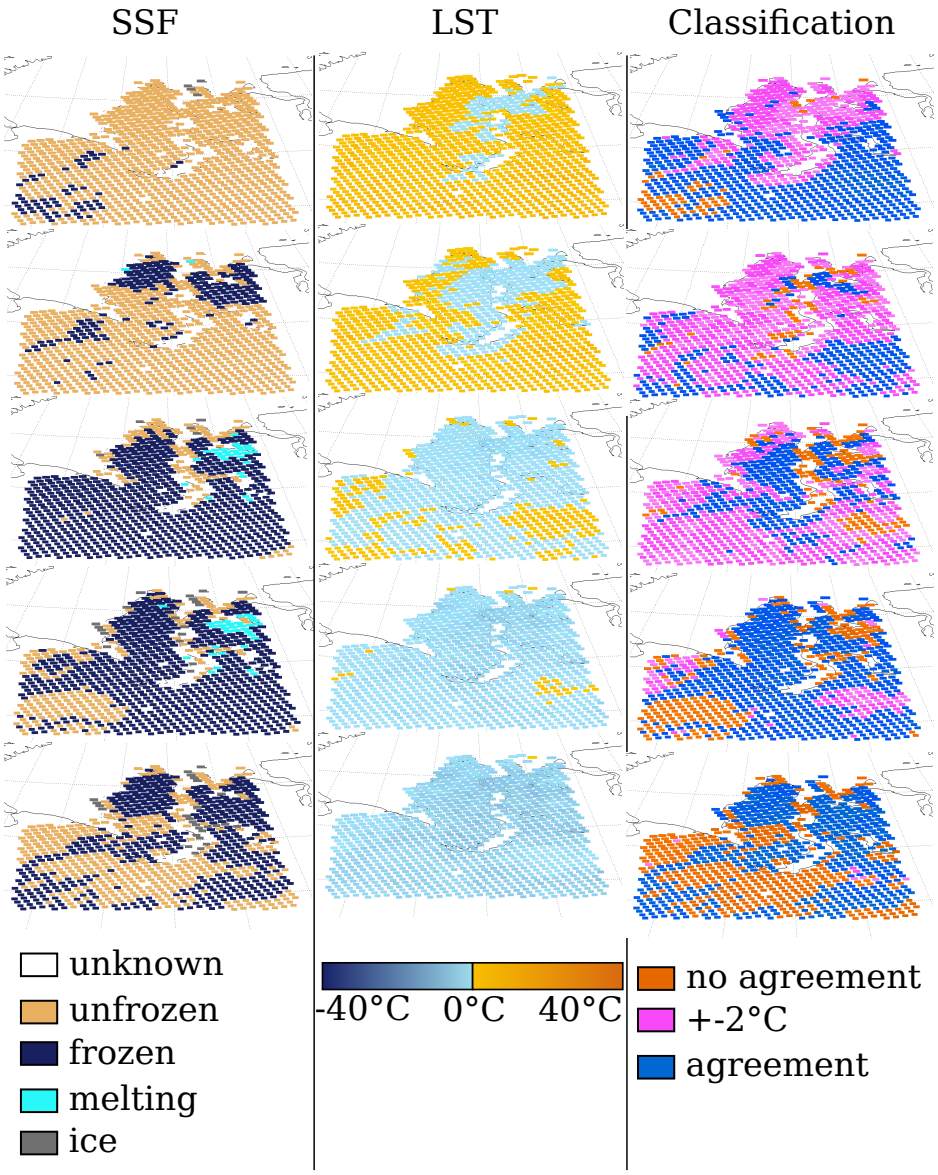

Figure 5.29 – Ob estuary autumn freezing period - 8 day periods 34 to 38 (top to bottom).

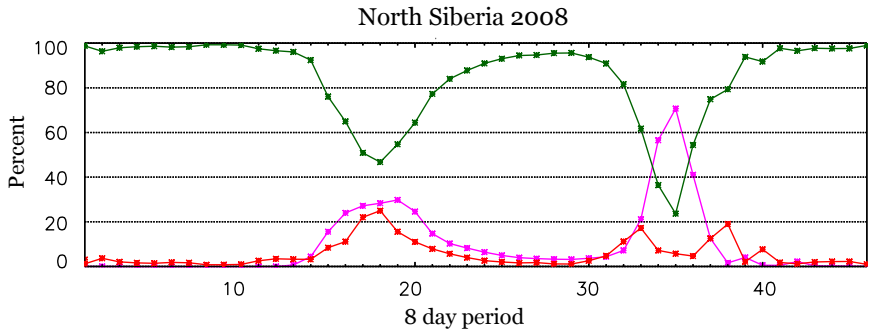

Figure 5.31 – Percent of correct (green), incorrect (red) and around zero (magenta) data points for every 8 day period.

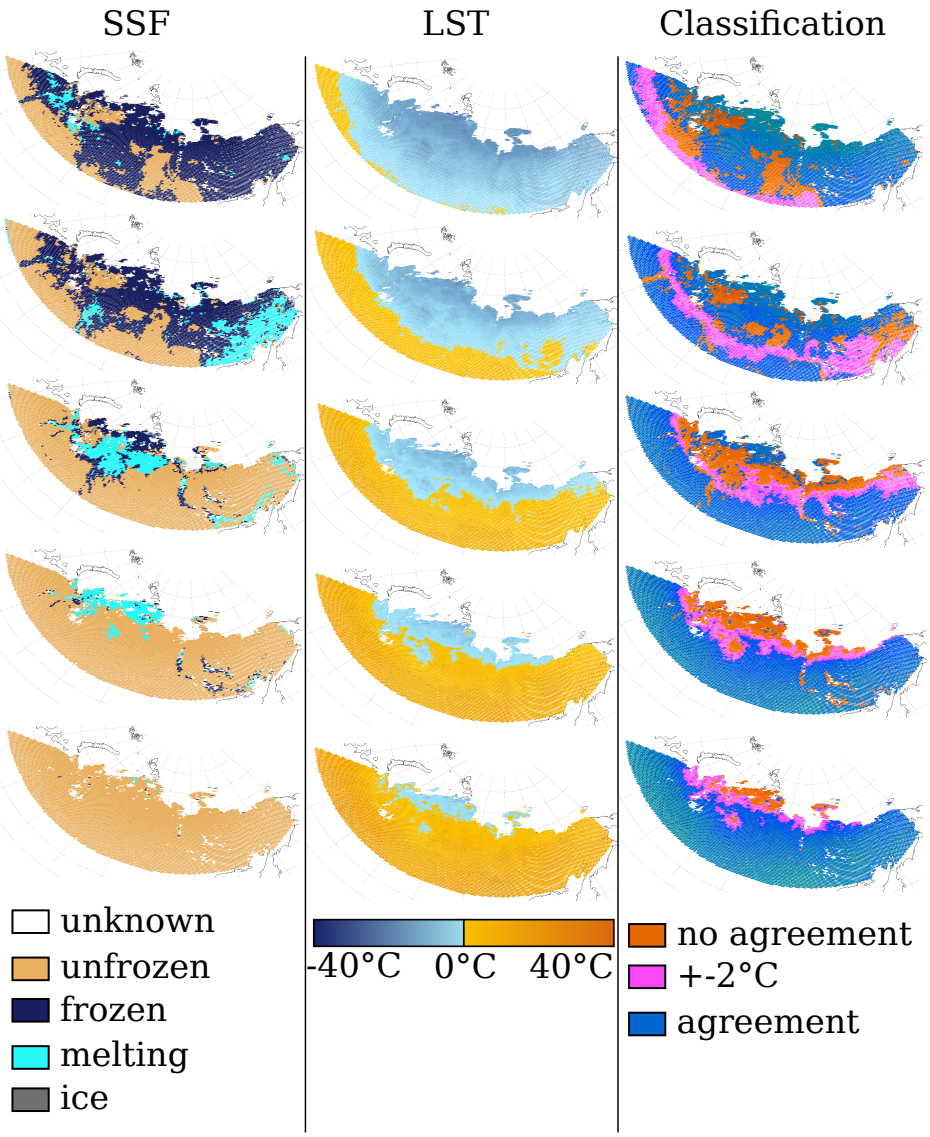

Figure 5.32 – North Siberia spring thawing period 2007 - 8 day periods 15, 17, 19, 21 and 23 (top to bottom).

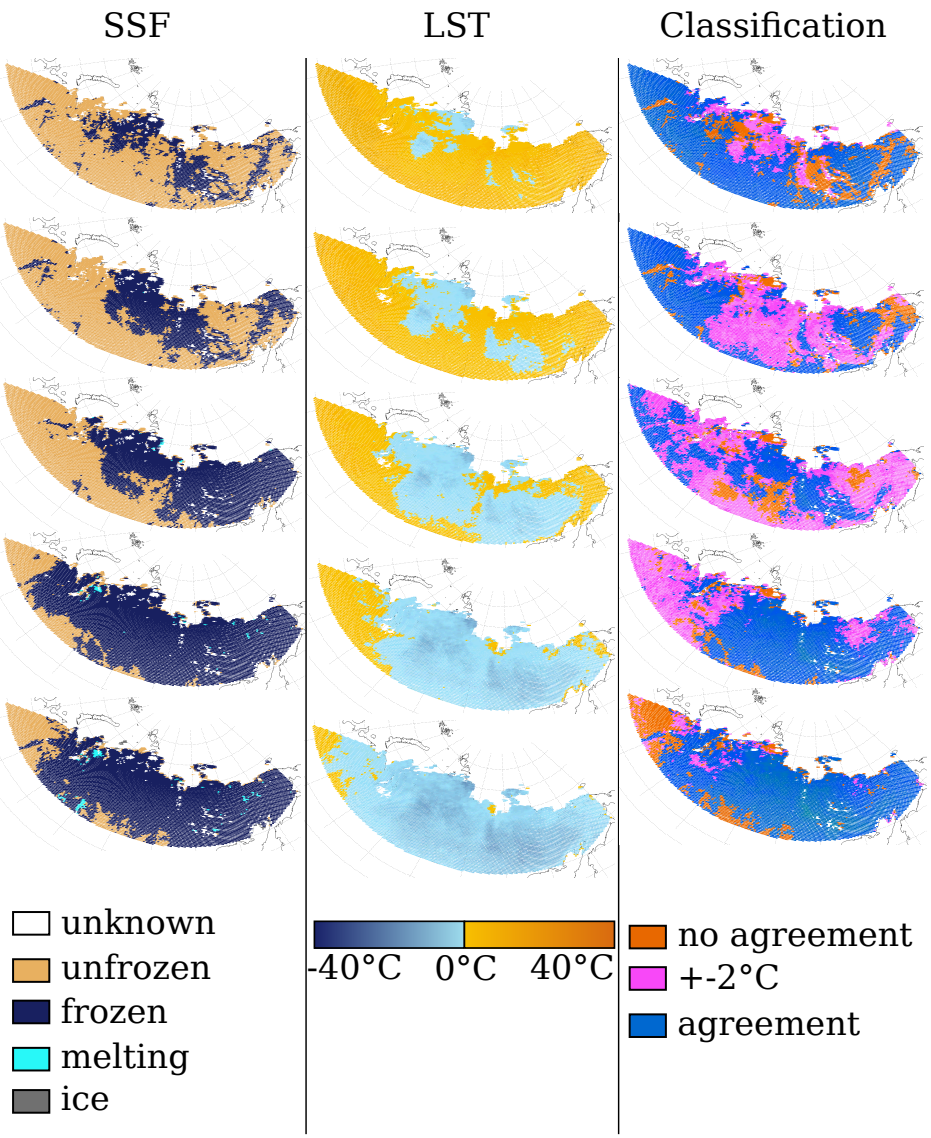

Figure 5.33 – North Siberia autumn freezing period 2007 - 8 day periods 33 to 37 (top to bottom).

5.4.2 AATSR

Kuparuk River

The AATSR data shows the same behavior as the MODIS data. In spring the SSF indicates unfrozen soil too soon (see Fig.5.35). The percentage of incorrect values in week 34 is so high because the SSF flag is missing for a large part of the test area and the averaging algorithm assumes that the ground is still unfrozen as it was in summer.

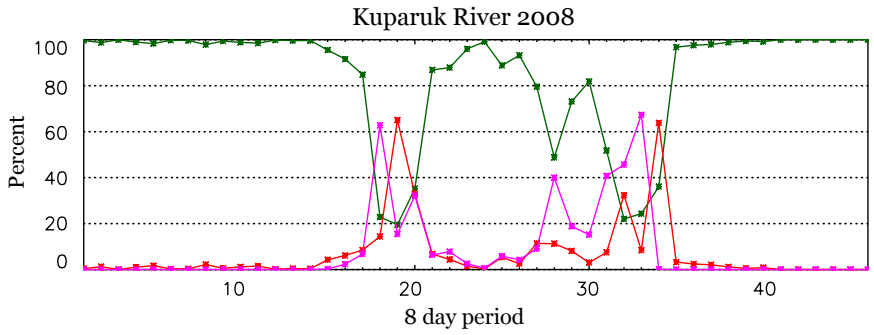

Figure 5.34 – Percent of correct (green), incorrect (red) and around zero (magenta) data points for every 8 day period.

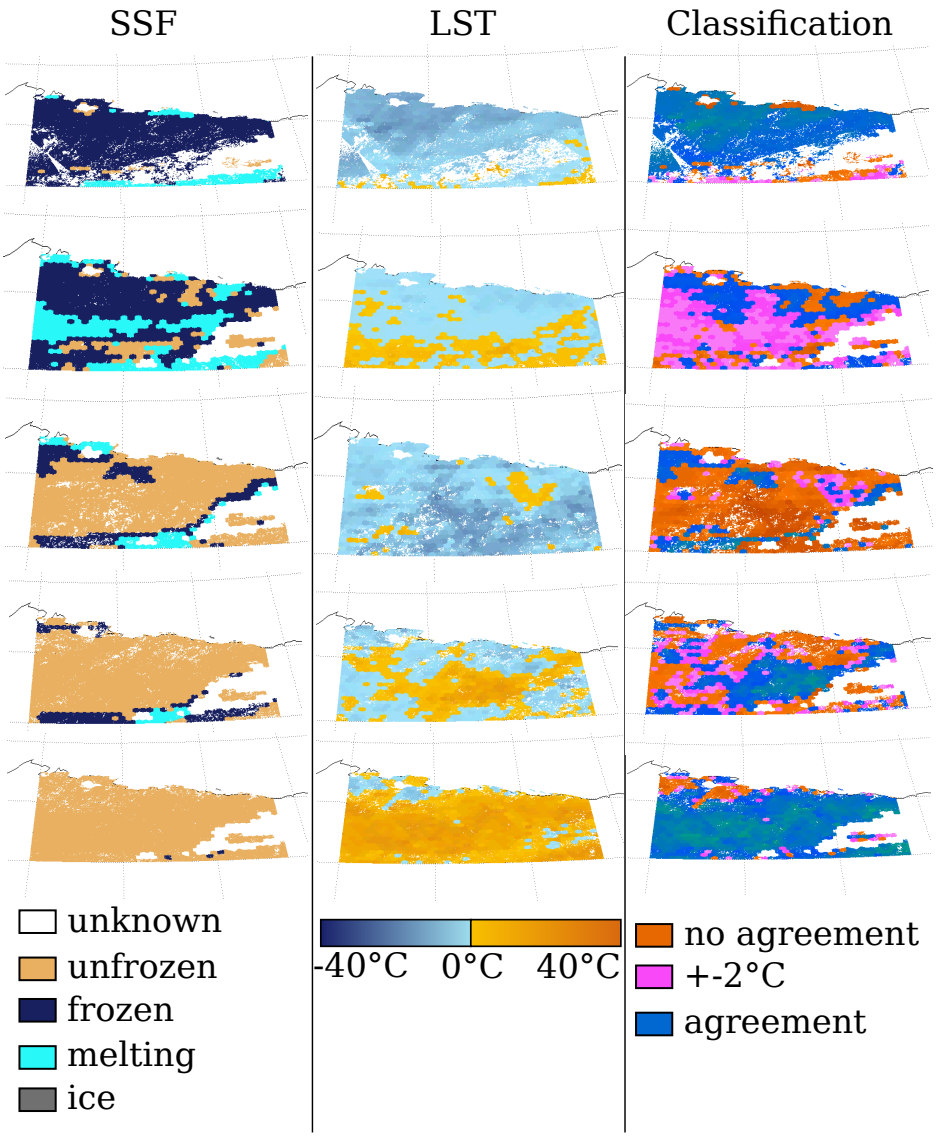

Figure 5.35 – Kuparuk River spring thawing period - 8 day periods 17 to 21 (top to bottom).

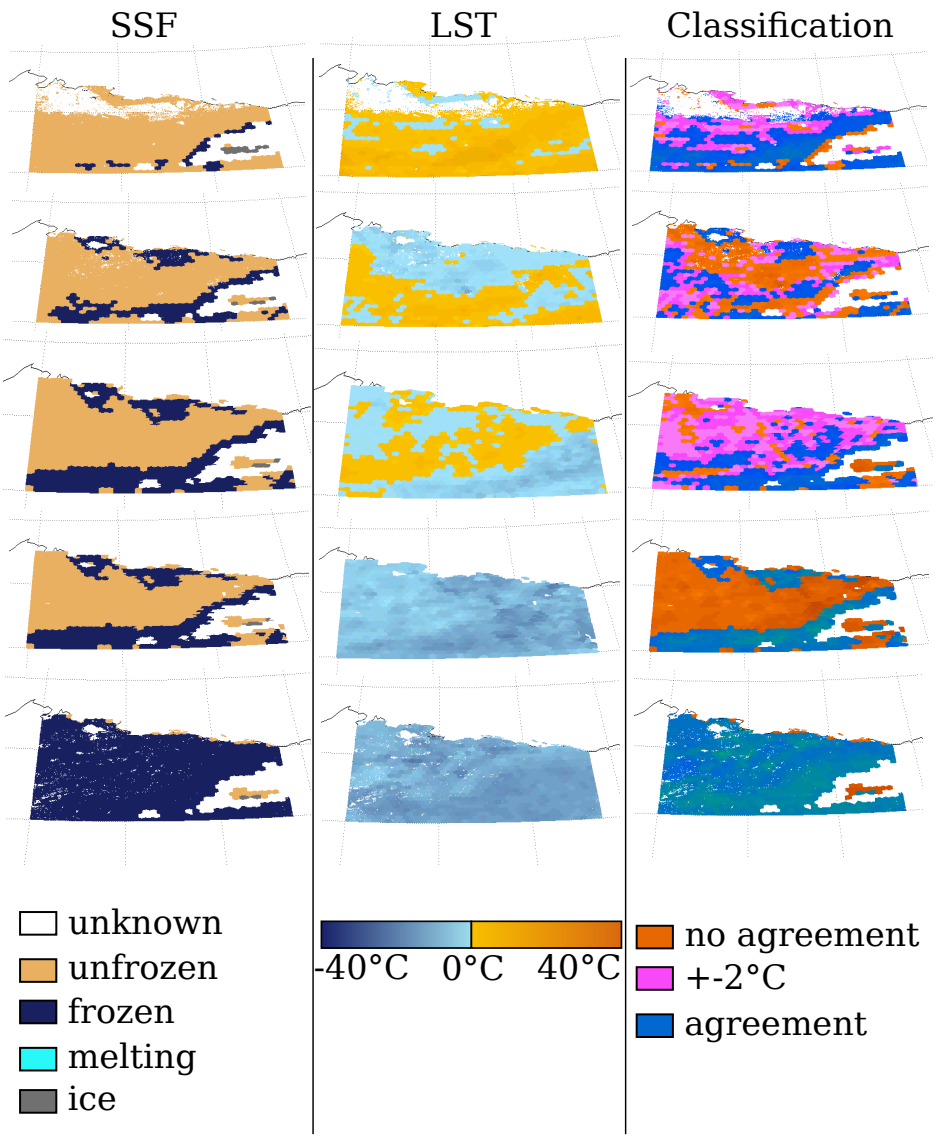

Figure 5.36 – Kuparuk River autumn freezing period 2007 - 8 day periods 31 to 35 (top to bottom).

5.4.3 Conclusion

The common disagreements between the SSF and LST from MODIS and AATSR are that unfrozen surface conditions are flagged to soon in spring and too long in autumn. It also happens in some parts of Siberia and in the Ob Estuary that the SSF jumps from frozen to unfrozen and back about 8 day period 38 (see the red spikes in Fig.5.29 and to a lesser extent in Fig.5.31) without any apparent change in LST. The second problem is how to interpret the SSF when it shows "temporary melting conditions" because that mainly happens in areas where the 8 day composite LST is still negative. Another problem is that the LST temperature is not accurate if clouds obscured the view to the ground.

5.5 Frozen area

Fig.5.37 shows the frozen area per month from [11] and from the derived from the SSF for the northern hemisphere. The area from the SSF is calculated by counting the gridpoints that are frozen, according to the SSF, at least once in each month and multiplying this number by $156.25 km^2$, which is the pixel size of a DGG grid point. The estimate of the SSF is to small but the SSF can not be derived for 28689 DGG points that would otherwise most likely experience freezing (see the white areas that are missing from Fig.4.3), which means that a maximum area of approx. $4.510^6 km^2$ is missing. Accounting for the missing area and the fact that thawing SSFs were not considered, the agreement with the results from [11] is very good.

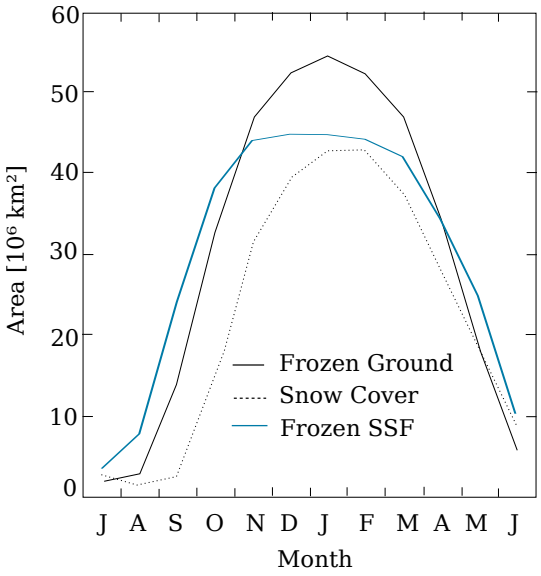

Figure 5.37 – Frozen area per month for the northern hemisphere from SSF and from [11]

5.6 Conclusion

The algorithm compares favorable to to all temperature datasets, if the backscatter changes enough with temperature and this relationship shows little to no ambiguities.Furthermore the winter and summer months should both be about 3 months long. In regions where these factors are not satisfied the algorithm is not reliable.

Improvements to the algorithm could definitely be made by eliminating the ambiguities using ancillary data, which will be tried in the following chapter. Further improvements could maybe be made to the freeze/thaw parameters, especially pt1 and pt2.

The validation approach has problems with the thawing SSF because it is not clear at which temperature range it should be considered as correct or incorrect, since this depends also on snow cover. This problem can also be seen in the different methods that the model datasets seem to use. GLDAS keeps soil temperature below the freezing point of water if snow is present while ERA-Interim permits positive values.

Choosing a threshold of 0°C to find the agreement of the SSF and the temperature datasets may be a little bit strict. Kim et.al [13] used a 3 degree threshold to distinguish frozen from unfrozen conditions and reported that using a stricter threshold reduced overall classification accuracies 2 to 6%. Kim.et.al were using a completely different algorithm but since the overall classification results are similar to what was achieved with the SSF algorithm this should provide a good estimate for what happens when using a different threshold.

6

Possible Improvements

As discussed in the previous chapter, the current algorithm has several shortcomings which may be solvable using ancillary datasets. Decision Tree 2 is only introduced because of ambiguities in backscatter, in this case low σ_{40} values in summer, but the critical behaviour around 0° C is the same as in Decision Tree 1. Other ambiguities are not considered in the algorithm and result in unknown or wrong surface states. Since most ambiguities do not occur at temperatures around 0° C the basic premise of the algorithm remains unchanged. It was tried to use ancillary datasets in a fashion that allows to simplify the existing decision trees and makes them more robust while resolving most of the ambiguities.

6.1 Improved algorithm

In the resulting algorithm just 2 decision trees whose main difference is the behaviour of σ_{40} during freezing (the direction of the logistic function) are used. Ambiguities are resolved using ancillary data in 2 ways:

- A simple temperature threshold, using the ERA-Interim 2m air temperature.
- Frozen probabilities based on 20 years of ERA-Interim 2m air temperature combined with snow and ice probabilities from SSM/I (see chapter 3)

ERA-Interim Air temperature was used because the Freeze/Thaw parameters are also based on this dataset. It would be preferable to compute both parameter sets using soil temperature. Any other global temperature dataset (e.g. GLDAS-NOAH) could also be used, but the recalculation and revalidation with different datasets was beyond the work considered for this thesis.

6.1.1 Threshold method

A simple temperature threshold, using the ERA-Interim 2m air temperature, was implemented, meaning if the temperature is above the threshold value only unfrozen or thawing surface state is permitted and if the temperature is below the negative threshold value only the frozen surface state is possible.

The advantage of this method is it's simplicity whereas the disadvantage is the need to have ERA-Interim data available for Freeze/Thaw detection which disqualifies this method for use in near real time applications. ERA Forecast data could be used in NRT applications but this would complicate the needed processing chain a lot, since another datastream has to be added in near real time. It would also make the resulting SSF dependent on the availability of the ERA Forecast.

Choosing a suitable threshold value

A suitable threshold was chosen through trial and error. Starting at 0.5°C the threshold was raised in 1 degree steps until it reached 7.5 degrees.Every step was compared to WMO Meteo data according to the method outlined in chapter 5. Additionally a 0 and 50 °C threshold were used to simulate the results of using only temperature and to see how the simplified decision trees perform without the additional information provided by a temperature dataset.

Fig.6.1 shows ROC plots (see chapter 5.1.1) of the 4 time periods and one for the whole 2 year validation. The new algorithm performs better in comparison to WMO meteo temperature data than the original for every temperature threshold. If no threshold is used (50 degrees C was used as an equivalent to no threshold) the new decision trees perform not as good, but this is to be expected since the complex rules that catch certain ambiguities in backscatter have been removed.

In Winter the false positive rate becomes smaller and smaller as the temperature threshold drops toward 0°C. In the original algorithm about 40 percent of all SSFs observed, when WMO temperatures were above the thawing point of ice, were not in agreement with the temperature data. The new algorithm without the use of ancillary data maintain this figure but it performs worse when flagging backscatter measurements taken below 0°C. The axes of the ROC plot are scaled very differently. The change in TPR is only about 3.5% while the change in FPR is 25% from the best to the worst algorithm. Interestingly the TPR drops when the temperature threshold drops below about 3°C, showing that WMO meteo and ERA Interim data are not 100% in agreement.

In Summer the FPR is very low since an overwhelming majority of measurements are taken during positive temperatures an nearly all of them are correctly flagged as unfrozen by all algorithms. An outlier in this respect are the new decision trees without ancillary data, since there is no longer an invalid SSF the new decision trees wrongfully assume frozen ground when the soil is very dry in summer. The TPR is very low for the original algorithm since nearly all measurements taken, when temperatures were below 0°C, are flagged as unfrozen. The ancillary data helps to find these anomalies, another possibility is that, in some rare cases, summertime is not defined correctly because of reasons discussed in chapter 5.2.6.

The transition zones of the year behave similarly, with linear improvement with lower temperature threshold. The original algorithm in autumn does stand out through its very high TPR, but since the the difference is only a few percent it is not as important as the improvements of over 10% in FPR.

ROC plots do not consider invalid SSFs, but they provide a space saving overview of the different classification results.

Table 6.1 shows the agreement, of the original and the new algorithm using different temperature thresholds, with WMO meteo data in percent. In the original algorithm there was a difference in agreement between winter and the two transition times, the new algorithm performs equally well during the whole year and very good in summer.

Keeping in mind that temperature data does not equal freeze/thaw data, it would be best to chose a threshold that provides enough information to make wrong classification especially in winter and summer unlikely while leaving enough freedom to the scatterometer data to provide real freeze/thaw detection. 5°C seems to be a good compromise between assistance in flagging and not overtraining the algorithm to the temperature dataset.

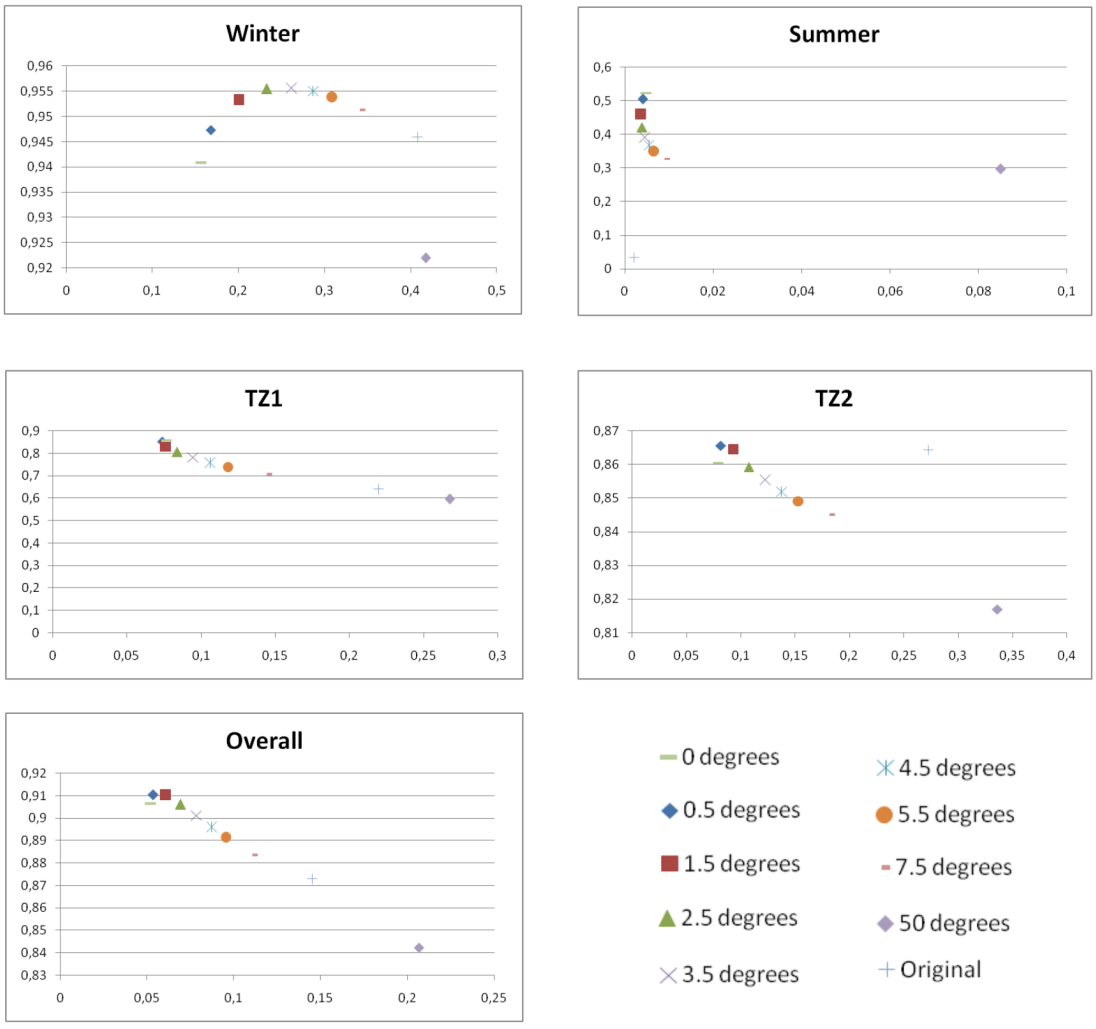

Figure 6.1 – ROC plots of different times of the year for several temperature thresholds (All plots have the false positive rate on the x-axis and the true positive rate on the y-axis

6.1.2 Frozen Probabilities

The frozen probabilities derived from ERA Interim data and the snow and ice cover probability flags, provided with the ASCAT data, are used (see chapter 3.6)

	Winter	Spring(TZ1)	Summer	Autumn(TZ2)	Overall
0 °C	89,89	90,62	98,96	90,61	93,72
0,5 °C	89,77	90,70	99,00	90,57	93,72
1,5 °C	88,76	90,06	99,00	89,66	93,18
2,5 °C	87,55	88,81	98,93	88,43	92,41
3,5 °C	86,35	87,38	98,82	87,23	91,61
4,5 °C	85,26	85,93	98,70	86,00	90,83
5,5 °C	84,29	84,51	98,58	84,78	90,08
7,5 °C	82,77	81,72	98,29	82,47	88,73
50 °C	78,16	69,70	90,74	70,08	80,52
original	77,87	71,67	92,32	73,41	81,93

Table 6.1 – Accuracy of the SSF algorithm using different temperature thresholds, in percent

If there are very high (> 95 percent) probabilities for frozen soil for a given day then no unfrozen surface state flag is permitted and if there are very low (< 5 percent) probabilities no frozen surface state is allowed. The snow and ice probability data is used with the same 95 and 5% thresholds. The problem with that is that the probability of snow cover sometimes jumps to 0% during winter which is probably an error in the data, because of that the 5% threshold for snow and ice probabilities is only allowed to change the SSF to unfrozen if the probability for frozen soil is below 50 percent.

The advantage of this method is that only the probability dataset is needed to better resolve the ambiguities in the σ_{40} data which makes this method viable for near real time applications. Extreme warm or cold periods are ignored by the probability dataset and could lead to wrongful flagging of measurements.

6.1.3 Simplified Decision Trees

Decision Tree 1 is shown in Figure 6.2 in it's simplified version. The threshold to differentiate between frozen and unfrozen conditions was unified and is now the freeze level + $2^{*}\sigma$ noise all year round. The lookup table for uncertain situations was removed because these cases should be handled by the ancillary data.

Decision Tree 2 is not necessary when using ancillary data and Decision Tree 3 is unchanged.

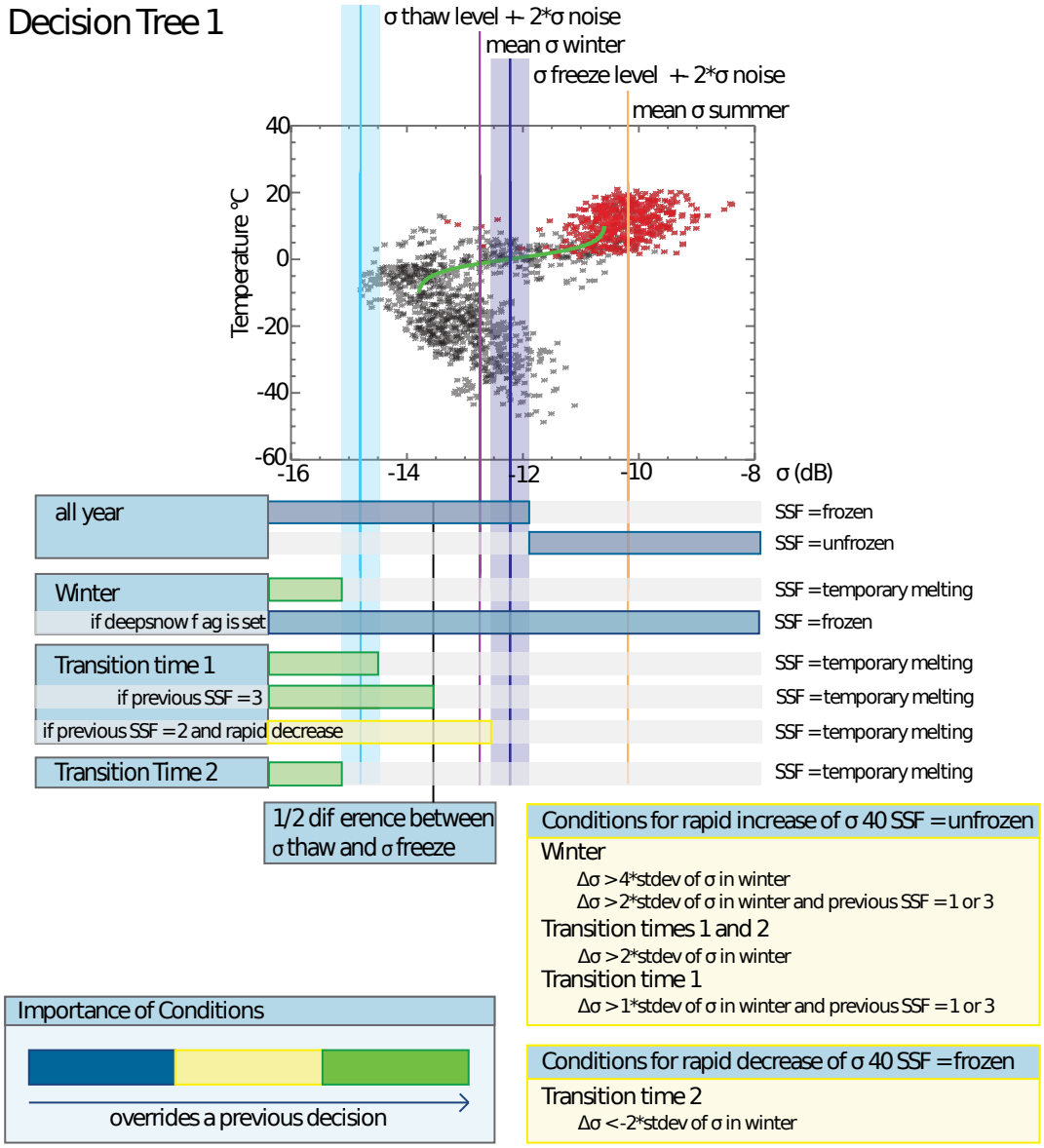

Figure 6.2 – Decision Tree 1 simplified

6.2 Comparison with original algorithm

In this section we are going to examine how the agreement with the datasets, used for validation of the original SSF, has changed. ERA Interim will not be used in this second validation since the ancillary data is based largely on this dataset.

The agreement with the temperature data from the GTN-P stations did not change significantly (less than 1% in most cases), so the results are not repeated in this section.

6.2.1 WMO Meteo data

Nearly all of the WMO meteo stations are in better agreement with the new algorithms. The algorithm using the temperature threshold performs better than the one using the frozen probabilities(see Fig.6.3 and 6.4). Some stations perform slightly worse when using the simplified decision trees and the ancillary data. This is easily observed for the algorithm that uses the probability flags, but these points only show a slight reduction in agreement and were all points where the original algorithm works very well. Table 6.2 shows that the improvement for both algorithms is especially good for the 2 transition zones where it ranges from 8.1 to 13.55 % in spring and from 11.98 to 12.1 % in autumn. Overall the improvement in agreement with WMO Meteo data is about 8 percent with most of it coming in regions where the original algorithm had problems. Central northern America, south and west Europa, Scandinavia and east Asia (eastern China, South Korea and Japan) see the biggest improvements.

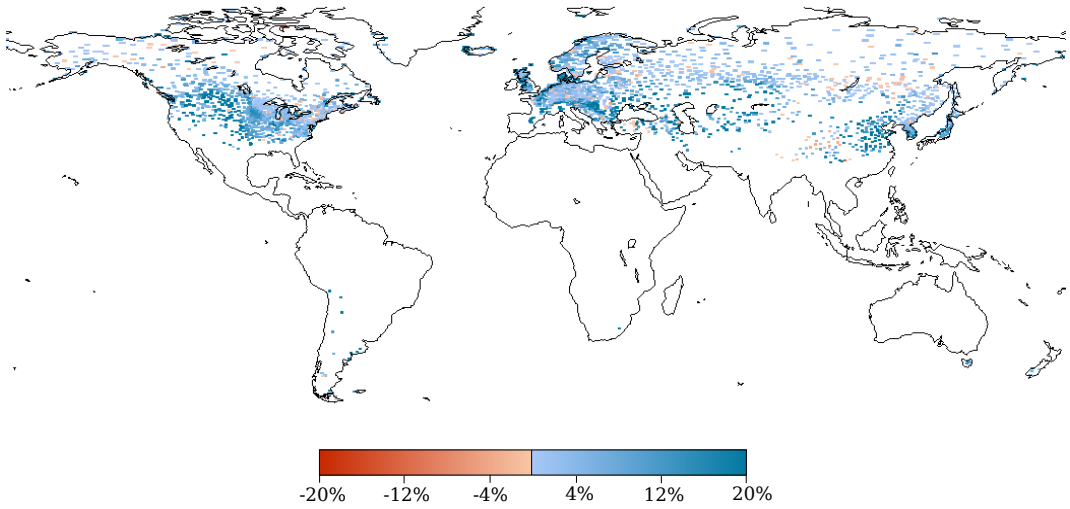

Figure 6.3 – Agreement with WMO Meteo temperature data of algorithm using 5°C temperature threshold minus agreement of original algorithm in percent.

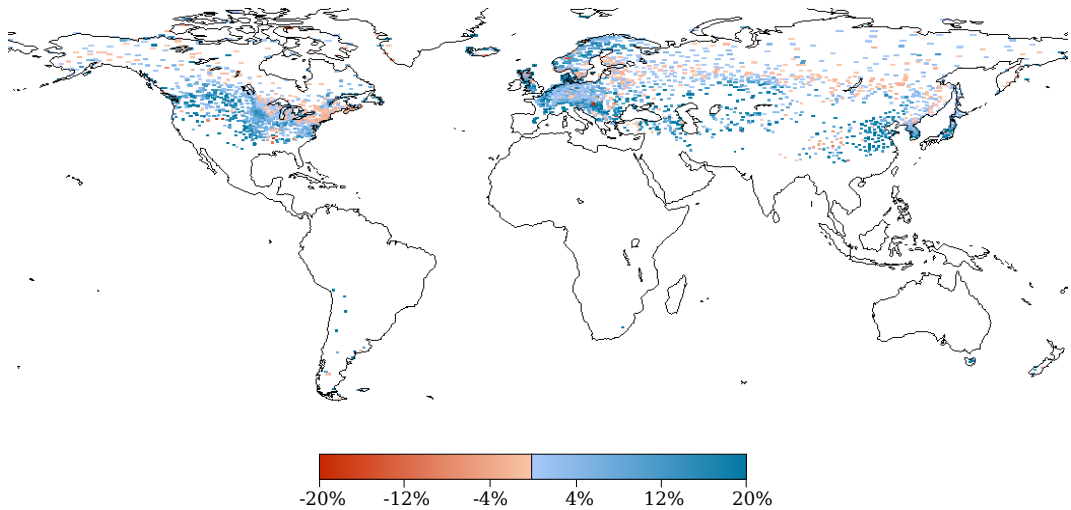

Figure 6.4 – Agreement with WMO Meteo temperature data of algorithm using frozen probabilities minus agreement of original algorithm in percent.

Method	Winter	Spring(TZ1)	Summer	Autumn(TZ2)	Overall
5 °C threshold	84,78	85,22	98,64	85,39	90,46
Probability Flags	82,88	79,77	98,06	85,51	89,21
original	77,87	71,67	92,32	73,41	81,93

Table 6.2 – Agreement of the SSF algorithms with WMO Meteo data using different ancillary data, in percent

6.2.2 GLDAS soil temperature

The comparison with GLDAS soil temperature shows similar patterns than that with the WMO temperature dataset. Most improvements over the original algorithm are in areas where freezing is seldom or the relationship between backscatter and temperature is not very well established.

In northern regions where the original algorithm worked very well we can see in Fig. 6.5 and 6.6 that the agreement with GLDAS soil temperature data is slightly worse than it was when using the original algorithm. The original decision trees where optimized for these regions and it seems that in these cases the ancillary data does not provide enough additional information to offset the simplification that was done to the decision trees. But the accuracy in these regions remains very high.

The agreement increases between 4 and 11 percent (see Table 6.3). The 2 methods provide similar improvements in all cases but spring where the method using the historical climatological flags performs 4% worse.

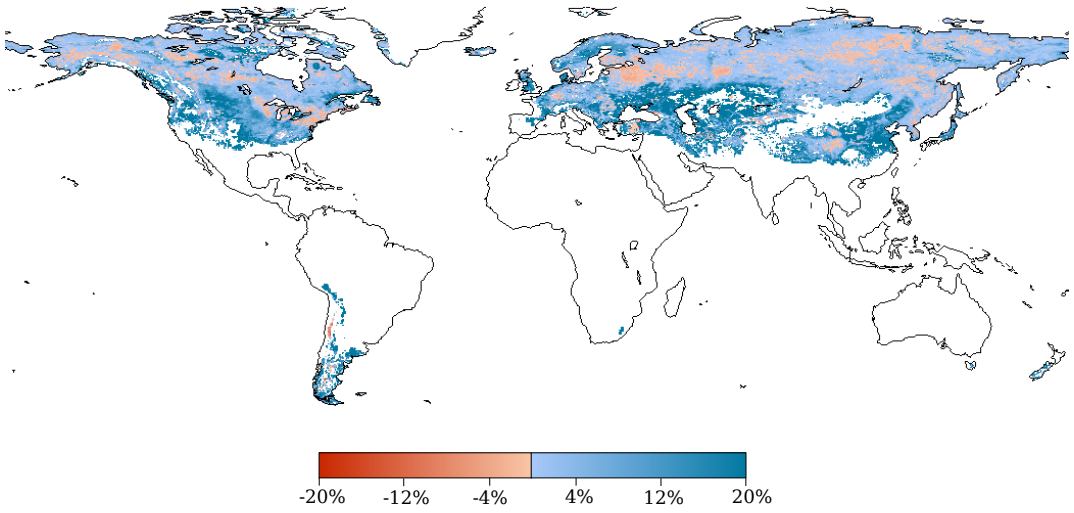

Figure 6.5 – Agreement with GLDAS soil temperature data of algorithm using frozen probabilities minus agreement of original algorithm in percent.

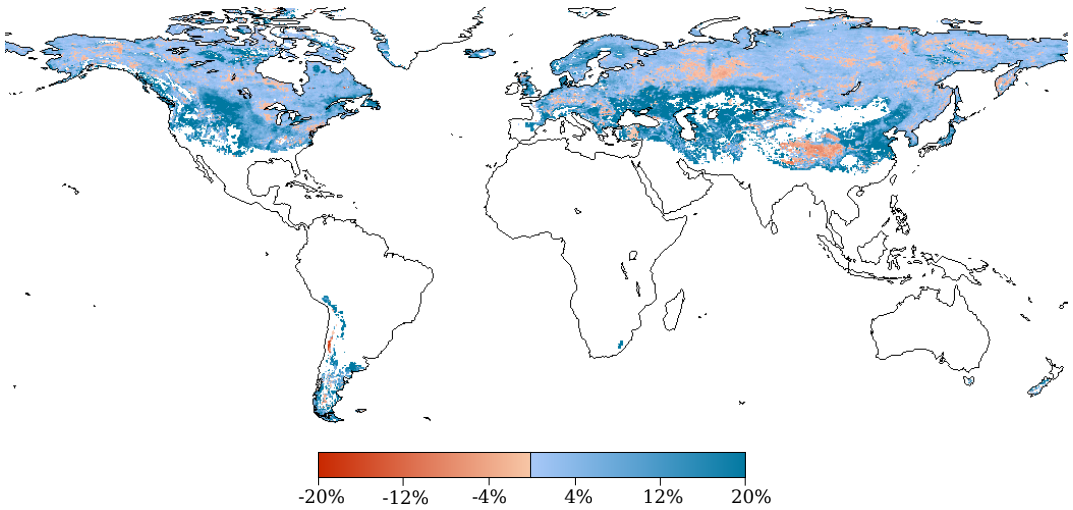

Figure 6.6 – Agreement with GLDAS soil temperature data of algorithm using 5°C temperature threshold minus agreement of original algorithm in percent.

Method	Winter	Spring(TZ1)	Summer	Autumn(TZ2)	Overall
5 °C threshold	93,26	79,65	97,08	86,32	91,11
Probability Flags	93,77	75,66	97,35	86,21	90,75
original	89,52	68,72	91,56	74,16	84,27

Table 6.3 – Agreement of the SSF algorithms with GLDAS soil temperature using different ancillary data, in percent

6.3 Unknown SSF and Failure cases

The unknown SSF does not exist in the new algorithm, so all problems shown in chapter 5.2.5 can be considered solved when using one of the two ancillary datasets.

The situations that were considered failure cases before are now showing good agreement with the temperature datasets. The information contained in the ancillary datasets compensates for errors in the definition of the transition times as well as for the ambiguities introduced by high backscatter in winter.

Figure 6.7 shows the three possible SSF time series for a grid point in northern Siberia. In the top right plot the upper time series was computed using the historical quality flags, the middle one that is centered around 0 degrees celcius is the original and the one at the bottom was computed using the 5 degree threshold method. It can be seen that both ancillary datasets eliminate the errors made by the original algorithm. No longer are there unfrozen flags in the middle of winter and the frozen flag does not start until summer is really over. The algorithm using the climatological probabilities performs more consistent especially at the end of summer when the temperature threshold is not in effect.

The frozen, snow and ice probabilities shown in the bottom right graph in Fig. 6.7 fit very well to the freezing and unfreezing pattern described by the backscatter. In times when the probability flags are uncertain σ^{40} can provide the necessary information about the freeze/thaw timing. In summer and winter when it is always unfrozen or frozen the ambiguities in backscatter do not matter because the frozen and snow probabilities show the correct freeze/thaw state of the surface.

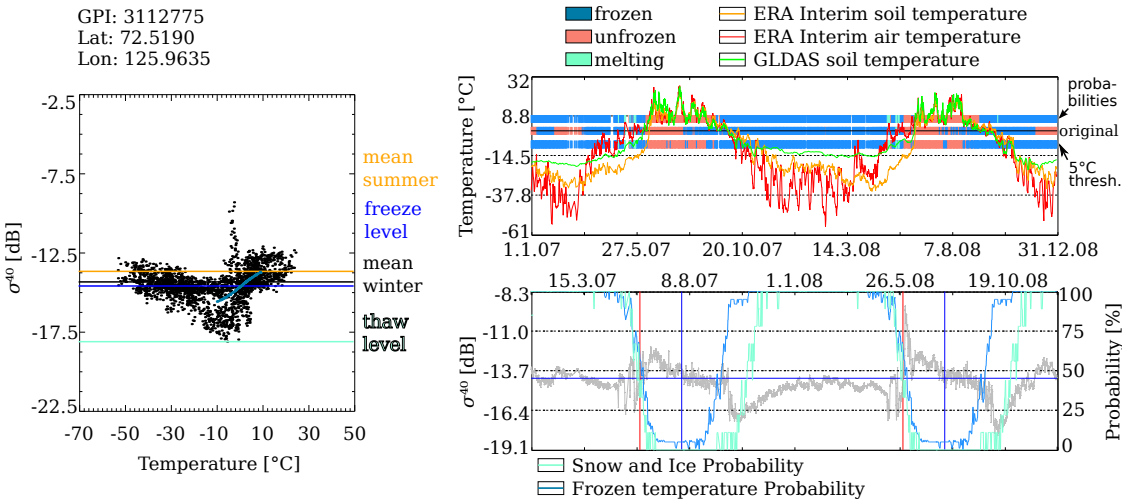

Figure 6.7 – On the left: σ_{40}/temperature plot, with the fitted logistic function in dark blue. On the right: Temperature plot with three possible SSFs indicated around the o°C line and σ_{40} plot with freeze level(horizontal blue line) and the transition times pt1 and pt2 (vertical red and blue lines respectively) for a grid point in north Siberia

The incorrect fitting of the logistic function can also be compensated by the ancillary datasets but the algorithm still assumes a wrong relationship between backscatter and temperature. These problems in the definition of the freeze/thaw parameters should be addressed in future versions of the algorithm.

7

Summary and Outlook

The original algorithm was shown to work well in northern areas but it was discovered that ambiguities in the relationship between backscatter and temperature cause the algorithm to fail in different ways. Is was suggested to use ancillary datasets in the form of either temperature data or historical climatological information to make the algorithm more robust. Additionally, because obvious summer and winter conditions can be taken care of by the ancillary datasets, it was possible to simplify the original decision trees and eliminate one altogether.

The suggested changes to the algorithm improved the validation results in most cases, especially in regions where the relationship between backscatter and temperature was not very strong or freezing is seldom. The usage of both ancillary datasets leads to a more consistent accuracy, both in time and in space. The ERA Interim temperature threshold leads to slightly better results but also needs a large amount of additional data that has to be updated whenever the time series of the ASCAT measurements is extended. The climatological probabilities can stay constant for several years without any changes and are also useful for near real time application of the algorithm.

Which method is used depends strongly on the available resources during processing as well as the trust that is placed in either dataset. The original algorithm may provide the "cleanest" product since it is more or less only dependent on the backcattered signal but it alone is not able to provide truly global flagging of the freeze/thaw state with consistent accuracy. So it is very interesting for academic purposes or regional applications, but any use case that requires global coverage will need ancillary data or other datasets to complement the original algorithm and this thesis presented two possibilities to do that.

7.1 Future Work

The robustness of the algorithm should improve if longer backscatter time series are used for calculation of the freeze/thaw parameters. The algorithm for calculating the transition days could be improved so that the detection also works when the seasons are very much longer or shorter than the 3 months assumed in the current version. Also the fitting of the logistic function should be improved. If a quality estimate of the fit of the function would be available it would be possible to reduce or increase the influence of the ancillary datasets accordingly and maybe find optimal thresholds for every grid point.

The thawing SSF is tricky since thawing snow or water on the surface say little about the actual freeze/thaw state of the soil. During validation it is difficult to decide if a thawing SSF is in agreement with negative or positive temperature data. More work needs to be done to decide how useful the flag is for different applications.

B

Bibliography

[1] Wikipedia, "Wikipedia article about absorption (electromagnetic radiation)." http://en.wikipedia.org/wiki/File:Atmospheric_electromagnetic_opacity.svg, August 2011.

[2] F. Ulaby, R. Moore, and A. Fung, *Microwave Remote Sensing - Active and Passive*. Remote Sensing Library, Artech House, Incorporated, 1986.

[3] R. Feynman, R. Leighton, and M. Sands, *The Feynman Lectures on Physics: Commemorative Issue*. Basic Books, 2005.

[4] E. Schanda, *Physical fundamentals of remote sensing*. Springer-Verlag, 1986.

[5] M. Hallikainen, F. Ulaby, M. Dobson, and M. El-Rayes, "Dielectric measurements of soils in the 3- to 37-Ghz band between -50°c and 23°c," *IEEE International Geoscience and Remote Sensing Symposium (IGARSS)*, pp. 163 – 168, August 1984.

[6] Z. Bartalis, *Spaceborne Scatterometers for Change Detection over Land*. PhD thesis, Technical University of Vienna, 2009.

[7] I. Woodhouse, *Introduction to microwave remote sensing*. Taylor and Francis, 2006.

[8] T. Fawcett, "An introduction to ROC analysis," *Pattern Recognition Letters*, vol. 27, no. 8, pp. 861 – 874, 2006. ROC Analysis in Pattern Recognition.

[9] Wikipedia, "Wikipedia article about semi-arid climate." http://en.wikipedia.org/wiki/Semi-arid_climate, August 2011.

[10] Wikipedia, "Wikipedia article about canadian prairies." http://en.wikipedia.org/wiki/Prairie_Provinces, August 2011.

[11] T. Zhang, R. Barry, and K. Knowles, "Distribution of seasonally and perennially frozen ground in the northern hemisphere," *Permafrost Proceedings of the Eight International Conference on Permafrost*, pp. 1289–1294, 2003.

[12] G. Rees, *Physical principles of remote sensing*. Topics in remote sensing, Cambridge University Press, 2001.

[13] Y. Kim, J. Kimball, K. McDonald, and J. Glassy, "Developing a global data record of daily landscape freeze/thaw status using satellite passive microwave remote sensing," *IEEE Transactions on Geoscience and Remote Sensing*, vol. 49, pp. 949–960, 2011.

[14] S. Solomon, I. P. on Climate Change, and I. P. on Climate Change. Working Group I., *Climate change 2007: the physical science basis : contribution of Working Group I to the Fourth Assessment Report of the Intergovernmental Panel on Climate Change*. Climate change 2007, Cambridge University Press, 2007.

[15] V. Naeimi, C. Paulik, W. Wagner, A. Bartsch, R. Kidd, and J. Boike, "ASCAT Surface State Flag (SSF): Extracting information on surface freeze/thaw conditions from backscatter data using an empirical threshold-analysis algorithm," *submitted*.

[16] W. Wagner, *Soil Moisture Retrieval from ERS scatterometer data*. PhD thesis, Technical University of Vienna, 1998.

[17] A. von Hippel, "The dielectric relaxation spectra of water, ice and aqueous solutions, and their interpretation. Ii. tentative interpretation of the relaxation spectrum of water in the time and frequency domain," *Electrical Insulation, IEEE Transactions on*, vol. 23, pp. 817 –823, oct 1988.

[18] M. Hallikainen, F. Ulaby, and M. Abdelrazik, "Dielectric properties of snow in the 3 to 37 Ghz range," *Antennas and Propagation, IEEE Transactions on*, vol. 34, pp. 1329 – 1340, nov 1986.

[19] J. Wang, T. Schmugge, and D. Williams, "Dielectric constants of soils at microwave frequencies - Ii," tech. rep., NASA - Goddard Space Flight Center, may 1978. NASA Technical Paper 1238.

[20] P. Koorevaar, G. Menelik, and C. Dirksen, *Elements of soil physics*. Developments in soil science, Elsevier, 1983.

[21] M. Tiuri, A. Sihvola, E. Nyfors, and M. Hallikaiken, "The complex dielectric constant of snow at microwave frequencies," *Oceanic Engineering, IEEE Journal of*, vol. 9, pp. 377 – 382, dec 1984.

[22] S. C. Colbeck, "The geometry and permittivity of snow at high frequencies," *Journal of Applied Physics*, vol. 53, pp. 4495 –4500, jun 1982.

[23] A. Denoth, "The pendular-funicular liquid transition in snow," *Journal of Glaciology*, vol. 25, pp. 93–97, 1980.

[24] A. Fung, *Microwave scattering and emission models and their applications*. The Artech House remote sensing library, Artech House, 1994.

[25] V. Naeimi, *Model improvements and error characterization for global ERS and METOP scatterometer soil moisture data*. PhD thesis, Technical University of Vienna, 2009.

[26] WMO, "DS512.0 data hosting facility." `http://dss.ucar.edu/datasets/ds512.0/`, August 2011.

[27] M. Burgess, S. Smith, J. Brown, V. Romanovsky, and K. Hinkel, "The global terrestrial network for permafrost (GTNet-p): Permafrost monitoring contributing to global climate observations.," *Current Research 2000E, Geological Survey of Canada*, 2000.

[28] ECMWF, "ECMWF spatial representations." `http://www.ecmwf.int/products/data/technical/gaussian/spatial_representations.html`, August 2011.

[29] M. Rodell, P. R. Houser, U. Jambor, J. Gottschalck, K. Mitchell, C. Meng, K. Arsenault, B. Cosgrove, J. Radakovich, M. Bosilovich, J. K. Entin, J. P. Walker, D. Lohmann, and D. Toll, "The global land data assimilation system.," *Bulletin of the American Meteorological Society*, vol. 85, pp. 381–394, 03/2004 2004.

[30] A. Bartsch, A. Wiesmann, S. Duguay, M. Urban, D. Sabel, T. Strozzi, S. Hachem, S. Poecking, and V. Naeimi, "ESA DUE permafrost, technical specifications," tech. rep., Institute of Photogrammetry and Remote Sensing.

[31] NASA, "MODIS website." `http://modis.gsfc.nasa.gov/about/`, August 2011.

[32] W. Zhengming, "MODIS land-surface temperature algorithm theoretical basis document (LST ATBD)," tech. rep., Institute for Computational Earth System Science University of California.

[33] ESA, "AATSR website." http://envisat.esa.int/instruments/aatsr/, August 2011.

[34] F. Prata, "Land surface temperature measurement from space: AATSR algorithm theoretical basis document," tech. rep., CSIRO Atmospheric Research Aspendale, Australia.

[35] K. Scipal, V. Naeimi, and S. Hasenauer, "Definition of quality flags. ASCAT soil moisture report series," tech. rep., Institute of Photogrammetry and Remote Sensing.

[36] V. Naeimi, C. Paulik, W. Wagner, and A. Bartsch, "Freeze/thaw detection in permafrost regions with C-band scatterometer," in *ESA Special Publications, SP-688*.

[37] H. Poor, *An introduction to signal detection and estimation*. Springer texts in electrical engineering, Springer-Verlag, 1994.

[38] G. Heinrichs, "Palliser and hind expeditions at the encyclopedia of saskatchewan." http://esask.uregina.ca/entry/palliser_and_hind_expeditions.html, August 2011.

[39] Wikipedia, "Wikipedia article about chinese snow storms of 2008." http://en.wikipedia.org/wiki/2008_Chinese_winter_storms, August 2011.

[40] A. Bartsch, T. Kumpula, B. C. Forbes, and F. Stammler, "Detection of snow surface thawing and refreezing in the eurasian arctic with QuikSCAT: implications for reindeer herding," *Ecological Applications*, vol. 20, no. 8, pp. 2346–2358, 2010.